

**Magnetospheric Period Oscillations of Saturn's
Magnetopause and Bow Shock**

Thesis submitted for the degree of
Doctor of Philosophy
at the University of Leicester

by

Kay Elizabeth Clarke

Radio and Space Plasma Physics Group
Department of Physics and Astronomy
University of Leicester

March 2010

Abstract

Magnetospheric Period Oscillations of Saturn's Magnetopause and Bow Shock

Kay Elizabeth Clarke

In this thesis we show that Saturn's magnetopause and bow shock oscillate with a period near that of planetary rotation that we term the 'magnetospheric period'. In our first study, using two Cassini orbits as exemplars, we demonstrate that Saturn's magnetopause oscillates at the magnetospheric period in response to changes in the magnetospheric pressure. The change in internal pressure required to produce such oscillations, which typically correspond to a ~10% change in the boundary radius, is estimated to be ~30-40% of the unperturbed background pressure. In our second study we develop a simple theoretical model of motion through an oscillating planar boundary that is equally applicable to the magnetopause and the bow shock. In our third study we use data from ~40 Cassini orbits to conduct a first systematic investigation of the magnetospheric period magnetopause oscillations. We show that boundary oscillation events are highly organized by the phase of the magnetic oscillations in the 'core' region of the magnetosphere. When radial propagation is accounted for, the phase of maximum outward boundary displacement is found to be directly related to the phase of the density maximum in the Enceladus torus. The boundary oscillation amplitude is estimated to be ~1.2 Saturn radii, but is occasionally as great as ~4-5 Saturn radii. In our fourth study we use data from 35 Cassini orbits that crossed both the magnetopause and the bow shock to provide first evidence for magnetospheric period bow shock oscillations. We find that the oscillations are significantly organized by the phase of the 'core' magnetosphere magnetic oscillations, though the degree of organization is less than for the magnetopause. The bow shock and magnetopause are found to oscillate approximately in phase within a phase uncertainty of about $\pm 25^\circ$ and to have similar oscillation amplitudes.

Declarations

The research undertaken during the course of this doctoral programme has led to the submission and acceptance for publication of the following three scientific papers:

Clarke, K.E., N. André, D.J. Andrews, A.J. Coates, S.W.H. Cowley, M.K. Dougherty, G.R. Lewis, H.J. McAndrews, J.D. Nichols, T.R. Robinson, and D.M. Wright (2006), Cassini observations of planetary-period oscillations of Saturn's magnetopause, *Geophys. Res. Lett.*, 33, L23104, doi:10.1029/2006GL027821.

Clarke, K.E., D.J. Andrews, C.S. Arridge, A.J. Coates, and S.W.H. Cowley (2010), Magnetopause oscillations near the planetary period at Saturn: Occurrence, phase, and amplitude, *J. Geophys. Res.*, in press, doi:10.1029/2009JA014745.

Clarke, K.E., D.J. Andrews, A.J. Coates, S.W.H. Cowley, and A. Masters (2010), Magnetospheric Period Oscillations of Saturn's Bow Shock, *J. Geophys. Res.*, 115, A05202, doi:10.1029/2009JA015164.

Acknowledgements

I would like to thank Stan Cowley for being an extremely conscientious supervisor, the RSPP group for providing me with financial support over the last few months of my studies, and all its members for creating a friendly and supportive working environment.

Table of Contents

| | |
|---|-----------|
| Chapter 1: Introduction | 1 |
| 1.1 The Solar Wind and the Interplanetary Magnetic Field | 2 |
| 1.2 Planetary Magnetic Fields | 6 |
| 1.3 Planetary Magnetospheres and Bow Shocks | 9 |
| | |
| Chapter 2: The Saturnian Magnetosphere | 15 |
| 2.1 Introduction to the Saturnian System | 15 |
| 2.2 Magnetospheric Period Phenomena at Saturn | 19 |
| | |
| Chapter 3: Instrumentation | 25 |
| 3.1 Introduction | 25 |
| 3.2 The Cassini Orbiter | 25 |
| 3.3 The Cassini Fluxgate Magnetometer | 27 |
| 3.4 The Cassini Electron Spectrometer | 29 |
| | |
| Chapter 4: Cassini Observations of Magnetospheric Period Oscillations of Saturn's Magnetopause | 31 |
| 4.1 Introduction | 31 |

| | | |
|---|--|-----------|
| 4.2 | Case Studies: Cassini Revs 16 and 17 | 31 |
| 4.3 | The Amplitude of the Boundary Oscillations | 36 |
| 4.4 | The Physical Origins of the Boundary Oscillations | 40 |
| 4.5 | Summary and Conclusions | 42 |
| Chapter 5: A Simple Theoretical Model of Motion Through an Oscillating Planar Boundary | | 44 |
| 5.1 | Introduction | 44 |
| 5.2 | Mathematical Formulation | 44 |
| 5.3 | Number of Observed Oscillations | 46 |
| 5.4 | Timing of Boundary Crossings | 51 |
| 5.5 | Width of the Oscillation Layer | 55 |
| 5.6 | Summary and Discussion | 56 |
| Chapter 6: Magnetospheric Period Oscillations of Saturn's Magnetopause: Occurrence, Phase, and Amplitude | | 58 |
| 6.1 | Introduction | 58 |
| 6.2 | Data Set Employed | 59 |
| 6.3 | Relation to the Magnetic Oscillation Phase in the 'Core' Magnetosphere | 60 |
| 6.3.1 | Preliminary Study | 63 |
| 6.3.2 | Main Study | 64 |

| | | |
|--|--|------------|
| 6.4 | Examples of Magnetopause Boundary Oscillations | 68 |
| 6.5 | Occurrence of Magnetopause Oscillations in Cassini Boundary Data | 70 |
| 6.6 | Spatial Coverage of Magnetopause Oscillation Observations | 72 |
| 6.7 | Magnetopause Boundary Oscillation Phase | 73 |
| 6.8 | Estimates of the Boundary Oscillation Amplitude | 78 |
| 6.9 | Summary and Discussion | 87 |
| Chapter 7: Magnetospheric Period Oscillations of Saturn's | | 94 |
| Bow Shock | | |
| 7.1 | Introduction | 94 |
| 7.2 | Data Set Employed | 94 |
| 7.3 | Examples of Bow Shock Oscillations | 95 |
| 7.4 | Relation to Magnetic Phase in the 'Core' Region | 100 |
| 7.5 | Occurrence and Amplitude of Bow Shock Oscillations | 105 |
| 7.6 | Summary | 109 |
| Chapter 8: Summary and Future Work | | 111 |
| 8.1 | Background | 111 |
| 8.2 | Summary | 112 |
| 8.3 | Future Work | 115 |

Appendix 118

References 120

Chapter 1

Introduction

In this thesis we show that at Saturn the positions of the magnetopause and bow shock are modulated at a period near that of planetary rotation that we term the ‘magnetospheric period’. These oscillations are related to magnetic field and plasma oscillations observed inside the magnetosphere.

This introductory chapter concerns the solar wind and interplanetary magnetic field and the formation of magnetospheres and bow shocks through their interaction with magnetized planets. Chapter 2 focuses on the saturnian system, including a detailed discussion of magnetospheric period phenomena observed at the planet. In Chapter 3 we discuss the Cassini orbiter, its tour of the saturnian system, and the fluxgate magnetometer and electron spectrometer instruments that were used to obtain the data employed in the studies presented in Chapters 4, 6, and 7. In Chapter 4, in a study based on the first ~20 Cassini orbits, we use data from two orbits to exemplify our discovery that the position of Saturn’s magnetopause exhibits a magnetospheric period modulation in response to changes in the total magnetospheric pressure. In Chapter 5 we develop a simple theoretical model of motion through an oscillating planar boundary, the results of which inform the data-based studies of Chapters 6 and 7. In Chapter 6 we make the first systematic study of magnetospheric period magnetopause oscillations, using data from ~40 Cassini orbits that crossed the magnetopause during 2004-2007, and examine the phase of the boundary oscillations relative to the magnetic oscillations inside the magnetosphere. This analysis is

then extended to the bow shock in Chapter 7. In Chapter 8 we summarize our findings and consider some directions for future work.

1.1 The Solar Wind and the Interplanetary Magnetic Field

The solar wind is the extension of the Sun's outer atmosphere, permeating the solar system and carrying with it a remnant of the Sun's magnetic field in the form of the interplanetary magnetic field (IMF). The solar wind eventually encounters the local interstellar medium at a distance of $\sim 100\text{-}150$ AU (1 AU is an astronomical unit, the average distance between the Sun and the Earth). The boundary between the two plasmas is called the heliopause, and the region within is the heliosphere, the sphere of influence of the Sun.

Figure 1.1 shows the structure of the Sun's interior and atmosphere. The Sun is a massive ball of plasma held together by its own gravitational attraction. Its composition is 70% hydrogen, 28% helium, and 2% heavier elements by mass. Within its dense core, at temperatures of around 15 million K, nuclear fusion reactions generate photons as a product of the transformation of hydrogen nuclei to helium nuclei. Surrounding the core is the radiative zone, a highly opaque layer in which the photons undergo a 'random walk' of so many scatterings that they take around 10 million years to emerge. Above the radiative zone the temperature falls sufficiently rapidly with radius that the plasma is unstable to convection. It is through dynamo action in this turbulent convection zone that the Sun's magnetic field is generated. Results from helioseismology (the study of the propagation of waves within the Sun) have shown that while the radiative zone rotates rigidly, the convection zone rotates differentially, the rotation being faster at the equator and slower

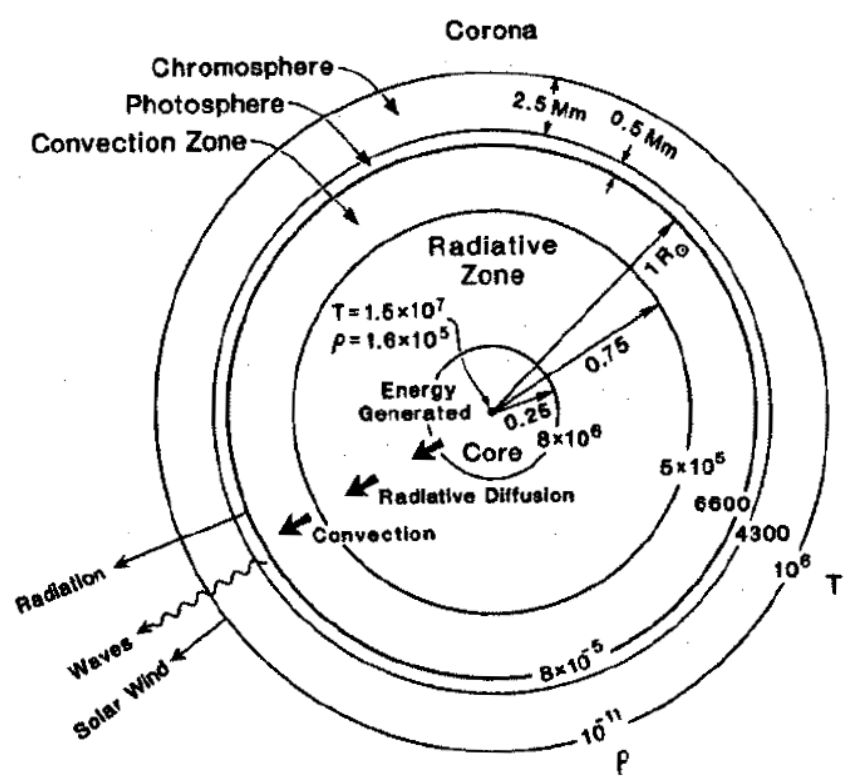


Figure 1.1 The structure of the solar interior and atmosphere. [From Priest, 1995.]

near the poles. The solar dynamo is thought to involve a combination of cyclonic convection (convection modified by the Coriolis force) and differential rotation.

The photosphere, the visible surface of the Sun, is the top of the convection zone. The convection cells can be seen as a pattern of granules. Individual granules are ~ 1000 km across and typically last for about 20 min. Figure 1.2 shows this granulation pattern and some sunspots. Sunspots are regions in which intense magnetic activity inhibits convection, reducing the temperature at the surface so that they appear as dark patches against the hotter background. Their number varies quasi-periodically on timescales of ~ 9 -14 years, the mean interval being ~ 11 years. Figure 1.3 shows the monthly sunspot numbers for the last five solar cycles. The studies presented in this thesis use data obtained between mid-2004 and the end of 2007 which can be seen to correspond to the late declining to minimum stages of the cycle. During the declining phase of the solar cycle the Sun's magnetic field is well approximated by a dipole tilted with respect to the spin axis, the angle of inclination reducing as solar minimum is approached. Near solar maximum the field is more complex.

The solar wind originates in the corona, the outer atmosphere of the Sun, which is visible as a pearly halo (or crown) during a total eclipse. The photosphere has a temperature of ~ 6000 K, while that of the corona exceeds 10^6 K. As heat cannot flow directly from the cooler photosphere to the hotter corona, energy must be transferred from the solar interior by non-thermal processes. The difficulty of explaining the heating mechanism is known as the coronal heating problem and remains one of the major challenges of solar physics. Theories are of two main types: those involving dissipation of magnetic stresses, and those involving dissipation of waves. Temperatures are so high that

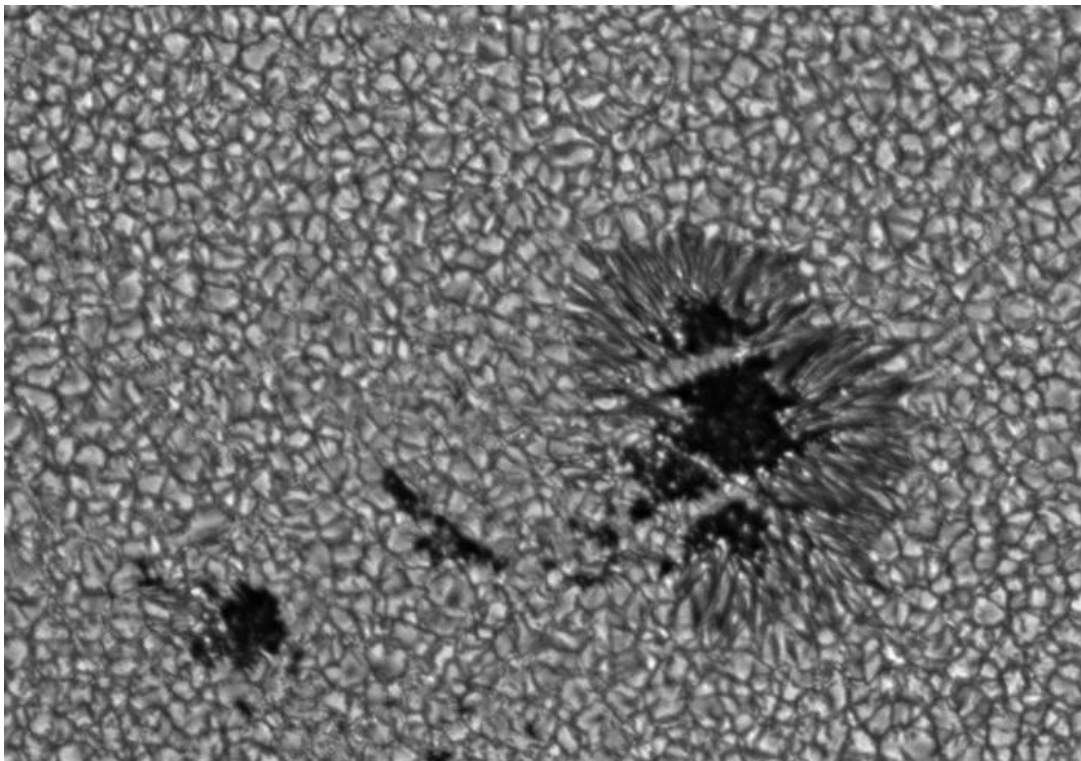


Figure 1.2 Sunspots and granules on the Sun's photosphere. [Courtesy NASA.]

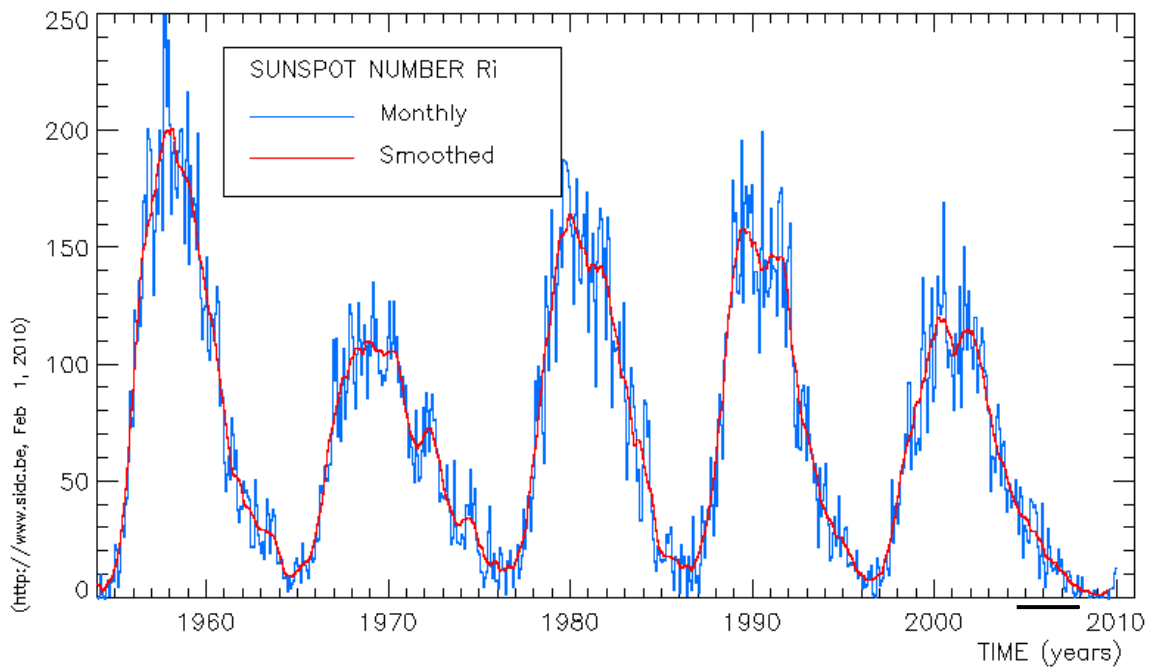


Figure 1.3 Monthly sunspot numbers for the last five solar cycles. [Courtesy Solar Influences Data Analysis Center.] The studies presented in this thesis use data obtained between mid-2004 and the end of 2007. This interval is marked by the black line below the horizontal axis.

the corona is not in hydrostatic equilibrium and plasma streams out into space at a rate of around one million tonnes per second. The solar wind is chiefly composed of fully ionised hydrogen and helium (with a much smaller proportion of heavier elements), with a He/H ratio that varies over the solar cycle, between $\sim 2\%$ and $\sim 5\%$ by number, the lowest values being observed around solar minimum [e.g. *Ogilvie and Hirshberg, 1974; Feldman et al., 1978; Aellig et al., 2001*].

On the spatial scales of the corona and solar wind, the plasma behaves as a nearly perfect conductor, such that to a first approximation the plasma and magnetic field are ‘frozen’ together. The energy density of a dipole field falls off rapidly with distance (as r^{-6}), so that, except within a few solar radii of the photosphere, the energy density of the magnetic field is low compared to that of the outflowing plasma, and the plasma carries the field lines with it. The foot of each field line remains frozen to the surface of the Sun and the combination of solar rotation and radial plasma outflow causes the lines to become wound into spirals, the curvature of which depends on the flow speed and the distance from the Sun. The angle formed by the spiral magnetic field and the solar wind direction is typically $\sim 45^\circ$ at Earth, increasing to $\sim 85^\circ$ at Saturn. Figure 1.4 shows the Parker spiral (named after Eugene Parker who first predicted the spiral configuration of the IMF) for a typical solar wind speed of 400 km s^{-1} .

The Parker spiral, though broadly confirmed by observations, is something of an idealization: in reality, solar wind speed is not constant but varies over a range of $\sim 300\text{-}750 \text{ km s}^{-1}$. The field lines are less tightly wound for higher speeds than for lower speeds. Figure 1.5 is an image obtained by a coronagraph instrument on the SOHO (Solar and Heliospheric Observatory) spacecraft, showing the structure of the corona. (A

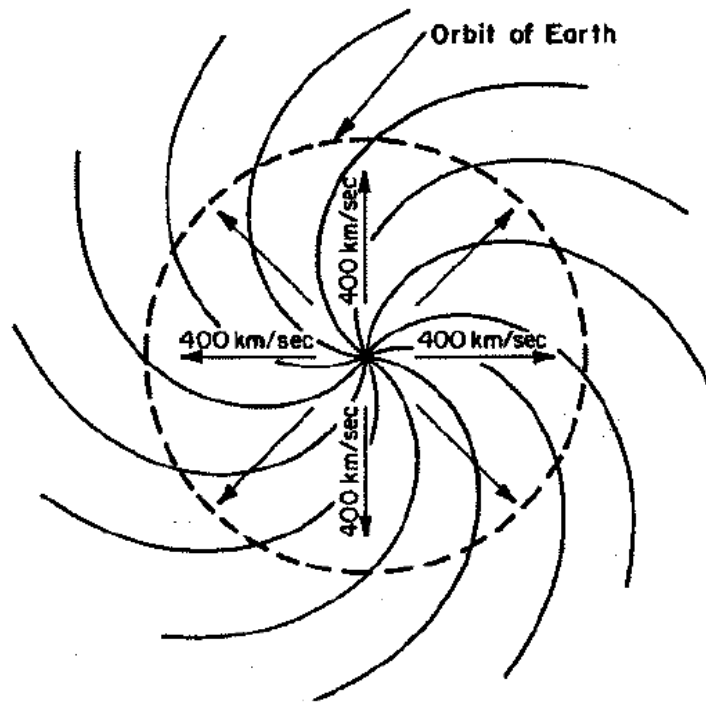


Figure 1.4 The Parker spiral for a solar wind speed of 400 km s^{-1} . [From *Hundhausen*, 1995.]

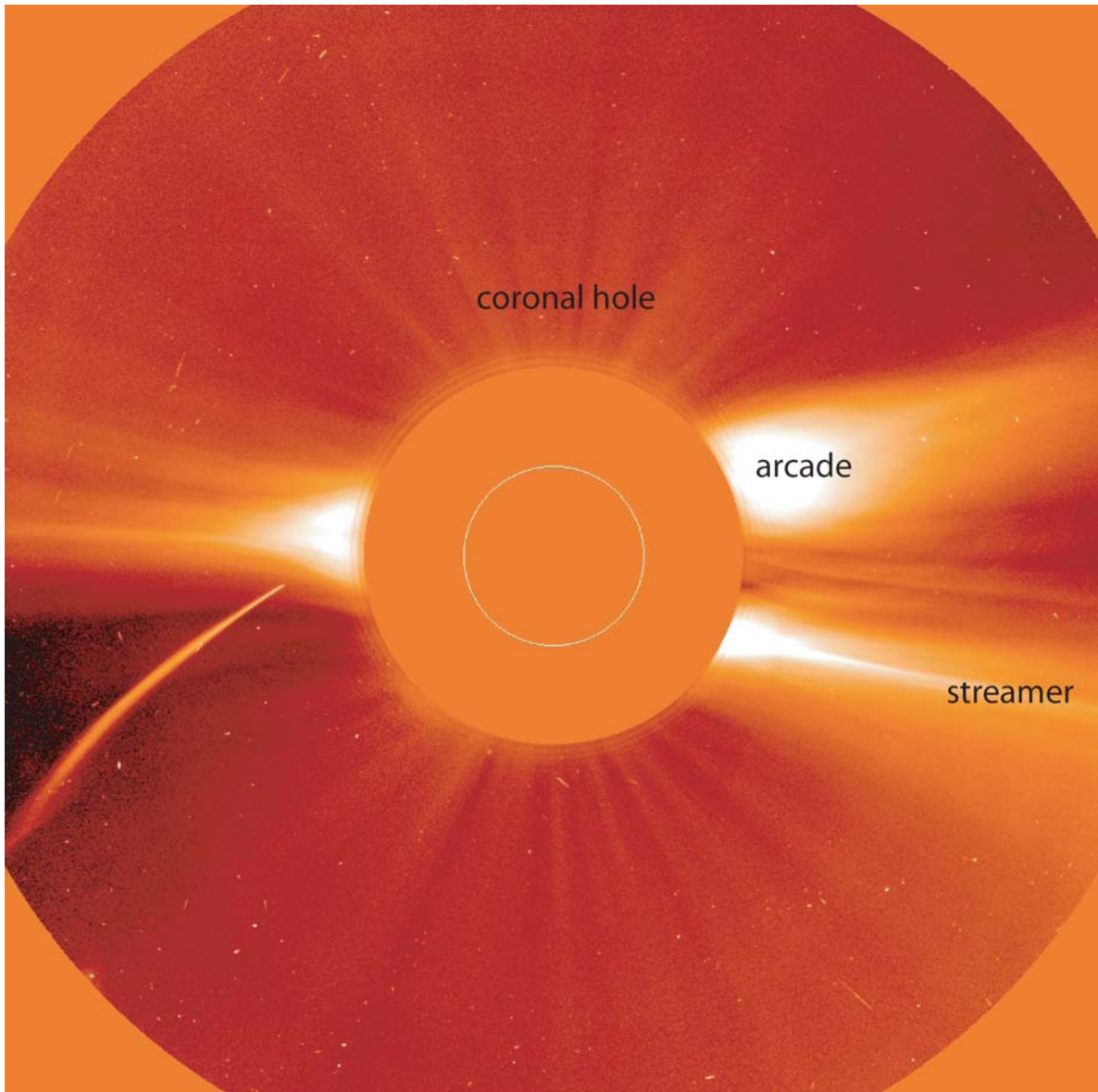


Figure 1.5 An image obtained by a coronagraph on the SOHO (Solar and Heliospheric Observatory) spacecraft, showing the low latitude coronal arcades and streamers and the high latitude coronal holes. The dust tail of the Comet SOHO-6 can also be seen on the left-hand side. [Courtesy ESA/NASA.]

coronagraph produces an artificial eclipse by blocking light from the Sun's disk.) Close to the Sun the magnetic energy density is greater than the plasma energy density so that the magnetic field constrains the plasma. Near the magnetic equator at low altitudes plasma is trapped on closed field lines, forming dense, bright arcades. Above the arcades the field weakens sufficiently for the plasma to flow outward as streamers. These streamers are the source of the denser, slower ($\sim 400 \text{ km s}^{-1}$) solar wind. At higher magnetic latitudes the dipole field is more radial and the plasma can escape more easily. Because these regions are tenuous and dim they are known as coronal holes. They are the source of the less dense, faster ($\sim 750 \text{ km s}^{-1}$) solar wind. During the declining phase of the solar cycle, when the tilt between the Sun's magnetic and spin axes is significant, flows from different magnetic latitudes and therefore with different characteristic speeds, are successively launched into any one radial direction. When fast wind follows slow wind (in a given direction), the fast flow catches up with and ploughs into the slower flow, forming high pressure compression regions in which the field strength and plasma density are increased. Low pressure rarefaction regions, in which the field strength and plasma density are reduced, are formed when slow wind follows fast wind. Although the solar wind plasma flows radially outward, the compressions and rarefactions approximately corotate with the Sun and are therefore known as corotating interaction regions (CIRs). The development of CIRs is illustrated in Figure 1.6, which shows a cut through the solar equatorial plane in the inner heliosphere. In this sketch the spirals represent magnetic field lines, while the black arrows indicate the radial outflow of the solar wind plasma. (The white arrows represent the pressure gradients associated with the CIRs.) At the orbits of Jupiter and Saturn, the interaction of fast and slow streams of solar wind produces a highly-structured heliosphere characterized by a repeating pattern of few-day compression regions and several-day

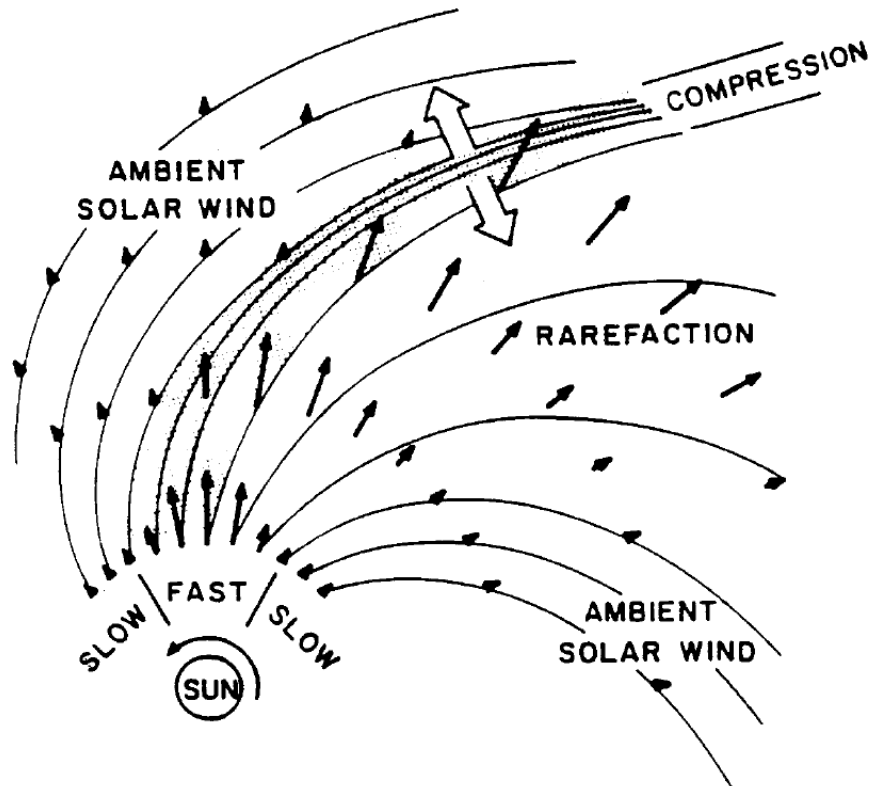


Figure 1.6 The development of corotating interaction regions (CIRs). The sketch shows a cut through the solar equatorial plane in the inner heliosphere. The spirals represent magnetic field lines, while the black arrows indicate the radial outflow of the solar wind plasma. (The white arrows represent the pressure gradients associated with the CIRs.)

[From *Gosling and Pizzo, 1999.*]

rarefaction regions. *Jackman et al.* [2008], in a study of 18 solar rotations between August 2003 and November 2004 using Cassini data, note that this pattern of compressions and rarefactions is pronounced during the declining phase of the solar cycle, but is less evident as conditions approach those of solar minimum and the dipole axis of the Sun becomes more closely aligned with the spin axis.

1.2 Planetary Magnetic Fields

Of the planets and major satellites within the solar system, Earth, Jupiter, Saturn, Uranus, Neptune, and the jovian moon Ganymede are known to possess global magnetic fields consistent with an active dynamo. Mercury also has a (weak) global field, perhaps produced by the decaying remains of a formerly more vigorous dynamo. The details of the dynamo mechanism at each body and the characteristics of the resulting field will depend on many factors, including (but not limited to) the size, composition, topology, rotational profile, and depth of the convection region. We will make only the briefest survey here, particularly as these remain matters of considerable uncertainty.

Planetary dynamos, like those of stars, arise from convective motions in conducting fluids. At Earth the conducting fluid is molten iron and nickel, while at Jupiter and Saturn it is composed of metallic H and He, and at Uranus and Neptune it is a partially metallised mixture of H₂O, NH₃, and CH₄ [e.g. *Stevenson*, 1983]. The convection in planets may be thermal or compositional, or some combination of the two. Thermal convection, which operates in the Sun and is also thought to dominate at Jupiter, is driven by a radial temperature gradient. In the giant planets the heat powering thermal convection may be primordial in origin (heat of formation) or that released by ongoing gravitational contraction. At Earth thermal convection is powered by a combination of primordial heat

and the radioactive decay of unstable isotopes. Compositional convection, which appears to be important at both Saturn and the Earth, involves gravitational differentiation of the planetary interior. At Saturn helium settles through hydrogen to join a growing helium-rich core, while at Earth a solid inner core grows at the expense of the fluid outer core and light elements mixed with the iron are excluded from the crystal structure and rise buoyantly through the outer core.

In spherical harmonic models the magnetic field of a planet is represented as a superposition of components of degree n and order m (where $n \geq 1$ and $0 \leq m \leq n$), i.e. as $\mathbf{B} = \sum_{n,m} \mathbf{B}_n^m$. (Note that this description arises for a field for which both divergence and curl are zero.) Components of degree 1 are dipolar, those of degree 2 are quadrupolar, and those of degree 3 are octupolar, etc. For each degree there is a dependence upon radial distance given by $r^{-(n+2)}$, such that well outside the region in which the field is generated the dipole field will dominate. The magnetic fields of planets are commonly represented as dipoles tilted with respect to the spin axis. The dipole tilt is 11° at Earth, $\sim 10^\circ$ at Mercury, 10° at Jupiter, and at Uranus and Neptune 59° and 47° , respectively.

Saturn's internally-generated magnetic field is found to be remarkably (indeed, seemingly impossibly) symmetric about the planet's spin axis, the dipole tilt being smaller than can be measured using data obtained to date but certainly less than $\sim 0.5^\circ$ [e.g. *Connerney et al.*, 1982; *Davis and Smith*, 1990; *Dougherty et al.*, 2005; *Giampieri et al.*, 2006]. This axisymmetry would appear to be forbidden by Cowling's theorem which disallows symmetry of a dynamo-generated magnetic field about any axis [*Cowling*, 1934, 1955]. *Stevenson* [1982] reconciles the observed axisymmetry of the field with Cowling's theorem by proposing that differential rotation in a conducting but non-convecting shell

above the dynamo region attenuates the non-axisymmetric components of the field. The shell is associated with the previously mentioned rain-out of helium and has no equivalent at Jupiter. Figure 1.7 shows the model interiors of Jupiter and Saturn, Stevenson's shell being represented by the dotted region. Using numerical dynamo models *Stanley* [2010] has demonstrated that differential rotation in a Stevenson-type shell due to thermal winds driven by the type of latitudinal temperature differences expected at Saturn (hotter at the equator, colder at the poles) can indeed increase a field's axisymmetry.

At Jupiter, because the magnetic dipole axis is tilted by 10° with respect to the spin axis, there is also a 10° tilt between the magnetic and rotational equatorial planes. At a given position, the magnetic equatorial plane containing the plasma sheet wobbles up and down at the planetary period (~ 10 h). This can be seen in Figure 1.8 [from *Bunce and Cowley, 2001*], which uses data obtained by *Voyager-2* when the spacecraft was located in Jupiter's middle magnetosphere near the (rotational) equatorial plane. The top panel shows the spacecraft's motion above and below the magnetic equator ($z = 0$). The remaining panels give the components of the magnetic field in cylindrical coordinates. The radial (ρ) component is positive when the spacecraft is above the magnetic equator and negative when below it. It can be seen that the spacecraft crosses the current sheet twice per rotation period. At Saturn we have the difficulty of explaining what, in the absence of a dipole tilt, is responsible for the abundance of oscillatory phenomena observed with periods near to that of planetary rotation. We will return to this issue in Chapter 2.

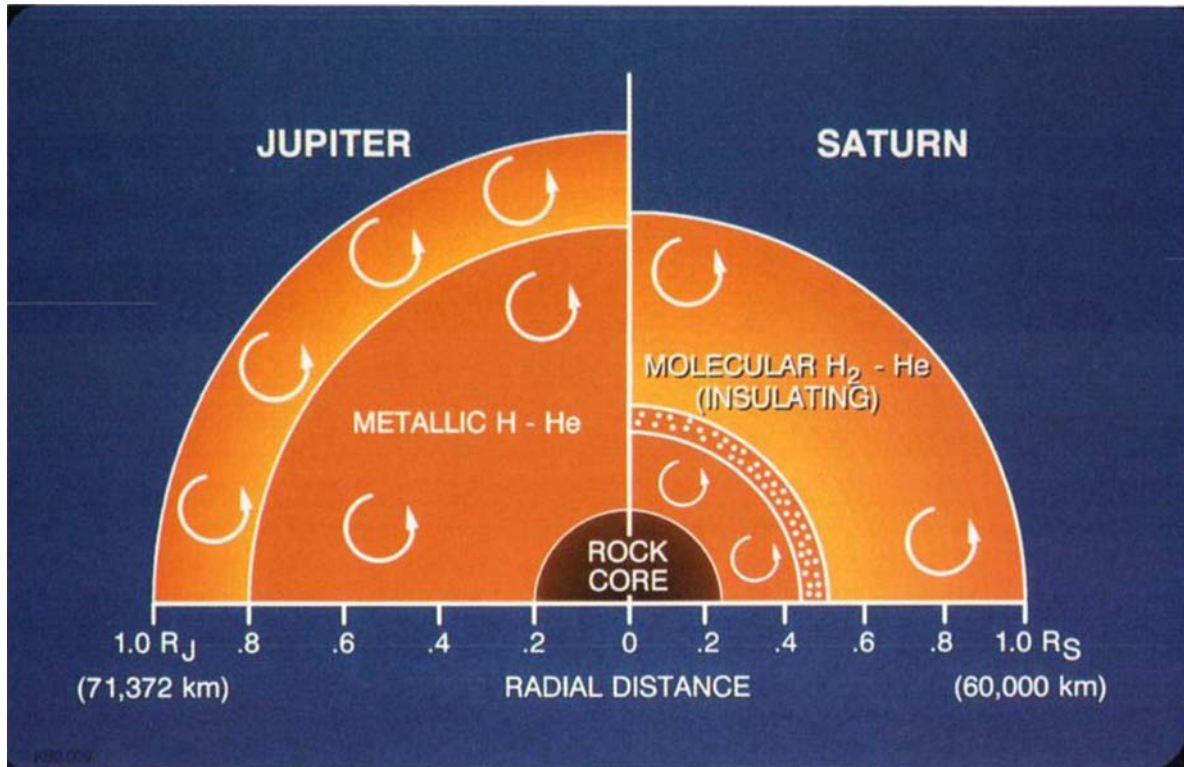


Figure 1.7 A schematic of the model interiors of Jupiter and Saturn. Both planets have a conducting and convecting outer core of metallic H - He, and an outer envelope of convecting H₂ - He. Saturn is shown with the non-convecting, but metallically conducting, shell proposed by *Stevenson* [1982]. [From *Connerney et al.*, 1993.] (Note that the currently accepted value for Saturn's equatorial radius is 60,268 km.)

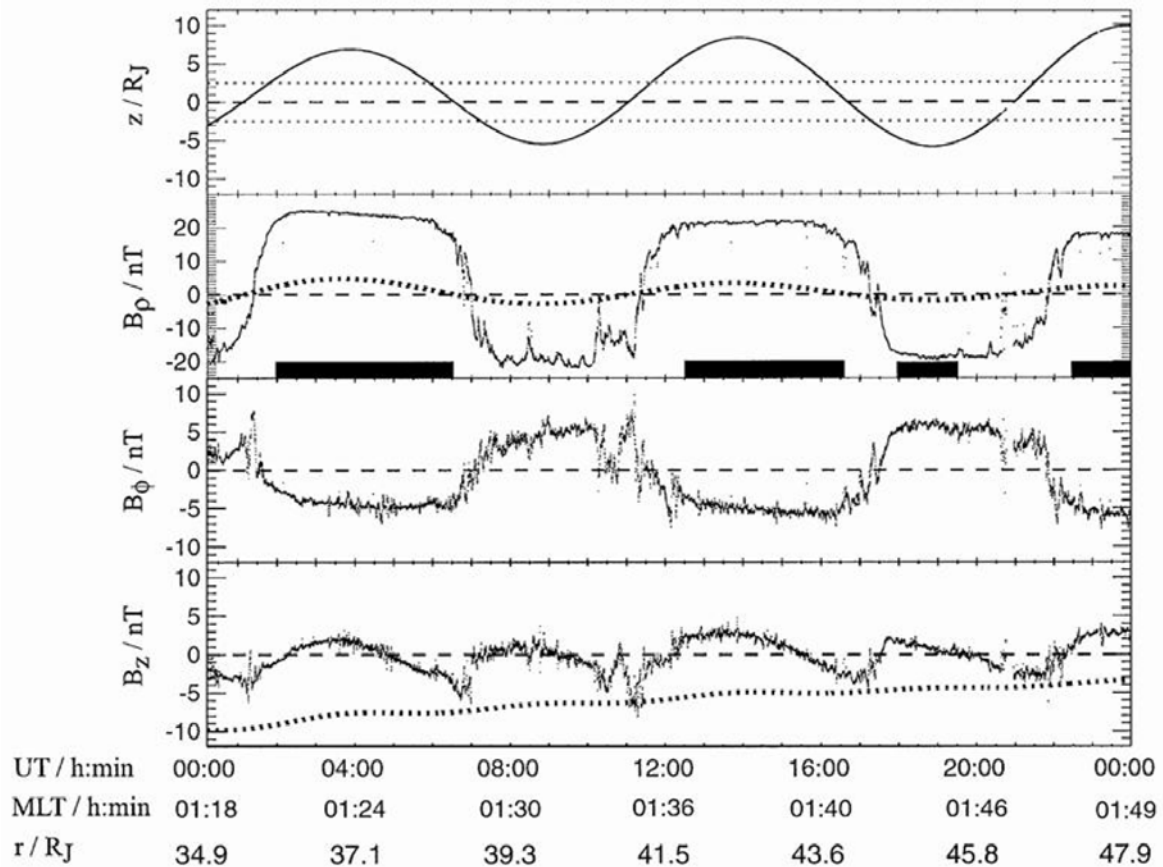


Figure 1.8 The figure shows data obtained by Voyager-2 on day 193 of 1979 when the spacecraft was located in Jupiter’s middle magnetosphere near the (rotational) equatorial plane. The top panel shows the spacecraft’s distance from the magnetic equatorial plane, while the remaining three panels show the radial (ρ), azimuthal (ϕ), and vertical (z) components of the magnetic field in cylindrical coordinates referenced to the planet’s magnetic axis. The dotted curves in the second and fourth panels represent the contribution of the internal planetary field derived from the VIP 4 model of *Connerney et al.* [1998]. Spacecraft positional information is given at the bottom of the plot, specifically magnetic local time (MLT), and radial distance from the centre of the planet. [From *Bunce and Cowley*, 2001.]

1.3 Planetary Magnetospheres and Bow Shocks

We now consider the interaction of the solar wind and IMF with magnetized planets. The magnetosphere is a magnetic cavity or bubble in the solar wind. As the solar wind is frozen to the IMF and the planetary plasma is frozen to the planetary field, the two plasmas must remain separate, to a first approximation. The solar wind is deflected around the magnetic obstacle and a current sheet, named the Chapman-Ferraro current (after the scientists who first proposed the existence of the Earth's magnetosphere), forms at the interface of the two plasmas. (The existence of the current sheet is a consequence of Ampère's law which states that where there is a curl in \mathbf{B} , a current must flow.) This current sheet is the magnetopause, which defines the outer boundary of the magnetosphere, the sphere of influence of the planet's magnetic field. The magnetosphere is compressed by the solar wind pressure on the dayside, but extends to form a long tail on the nightside. Because the solar wind is highly supermagnetosonic, a standing shock wave, the bow shock, forms upstream of the magnetosphere. The solar wind plasma is slowed, compressed, and heated as it crosses the bow shock. The shocked solar wind plasma is called the magnetosheath. Figure 1.9 shows a sketch of the terrestrial system, in which the inner and outer plain dashed lines represent the magnetopause and bow shock, respectively, the arrowed dashed lines indicate plasma flow, and the arrowed solid lines represent magnetic field lines.

The size and shape of a planetary magnetosphere are determined by pressure balance at the magnetopause. The total pressure exerted by the solar wind is given by

$$P_{SW, total} = P_{dynamic} \cos^2 \psi + P_{thermal} + P_{magnetic} \quad , \quad (1.1)$$

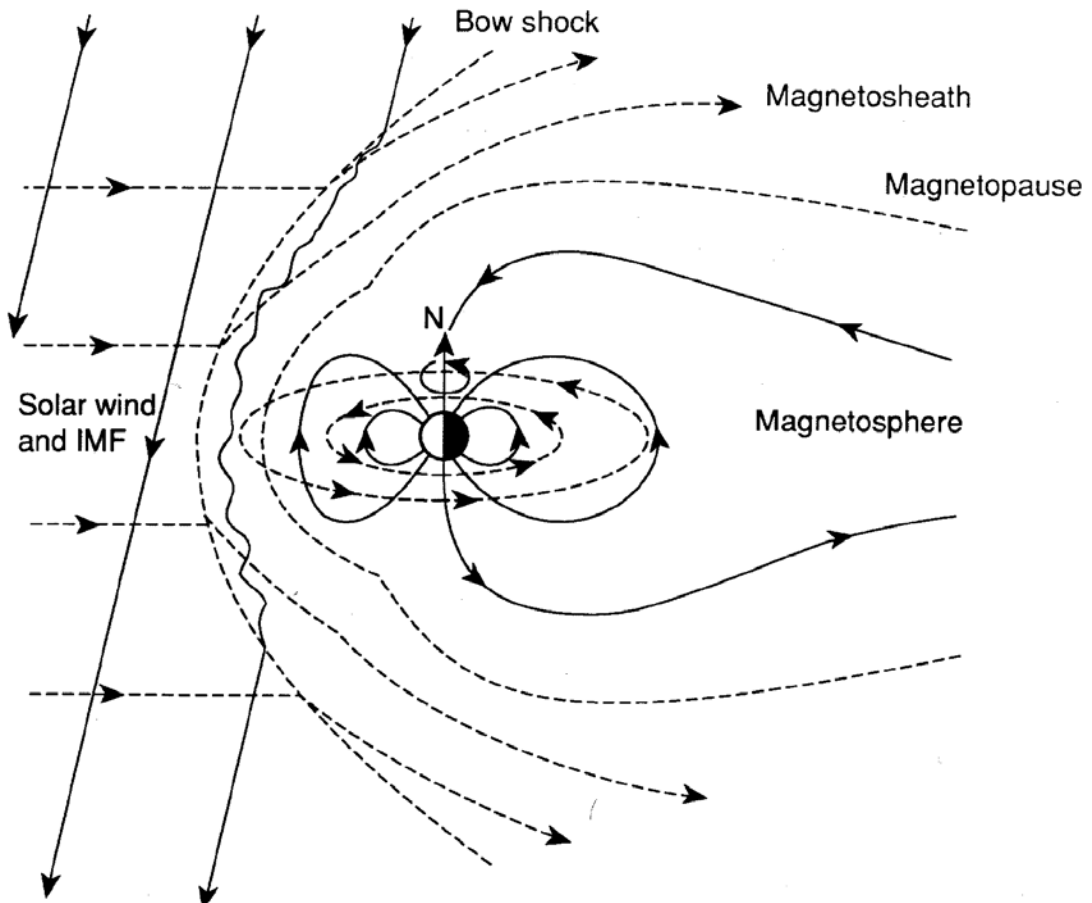


Figure 1.9 A sketch of the terrestrial magnetosphere. The inner and outer plain dashed lines represent the magnetopause and bow shock, respectively, the arrowed dashed lines indicate plasma flow, and the arrowed solid lines represent magnetic field lines. [From Cowley, 1991.]

where ψ is the angle between the flow and the normal to the magnetopause. At the subsolar magnetopause the flow is perpendicular to the boundary ($\psi = 0$), but away from the nose the effective dynamic pressure falls off as $\cos \psi$ decreases, such that the magnetopause flares out. Inside the magnetosphere the total pressure is some combination of magnetic pressure and plasma pressure, the relative importance of the two depending on the planet and also varying over time with conditions within the magnetosphere. In the upstream solar wind, the dynamic pressure of the flow dominates, the thermal and magnetic pressures making only minor contributions to the total. When the solar wind crosses the bow shock, the dynamic pressure is converted into an equivalent thermal and magnetic pressure, in a process termed thermalization. At the subsolar magnetopause, it is this thermal and magnetic pressure that balances the magnetospheric pressure, as illustrated schematically in Figure 1.10. As the shocked plasma flows around the flanks of the magnetopause, the speed of the flow increases (becoming supermagnetosonic again at solar zenith angles of $\sim 40^\circ - 50^\circ$) and the thermal and magnetic pressures are converted back to dynamic pressure, though the increase in entropy at the shock means that this reversal cannot be complete.

Noting that the combined thermal and magnetic pressure in the subsolar magnetosheath is approximately equal to the dynamic pressure in the solar wind upstream of the bow shock, and assuming that plasma pressure in the magnetosphere near the magnetopause is negligible, the relationship between the internal and external pressures at the subsolar magnetopause can be simplified to

$$P_{SW} \approx B_{MP}^2 / 2\mu_0 , \quad (1.2)$$

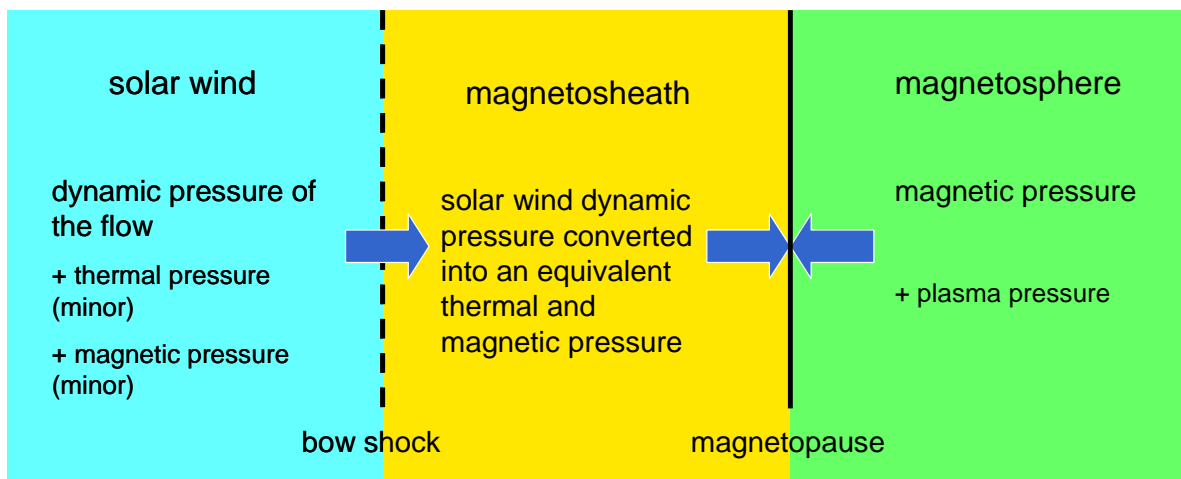


Figure 1.10 A schematic of pressure balance at the subsolar magnetopause.

where P_{SW} is the solar wind dynamic pressure, B_{MP} is the field strength just inside the equatorial magnetopause, and μ_0 is the permeability of free space. As discussed in section 1.2, a dipole field varies as the inverse cube of radial distance so that

$$B_{MP} \approx 2B_{eq}/R_{MP}^3, \quad (1.3)$$

where B_{eq} is the field strength at the planet's equator, and R_{MP} is the standoff distance (the distance between the centre of the planet and the nose of the magnetopause) in planetary radii. The factor of 2 comes from the fact that the Chapman-Ferraro current generates a magnetic field that has the effect of strengthening the field inside the magnetopause boundary to approximately twice the undisturbed dipole value. Combining equations (1.2) and (1.3) yields

$$P_{SW} \approx 2B_{eq}^2/\mu_0 R_{MP}^6, \quad (1.4)$$

and

$$R_{MP} \approx \left(\frac{2B_{eq}^2}{\mu_0 P_{SW}} \right)^{\frac{1}{6}}. \quad (1.5)$$

The sixth root indicates that the magnetopause standoff distance is relatively insensitive to changes in solar wind pressure.

For a closer correspondence to reality, the above simple analysis should be modified in two respects. Firstly, magnetospheric plasma pressure should be included. At Jupiter plasma pressure significantly increases the standoff distance, and as we will show in Chapter 4, periodic variations in the plasma pressure in Saturn's outer magnetosphere produce corresponding motions of the magnetopause boundary. The right-hand side of equation (1.2) could be modified to take account of internal plasma pressure. Indeed, we make use of such an equation in Chapter 4. Secondly, a fuller account should be taken of

the modification of the magnetic field inside the boundary by internal plasma currents. Our simple analysis included the effect of the Chapman-Ferraro current, but neglected the contribution of the ring current. The latter effect can be thought of as being due to an additional magnetic moment of the plasma associated with the ring current which increases the field at large distances beyond the ring current. The effect of both the plasma pressure and these internal plasma currents is to push the boundary further out. If the moment associated with the ring current is constant, the standoff distance (although having a value greater than that given by the unmodified equation (1.5)) will still vary with solar wind dynamic pressure as $P_{SW}^{-1/6}$. However, if the moment varies with the system size, then the exponent, which describes the compressibility of the magnetosphere, will be modified. Notably, *Bunce et al.* [2007, 2008a] found that at Saturn the moment associated with the ring current increases with the expansion of the magnetosphere resulting in a more compressible magnetosphere. (This will be discussed in more detail in Chapter 2.)

Empirical modelling of the magnetopause boundary position has shown that while the terrestrial magnetosphere does have a low compressibility reasonably consistent with an exponent of $-1/6$ [e.g. *Shue et al.*, 1997], for the jovian magnetosphere exponents ranging between $-1/5$ and $-1/4$ [*Slavin et al.*, 1985; *Huddleston et al.*, 1998; *Joy et al.*, 2002] indicate a significantly greater degree of compressibility. The compressibility of the saturnian magnetosphere appears to be intermediate between the terrestrial and jovian cases, the exponents ranging from $-1/6.1$ [*Slavin et al.*, 1983], to $-1/5.0$ [*Kanani et al.*, 2010], and $-1/4.3$ [*Arridge et al.*, 2006]. In the outer heliosphere, interactions between fast and slow solar wind streams (as mentioned in section 1.1) result in a solar wind dynamic pressure that is highly variable over time. This variability combined with the

enhanced compressibility of the magnetospheres causes standoff distances to vary by a factor of ~ 3 at Jupiter and up to ~ 2 at Saturn.

Figure 1.11 shows the relative sizes of the magnetospheres of the magnetized planets. Saturn and Jupiter have large magnetospheres because they have large magnetic dipole moments (~ 600 and $\sim 20,000$ times that of the Earth, respectively) and because the mean solar wind dynamic pressure is much less than at Earth. Dynamic pressure is given by the product of the solar wind's mass density and the square of its bulk flow speed. While the typical speed of the solar wind varies little with distance from the Sun, the mean density falls as $1/r^2$ and hence the dynamic pressure shows the same inverse square dependence on distance. At Saturn, with an orbital distance of ~ 9.5 AU, the mean solar wind dynamic pressure is therefore only around one hundredth of the value at the Earth.

The location of the bow shock chiefly depends on the size and shape of the dayside magnetosphere (these being determined by pressure balance at the magnetopause as outlined above) and the upstream solar wind magnetosonic Mach number (the ratio of the bulk flow speed to the speed of the fast magnetosonic wave). The jovian and saturnian subsolar magnetosheaths are found to be thinner than would be expected if the magnetospheric obstacle was axisymmetric about the Sun-planet line. This is suggestive of magnetospheres that are equatorially broadened by strong ring current systems such that they present a more streamlined shape to the solar wind flow and the shock can stand closer to the magnetosphere [Slavin *et al.*, 1985; Stahara *et al.*, 1989]. Solar wind magnetosonic Mach number is a function of the speed, density, and temperature of the solar wind, and the direction and strength of the IMF, all of which vary over time. The location of the bow

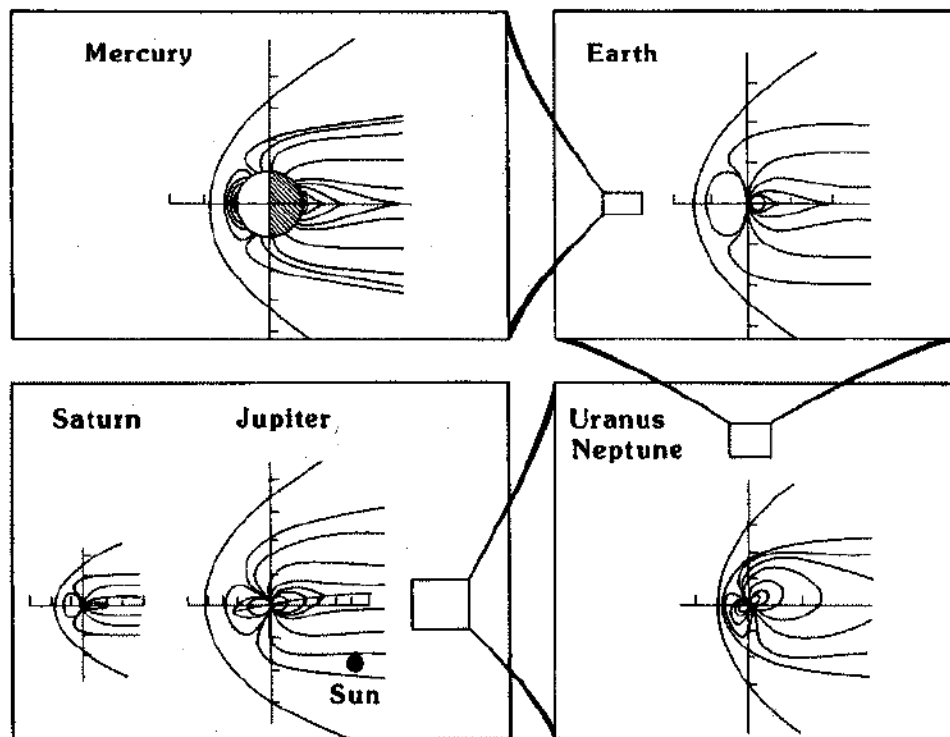


Figure 1.11 The relative sizes of the magnetospheres of the magnetized planets. [From *Russell and Walker, 1995.*]

shock is consequently much more sensitive to upstream conditions than that of the magnetopause.

Chapter 2

The Saturnian Magnetosphere

2.1 Introduction to the Saturnian System

Saturn is the second largest planet in the solar system (after Jupiter) with a radius nearly 10 times that of the Earth and a mass ~ 95 times greater. Both its composition, of $\sim 75\%$ hydrogen and $\sim 25\%$ helium by mass with traces of other elements, and its internal structure (discussed in Chapter 1, see Figure 1.7) are similar to those of Jupiter. Saturn rotates rapidly with a period of less than 11 h (we return to the issue of rotation in section 2.2) with the result that the planet bulges at the equator and is flattened at the poles, the degree of dynamical flattening being $\sim 10\%$. Throughout this thesis it is the equatorial radius at a pressure of 1 bar, 60,268 km, that we use for the planet's radius, R_S . Saturn orbits the Sun at a mean distance of ~ 9.5 AU with a period of ~ 29.5 years. Because there is a significant tilt of $\sim 27^\circ$ between the planet's equatorial and orbital planes, Saturn, like the Earth, experiences seasons. The data used in this thesis were obtained under conditions of southern hemisphere summer / northern hemisphere winter.

Figure 2.1 shows Saturn's ring structure and some of the planet's many moons. Of particular interest is Enceladus, a small (radius ~ 500 km) but cryovolcanically active moon with an orbital radius of $3.9 R_S$. Lineaments named 'tiger stripes' in the moon's southern polar region are associated with plumes of water vapour and dust particles [*Porco et al.*, 2006] (see Figures 2.2 and 2.3). These plumes are the source of the radially extended E-ring, the brightness of which peaks at the orbit of Enceladus, and of most of the water-group plasma in Saturn's magnetosphere. Ionisation of the neutral gas leads to plasma



Figure 2.1 Saturn's ring structure and moons. [Courtesy NASA/JPL.]

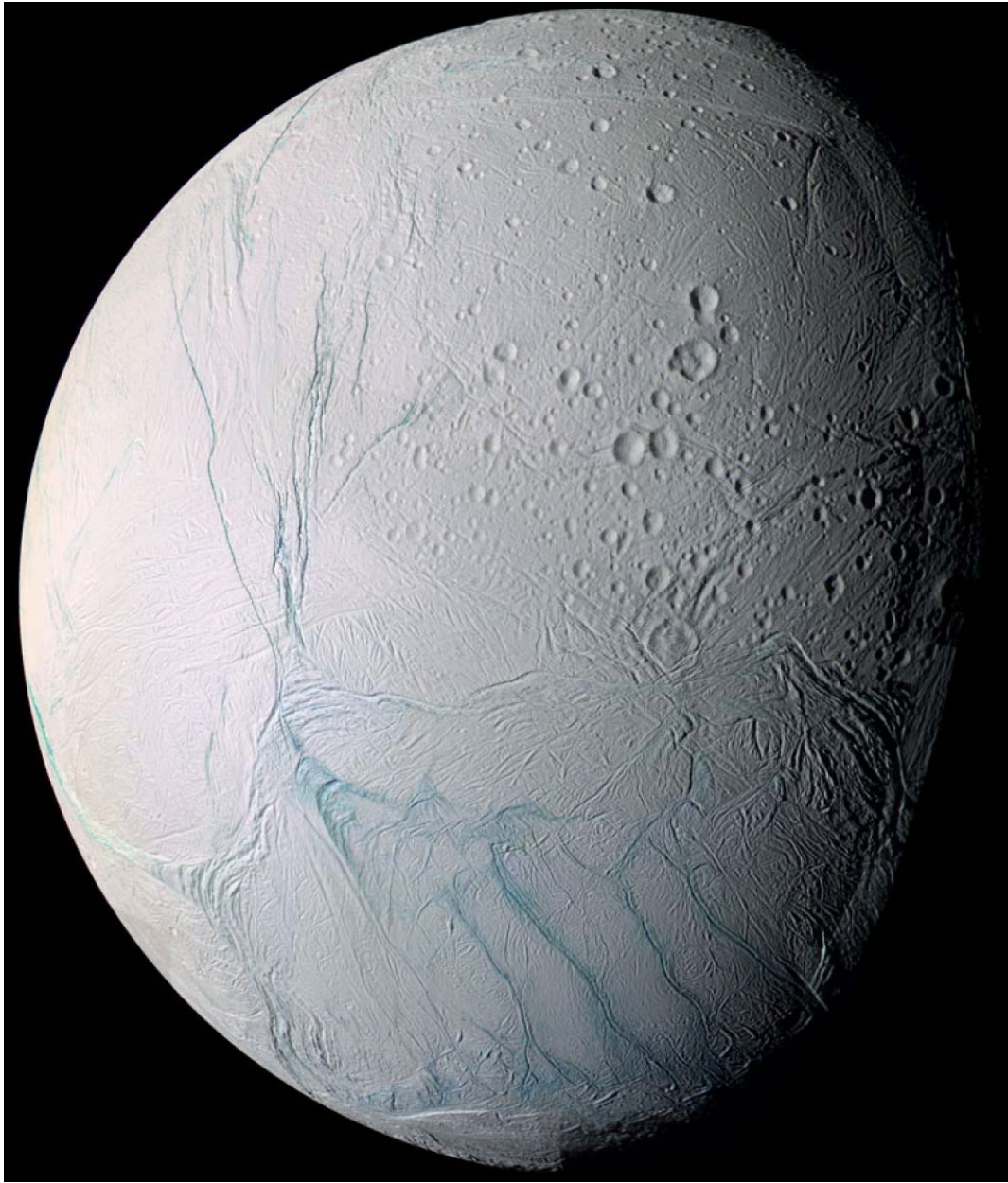


Figure 2.2 A Cassini image of Enceladus in which the ‘tiger stripes’ are visible in false-colour blue. [Courtesy NASA/Cassini Imaging Team.]

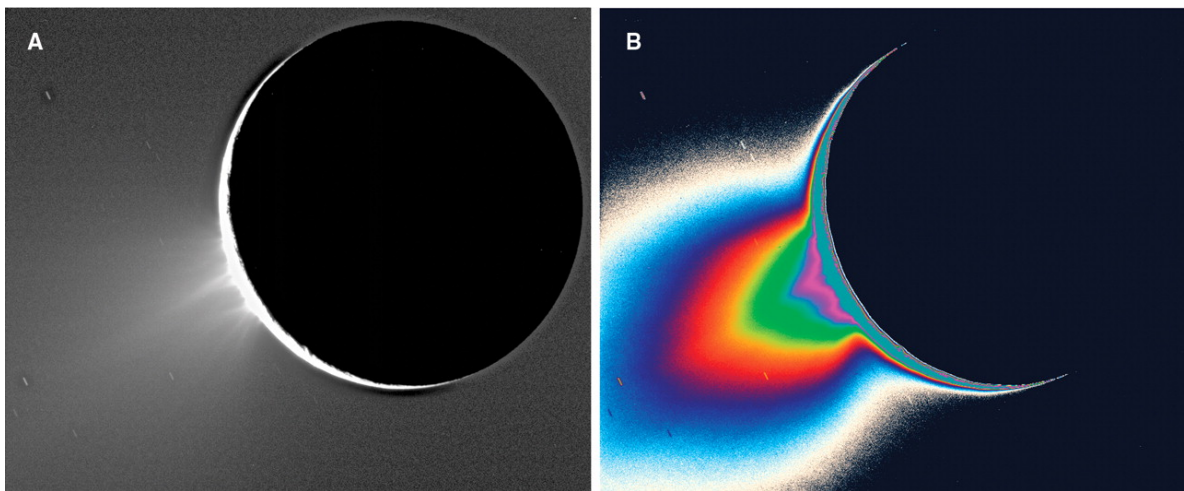


Figure 2.3 (A) Cassini image of Enceladus' water-ice plumes in which the south pole points towards the lower left. Individual jets can be clearly distinguished. (B) The image has been colour-coded according to light level in order to enhance the visibility of the fainter component and indicate its large extent. [From *Porco et al.*, 2006.]

mass loading of field lines. *Tokar et al.* [2006] and *Pontius and Hill* [2006] have estimated the mass loading rate, which can be treated as a proxy for the outgassing rate, as $\geq 100 \text{ kg s}^{-1}$. Based upon a study of absorption microsignatures, *Jones et al.* [2006] have reported substantial variability in the outgassing rate on timescales of days or weeks.

Figure 2.4 shows a sketch of the configuration of Saturn's magnetosphere under southern summer conditions, in a cut through the noon-midnight meridian plane with the solar wind blowing from right to left. The black dot-dashed line represents the magnetopause, and the solid black lines indicate magnetic field lines. (The polarity of the saturnian dipole is opposite to that of the Earth i.e. the field lines point southwards at the equator.) The blue dotted region represents cool ($\sim 1 \text{ eV}$ to a few tens of eV) water-group plasma evolved from sources in the inner magnetosphere, principally Enceladus. Rapid rotation of the plasma with the planet generates centrifugal forces that drive interchange motions that transport the plasma outward while confining it near the equatorial plane. (We will have more to say about the Enceladus plasma torus in Chapter 6.) The red dotted region represents warm and hot ($\sim 1 \text{ keV}$ to several tens of keV) plasma which is transported inward from the outer magnetosphere. The purple dotted region indicates a radiation belt of high-energy particles, the extent of which is restricted in the inner region by the presence of Saturn's main ring system, the latter being represented by the green lines on either side of the planet. Note that because the planet's spin axis is tilted away from the solar wind flow, the magnetic equator represented by the dashed line is displaced northward of the rotational equator in the outer magnetosphere on both the dayside and the nightside.

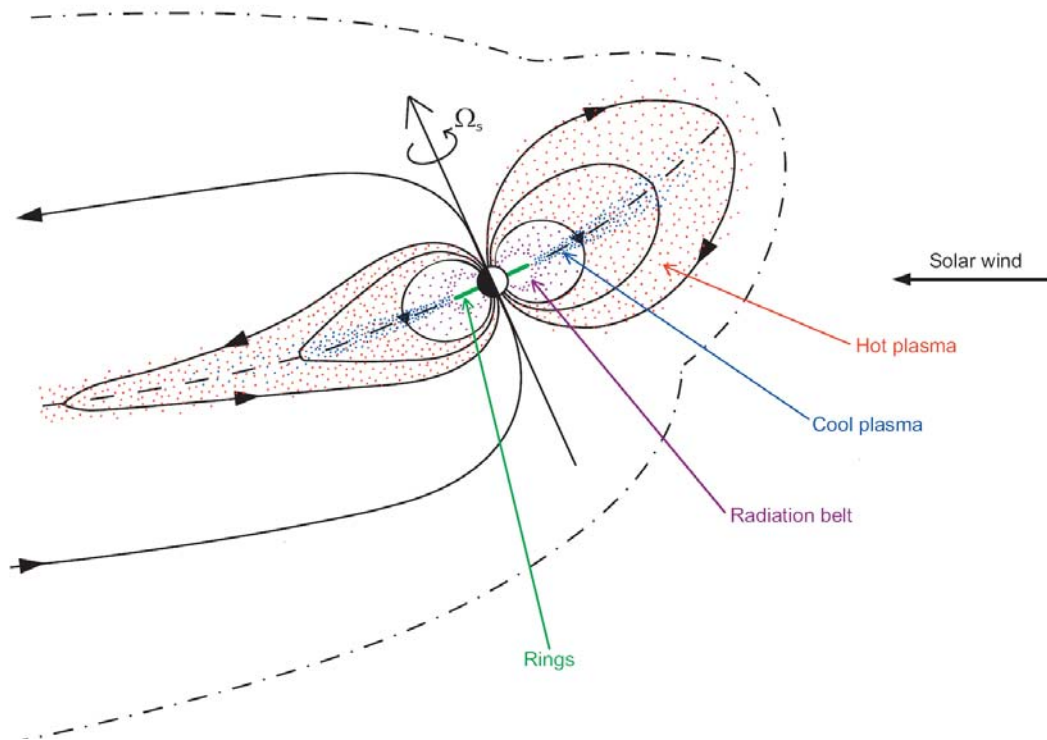


Figure 2.4 This sketch of the configuration of Saturn's magnetosphere under southern summer conditions shows a cut through the noon-midnight meridian plane with the solar wind blowing from right to left. The black dot-dashed line represents the magnetopause and the solid black lines indicate magnetic field lines. The effect of the ring current, an eastward flowing disk of current in the middle magnetosphere, is apparent in the distension of the equatorial field lines away from the planet. The blue dotted region represents cool water-group plasma centrifugally confined near the equatorial plane, the red dotted region represents warm and hot plasma, the purple dotted region indicates a radiation belt of high-energy particles, and the green lines on either side of the planet represent the main ring system. Because the planet's spin axis is tilted with respect to the solar wind flow, the magnetic equator represented by the dashed line is displaced northward of the rotational equator in the outer magnetosphere. [From *Kellett et al.*, 2009.]

The effect of the ring current, an eastward flowing disk of current in the middle magnetosphere, is apparent in the distension of the equatorial field lines away from the planet. The size and strength of the ring current system are found to increase with the expansion of the magnetosphere [Bunce *et al.*, 2007]. The middle magnetosphere has a quasi-dipolar configuration when the magnetosphere is strongly compressed and extends into a magnetodisc when the magnetosphere is strongly expanded [Bunce *et al.*, 2008a]. This has the effect of enhancing the compressibility of the magnetosphere. When the magnetosphere expands in response to a weakening of the solar wind dynamic pressure, the size and strength of the ring current increases, which pushes the boundary even further out. When the magnetosphere contracts in response to a strengthening of the solar wind dynamic pressure, the size and strength of the ring current decreases, which causes the boundary to move even further inward. Physically, the ring current is produced by the differential drift of ions and electrons associated both with the plasma centrifugal force mentioned above and with energy-dependent drifts of both the warm and hot plasma [e.g. Achilleos *et al.*, 2009; Kellett *et al.*, 2010].

Prior to the arrival of Cassini in July 2004, Saturn had been visited by three spacecraft. Flybys of the planet were made by Pioneer-11 in September 1979, Voyager-1 in November 1980, and Voyager-2 in August 1981. The trajectories are shown in Figure 2.5 [from Dougherty *et al.*, 2004], projected onto Saturn's equatorial plane. Observed crossings of the magnetopause (M) and bow shock (S) are indicated by rectangles and circles, respectively. Average modelled magnetopause and bow shock boundaries from Bridge *et al.* [1982] are superposed. All three spacecraft entered the magnetosphere near the noon meridian, with Pioneer-11 and Voyager-2 exiting near dawn and Voyager-1

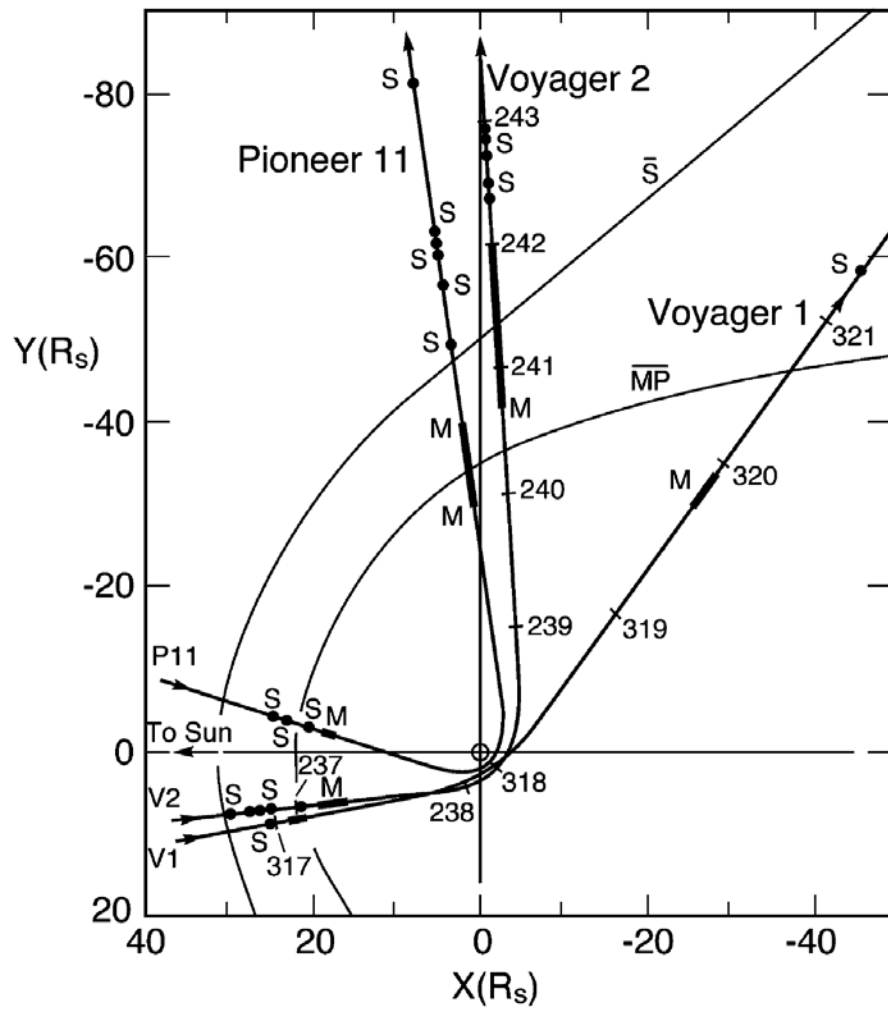


Figure 2.5 The figure shows the trajectories of Pioneer-11, Voyager-1, and Voyager-2 projected onto Saturn's equatorial plane. Observed crossings of the magnetopause (M) and bow shock (S) are indicated by rectangles and circles, respectively. Average modelled magnetopause and bow shock boundaries from *Bridge et al.* [1982] are superposed. [From *Dougherty et al.*, 2004.]

emerging further down the tail. Pioneer-11 remained close to the equatorial plane throughout the flyby, while Voyager-1 maintained low latitudes on the inbound portion of the pass and large northerly latitudes outbound, and Voyager-2 kept to high latitudes (northerly inbound, southerly outbound) except near periapsis. These flybys vastly increased our knowledge of the saturnian system but their spatial and temporal coverage was necessarily very limited. At the time of writing (March 2010) Cassini has been orbiting Saturn for nearly six years, and the studies in this thesis use data from orbits spanning an interval of three and a half years. We will discuss Cassini's orbital tour in more detail in Chapter 3.

Several models of Saturn's internally-generated magnetic field have been developed based upon magnetic data obtained close to periapsis. These include the Z3 model [Connerney *et al.*, 1982] derived from Voyager 1 and 2 observations, the SPV model [Davis and Smith, 1990] which uses all available pre-Cassini data, and the Cassini-SOI model [Dougherty *et al.*, 2005] which uses data obtained during Cassini's orbital insertion (periapsis at $\sim 1.33 R_S$). All of these models are zonal harmonic models of degree 3 (up to octupolar). A zonal harmonic model is a spherical harmonic model (see section 1.2) in which only axisymmetric ($m = 0$) components have non-zero values. Burton *et al.* [2009] have most recently published a model, also zonal harmonic of degree 3, based on data from 45 periapsis passes occurring during the first three years of Cassini's tour of Saturn. Comparing their data with that obtained by Pioneer-11 and Voyager 1 and 2, they note that there is little evidence for secular variation in the internal field over the ~ 30 years since observations were first made.

2.2 *Magnetospheric Period Phenomena at Saturn*

Despite the remarkable symmetry of Saturn's internally-generated magnetic field, oscillations in the magnetic field, plasma particles, and radio emissions at a period close to the planetary rotation period (~ 10.8 h) have been found to be ubiquitous within the planet's magnetosphere. The first of these phenomena, observed by the Voyager spacecraft, was the intensity modulation of Saturn kilometric radiation (SKR) [*Kaiser et al.*, 1980; *Warwick et al.*, 1981; *Desch and Kaiser*, 1981; *Lecacheux and Genova*, 1983; *Galopeau et al.*, 1995; *Zarka*, 1998]. These non-thermal radio emissions are believed to be generated by precipitating auroral electrons principally in the high-latitude pre-noon sector, through the cyclotron maser instability. The modulation is 'strobe-like' in that the temporal variations in emitted power are independent of the position of the observer. The period was initially taken to define the rotation period of the planet's interior e.g. through emission modulation by a rotating magnetic anomaly (undetected directly), but subsequent analysis of Ulysses and Cassini data has shown that the SKR period varies by $\sim 1\%$ on few-year timescales [*Galopeau and Lecacheux*, 2000; *Gurnett et al.*, 2005; *Kurth et al.*, 2007, 2008], this being much too large a variation to be associated directly with the planet. Here we therefore refer to this slowly-varying period as the 'magnetospheric period'. It has recently been discovered that the SKR power modulations occur at somewhat differing periods in the two hemispheres, at ~ 10.6 h for northern sources and ~ 10.8 h for southern sources during the recent epoch investigated using data from the Cassini orbiter [*Kurth et al.*, 2008; *Gurnett et al.*, 2009]. However, the data examined in the studies presented in this thesis clearly relate to the dominant longer southern period, corresponding to the summer hemisphere at Saturn over the interval considered (2004-2007).

The Pioneer-11 and Voyager flybys also provided initial evidence for related oscillations in magnetospheric particle and field data. *Carbary and Krimigis* [1982] reported periodic variations in Voyager energetic ion and electron spectra which they linked to the SKR modulations, while *Espinosa and Dougherty* [2000, 2001] and *Espinosa et al.* [2003a,b] identified magnetic oscillations in both Pioneer-11 and Voyager data, and showed via their polarization that the perturbations were not due to a rotating tilted planetary dipole. More recently, these results have been expanded upon using data from the Cassini orbiter [e.g. *Krimigis et al.*, 2005; *Krupp et al.*, 2005; *Giampieri et al.*, 2006; *Carbary et al.*, 2007a, 2007b, 2008a; *Burch et al.*, 2009].

Cassini observations have shown that in contrast to the ‘strobe-like’ SKR modulation, particle and field oscillations rotate around the planet and also propagate radially away from it, leading to oscillation ‘phase fronts’ that spiral slowly outward from the planet [*Cowley et al.*, 2006; *Gurnett et al.*, 2007; *Carbary et al.*, 2007c; *Andrews et al.*, 2008, 2010], as illustrated in Figure 2.6. *Cowley et al.* [2006] demonstrated that the observed oscillations are not fixed at the magnetospheric period but are Doppler shifted in a manner consistent with spacecraft motion through a spiral wave field. Figure 2.7 shows data from the fluxgate sensor of the Cassini magnetic field investigation [*Dougherty et al.*, 2004] obtained during days 65-72 of 2005. The three panels show the radial (r), colatitudinal (θ), and azimuthal (φ) components of the magnetic field in spherical polar coordinates referenced to the planet’s spin/magnetic axis, from which the SPV internal field [*Davis and Smith*, 1990] has been subtracted. Oscillations of varying period are clearly visible in the radial and azimuthal components. Inbound and outbound magnetopause crossings (MP) and periapsis (PA) are marked with arrows, and the oscillations, delimited

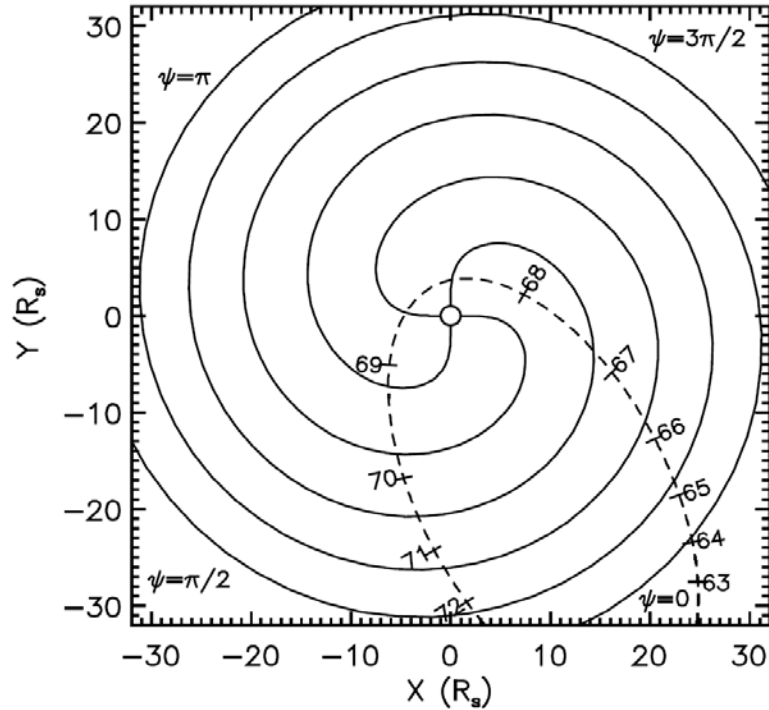


Figure 2.6 The figure shows instantaneous phase fronts of the wave, the spiral form of which results from the rotation of the source (at the magnetospheric period) combined with outward radial propagation (at the Alfvén speed, used as a reasonable approximation to the fast mode speed). The wave phase ψ changes by $\pi/2$ radians between each front. Cassini's trajectory during days 62-72 of 2005 is superposed as a dashed line on which tick-marks indicate the start of each day. In the coordinate system used here, the X-Z plane contains the direction towards the Sun and Y points from dawn to dusk. [From Cowley *et al.*, 2006.]

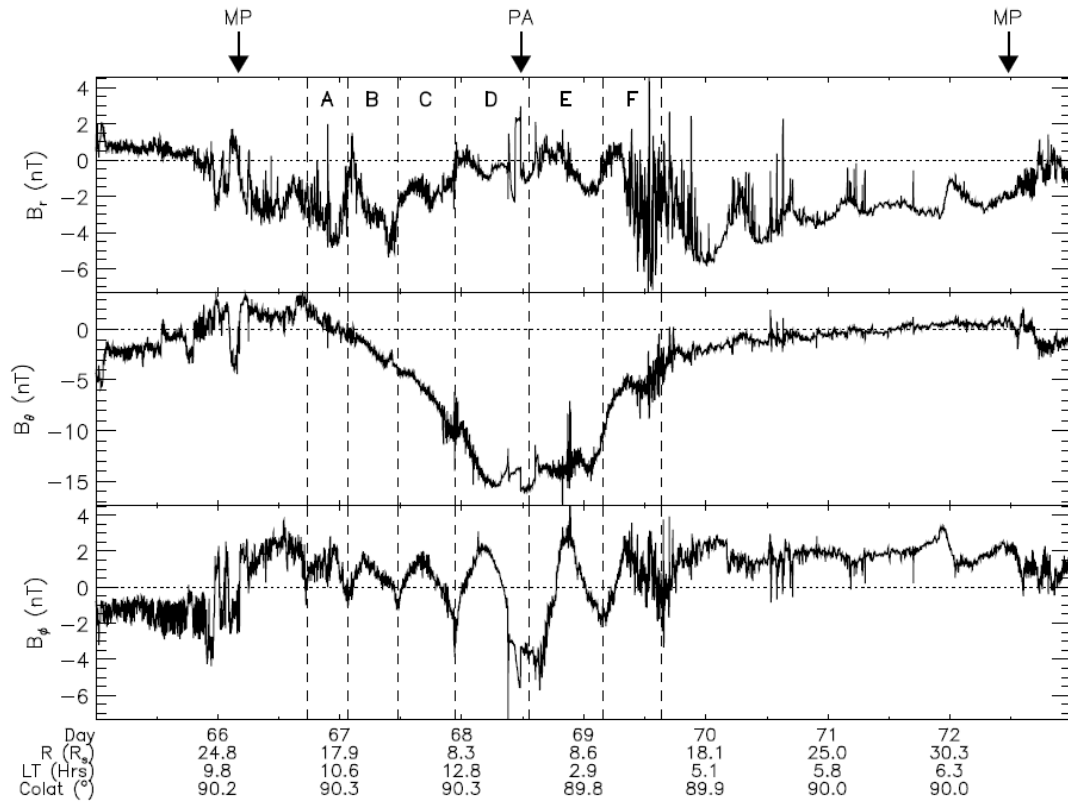


Figure 2.7 Cassini magnetic field data for days 65-72 of 2005. The three panels show the radial (r), colatitudinal (θ), and azimuthal (φ) components of the magnetic field, from which the SPV internal field has been subtracted, in spherical polar coordinates referenced to the planet's spin/magnetic axis. Inbound and outbound magnetopause crossings (MP) and periapsis (PA) are indicated at the top of the plot. Spacecraft positional data, specifically radial distance (R) from the centre of the planet, local time (LT), and colatitude (also with respect to the spin/magnetic axis) are given at the bottom of the plot. The vertical dashed lines delimit field oscillations, labelled A to F, according to minima in the φ component. [From Cowley *et al.*, 2006.]

according to minima in the φ component, are labelled A to F. In Figure 2.8 the observed periods are compared with the predictions of the spiral wave field model in a plot of wave period versus time. The horizontal line indicates the magnetospheric period (i.e. the un-Doppler-shifted period that would be observed if the spacecraft position was fixed), the dashed line shows the expected period if there is only azimuthal spacecraft motion, and the solid line takes account of both azimuthal and radial spacecraft motion. The model predicts that

- (a) near periapsis, azimuthal motion lengthens the period,
- (b) further out, radial motion dominates, shortening (blue-shifting) the period during the inbound portion of the pass and lengthening (red-shifting) it outbound,
- (c) close to periapsis the Doppler shift changes rapidly, but further out it is reasonably constant.

The observed values are seen to follow expectations in sense and magnitude.

The synodic period of the field oscillations is closely similar to that of the SKR modulations over several-year intervals, with modest relative phase drifts that lie within the envelope of scatter of the SKR phase determinations [*Andrews et al.*, 2008; *Provan et al.*, 2009a]. In the inner quasi-dipolar magnetosphere that we refer to here as the ‘core’ region, on magnetic shells with equatorial radial distances less than $\sim 15 R_S$, the oscillatory perturbation field takes the form of a quasi-uniform field (i.e. the magnitude and direction of the field in space vary only slowly with position) of a few nT amplitude lying in the equatorial plane (perpendicular to the equatorial planetary field), that rotates in the same sense as the planet [*Espinosa et al.*, 2003a,b; *Southwood and Kivelson*, 2007; *Andrews et al.*, 2010]. The SKR power is found to peak when this field points radially outward in the

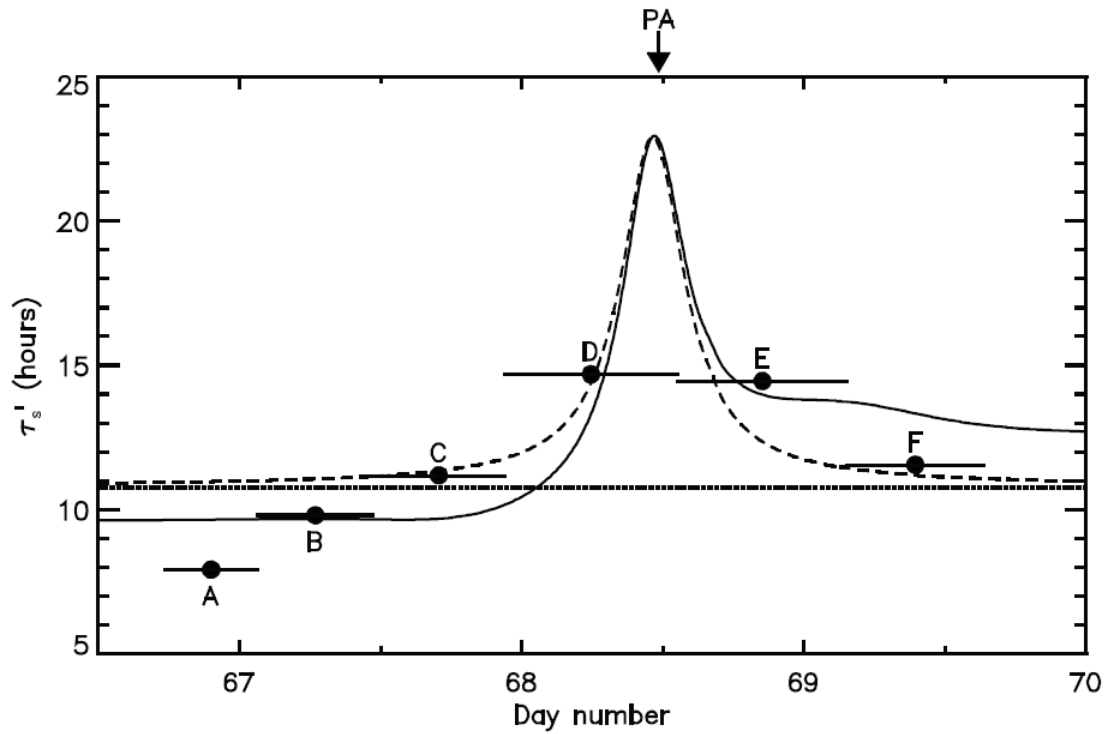


Figure 2.8 The figure shows a plot of Doppler-shifted wave period versus time in which the observed periods of oscillations A to F determined from the data shown in Figure 2.7 are compared to the predictions of the model. The horizontal line indicates the magnetospheric period (i.e. the assumed un-Doppler-shifted period), the dashed line shows the period obtained from the model when there is only azimuthal spacecraft motion, and the solid line that obtained when there is both azimuthal and radial spacecraft motion. [From Cowley *et al.*, 2006.]

post-midnight sector, at a local time (LT) of ~ 2 h [Andrews *et al.*, 2008; Provan *et al.*, 2009a]. The field perturbs the background planetary field, tilting the magnetic equator towards the direction in which the transverse field points, leading to the oscillatory tilting of the equatorial ring current/plasma sheet reported by Carbary *et al.* [2008b], which thus tilts maximally away from the Sun at SKR maxima. Oscillations of comparable amplitude in the colatitudinal component of the magnetic field (along the direction of the equatorial planetary field) are also found to be present within the ‘core’, that are in phase with the radial component of the transverse field [Andrews *et al.*, 2008; Provan *et al.*, 2009a]. Figure 2.9 shows a sketch of the near-equatorial perturbation field, the phase shown being specifically that corresponding to peak SKR power. Provan *et al.* [2009a] and Khurana *et al.* [2009] related these field variations to rotating modulations of Saturn’s ring current plasma.

Southwood and Kivelson [2007] suggested that the quasi-uniform transverse field observed in the ‘core’ region is produced by a rotating non-axisymmetric system of field-aligned currents flowing between the northern and southern ionospheres on magnetic shells with $L \sim 15$, possibly driven by seasonal differences in conductivity between the two hemispheres. Outside the region carrying the current, the magnetic perturbations will then mimic the field of a rotating transverse dipole pointing in the direction of the inner transverse field, the dipole moment concerned being that of the field-aligned current loops. Similarly, Provan *et al.* [2009a] have suggested that the overall current system associated with both the longitudinal and the transverse field oscillations is that of a rotating asymmetric ring current and its field-aligned closure currents mapping to the ionosphere. Given north-south symmetry, such a current system has no net dipole moment, and will not

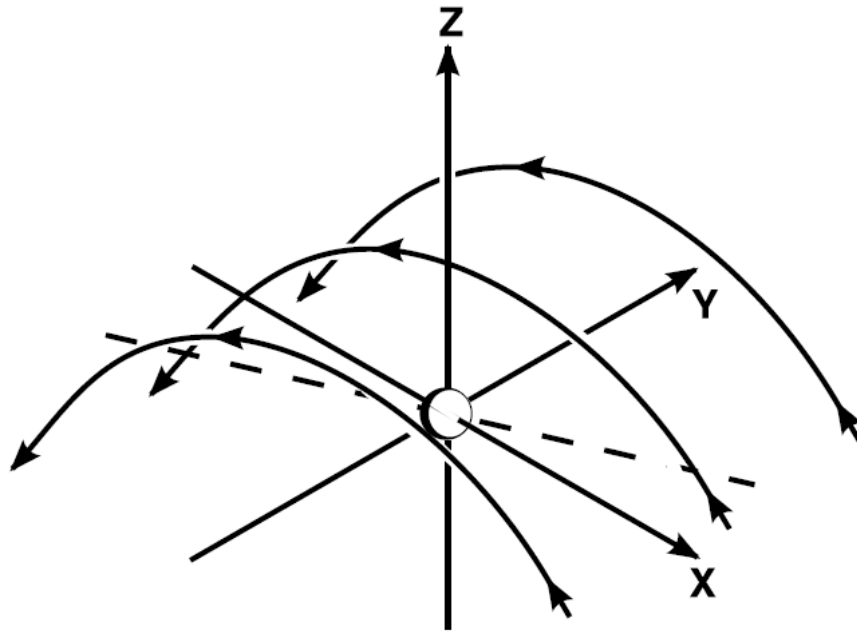


Figure 2.9 Sketch of the field lines of the near-equatorial magnetic perturbations, where the Z-axis points along the planet's spin axis, the X-Z plane contains the Sun, and Y points towards dusk. The field configuration rotates around the spin axis at the magnetospheric period, the phase shown here being specifically that corresponding to peak SKR power, when the field points radially outward at a local time of ~ 2 h as indicated by the dashed line. [From *Andrews et al.*, 2008.]

produce a quasi-uniform transverse field in the equatorial magnetosphere. However, seasonal hemispheric differences in the field-aligned currents produce effects which are exactly equivalent to the *Southwood and Kivelson* [2007] current system, including a rotating quasi-uniform field inside the current system and a net ‘dipole’ moment whose field effects will dominate at large distances. (It should be noted at this point that recent developments, to be discussed in Chapter 8, have somewhat modified this picture.) Oscillating field and plasma phenomena have been observed by Cassini in the nightside tail to distances of $\sim 60 R_S$ [e.g. *Carbary et al.*, 2007d; *Burch et al.*, 2008; *Khurana et al.*, 2009], including oscillations of the plasma sheet, that are similar in form to those produced by a tilted dipole. Hubble Space Telescope imaging of Saturn’s southern auroral oval, which maps magnetically to the outer region of the magnetosphere [*Bunce et al.*, 2008b; *Talboys et al.*, 2009], has also shown that it oscillates in position at the magnetospheric period with an amplitude of $\sim 1^\circ$ of colatitude [*Nichols et al.*, 2008]. The sense of the oscillation has been established to be consistent with expectations based on the rotating current system described above [*Provan et al.*, 2009b].

In the outermost regions of the magnetosphere, periodic modulation is also seen in the position of the magnetopause. *Espinosa and Dougherty* [2001] and *Espinosa et al.* [2003a] presented the first evidence for such oscillations from Pioneer-11 field data. During the outbound portion of the flyby the magnetopause was found to be modulated in phase with the radial component of the perturbation magnetic field, as shown in Figure 2.10. The upper panel shows the radial component of the magnetic field from which the SPV internal field has been subtracted, with a fitted sinusoid. The lower panel shows the colatitudinal component (from which the internal field has not been subtracted) in which magnetopause

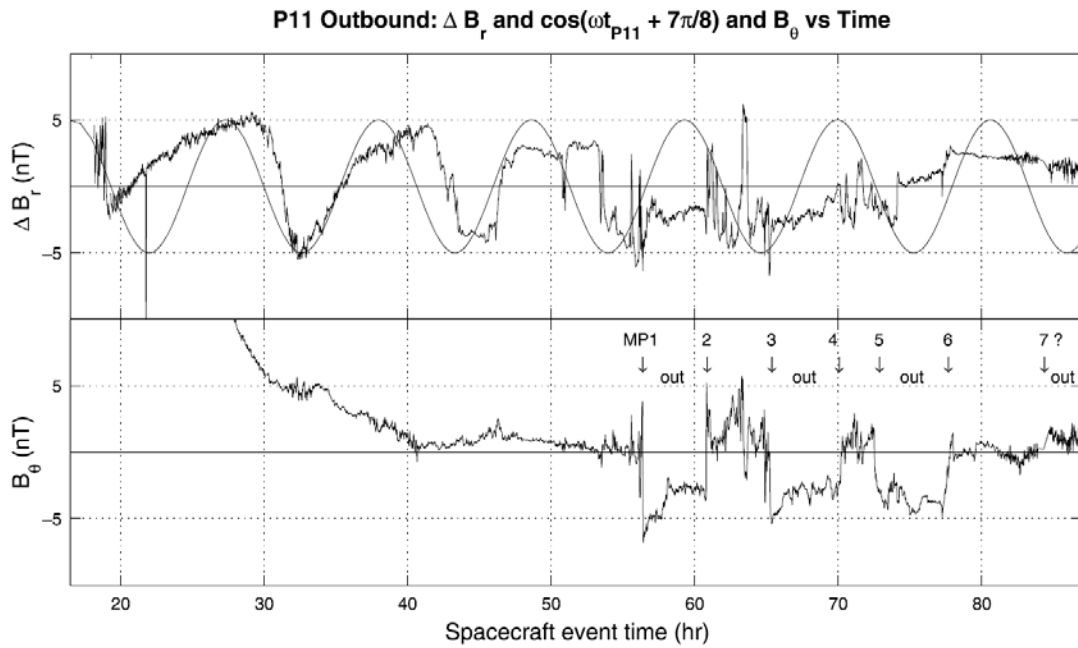


Figure 2.10 Magnetic field data from the outbound pass of the Pioneer-11 flyby. The upper panel shows the radial component of the perturbation magnetic field, and a fitted sinusoid. The lower panel shows the colatitudinal component, from which the internal field has not been subtracted, with magnetopause crossings numbered and marked by vertical arrows. [From *Espinosa et al.*, 2003a.]

crossings, numbered and marked by vertical arrows, can be clearly identified from the sharp changes between positive and negative values. Transitions from the magnetosphere to the magnetosheath (crossings 1 and 3) can be seen to occur when ΔB_r , as predicted by the sinusoid fit is negative, and from the magnetosheath to the magnetosphere (crossings 2 and 4) when ΔB_r is positive. *Espinosa and Dougherty* [2001] and *Espinosa et al.* [2003a] suggested that variations in the total pressure (combined magnetic and plasma pressure) periodically pushed the magnetopause outwards. In Chapter 4, in a study using both magnetic and electron plasma data from the Cassini orbiter, we are able to confirm that this is, indeed, the case. In Chapter 6 we show that within a broad timing window centred on the magnetospheric period, magnetopause motions are highly organized by the phase of the magnetic oscillations in the ‘core’ magnetosphere. We also demonstrate a relationship between the phase of maximum outward magnetopause boundary displacement and that of the rotating plasma ‘bulge’ in the outer magnetosphere recently reported by *Burch et al.* [2009] and the density maximum in the inner Enceladus plasma torus observed by *Gurnett et al.* [2007]. As the magnetopause represents the effective obstacle around which the solar wind flows, oscillatory motion of the magnetopause should produce corresponding modulation of the bow shock position, and in Chapter 7 we present the first clear evidence of magnetospheric period oscillations of the bow shock.

Chapter 3

Instrumentation

3.1 Introduction

The studies presented in Chapters 4, 6, and 7 of this thesis use data from the fluxgate magnetometer (FGM) and electron spectrometer (ELS) sensors of the Cassini orbiter. The data are mainly used for the identification and timing of magnetopause and bow shock boundary crossings, but in Chapter 4 they are also used to calculate magnetic and plasma pressures. The characteristics of the magnetic field and the plasma change markedly across both boundaries. We employ electron rather than ion data because the thermal velocities of the electrons are much larger than the bulk flow speeds of the plasma, so that under usual conditions the electron fluxes will not depend greatly on look direction and the variations in electron properties across the boundaries can be observed essentially independent of spacecraft or instrument pointing. The thermal velocities and bulk velocities of the ions are comparable and the main ion population will only be seen if the detector happens to be pointing into the flow. In the present chapter we provide an overview of Cassini and its orbital tour, and describe the most pertinent features of the FGM and ELS sensors. Detailed descriptions of the FGM and ELS can be found in *Dougherty et al.* [2004] and *Young et al.* [2004], respectively.

3.2 The Cassini Orbiter

The Cassini-Huygens mission is a joint project between the American (NASA), European (ESA), and Italian (ASI) space agencies to explore the entire saturnian system.

Cassini-Huygens is the largest and most complex interplanetary spacecraft ever built, measuring 6.7 m high and 4 m wide (see Figure 3.1), and carrying 12 suites of science instruments on the orbiter and 6 on the Huygens probe. Figure 3.2 shows a diagram of Cassini (with the Huygens probe still attached) on which science instruments and some of the engineering subsystems are labelled. The spacecraft is three-axis stabilized (rather than spin stabilized), its attitude being maintained by thrusters and reaction wheels, and the instruments are body-fixed, though some are capable of articulation. This arrangement was adopted for budgetary reasons but has the disadvantage of restricting the three-dimensional view of individual sensors, such that it is usually necessary to turn the whole spacecraft to point an instrument.

Cassini-Huygens began its seven year journey to Saturn in October 1997. Gravity assist flybys of Venus (in April 1998 and June 1999), Earth (August 1999), and Jupiter (December 2000) gave the spacecraft the energy needed to reach Saturn, and also provided opportunities to test (and in the case of Earth flyby, calibrate) instruments and obtain new scientific data. The spacecraft arrived at Saturn in July 2004 and began an orbital tour that was originally intended to last four years but which has since been extended to 2017. The Huygens probe was released in December 2004 and successfully landed on Titan in January 2005. Cassini's tour began with the Saturn Orbit Insertion (SOI) pass in July 2004, followed by three orbits or 'Revs' (revolutions) denoted A, B, and C. Subsequent orbits are numbered Revs 3, 4, 5 and so on, the Rev number changing at apoapsis. In Chapter 4 we consider only the first ~20 orbits, while in Chapters 6 and 7 we use all suitable orbits from SOI to the inbound pass of Rev 55 in late December 2007. During this time Cassini's trajectory is continually evolving: the earliest orbits have apoapses in the dawn to noon sector, apoapsis then rotates into the magnetotail during which interval no magnetopause or



Figure 3.1 The Huygens probe (gold dome) being mounted onto the Cassini orbiter.

[Courtesy NASA/JPL.]

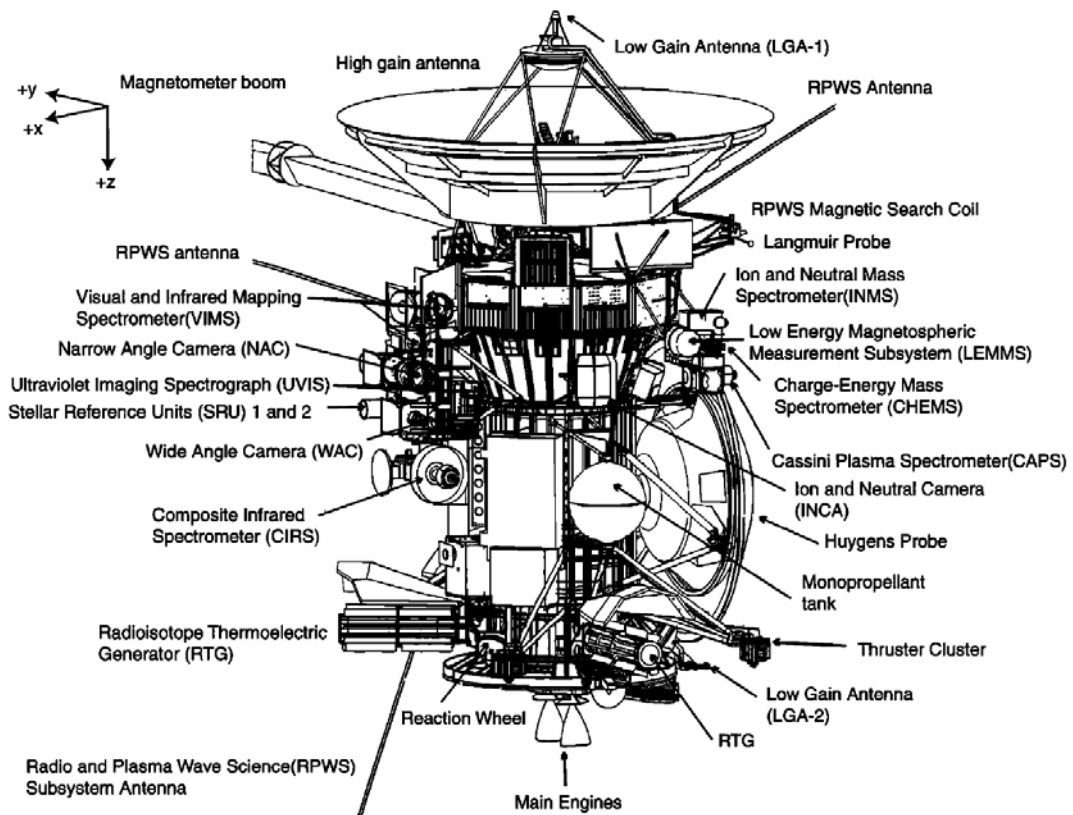


Figure 3.2 A diagram of Cassini, with the Huygens probe still attached, showing the science instruments and some of the engineering subsystems. [From *Burton et al.*, 2001.]

bow shock crossings take place, and for later orbits apoapsis occurs in the noon to post-noon sector. The orbital tour is discussed further in Chapter 6.

3.3 The Cassini Fluxgate Magnetometer

Cassini's dual technique magnetometer (MAG) consists of a fluxgate magnetometer (FGM) and a vector helium magnetometer that can also operate in scalar mode (V/SHM). Magnetometers are sensitive to electric currents and ferrous materials so to isolate these instruments from the stray magnetic field of the spacecraft the FGM is situated midway along an 11 m non-metallic boom and the V/SHM at the end of the boom (see Figure 3.3). The dual technique approach has a number of advantages. Placing two magnetometers at different distances along the boom assists in the characterization of the spacecraft-generated field and its separation from the external field. The instruments can be cross-calibrated, and the extremely wide dynamic range of the FGM is complemented by the lower noise of the V/SHM. Most importantly the inclusion of two magnetometers provides the redundancy essential in missions of long duration. If one instrument fails, as the V/SHM did in November 2005 (having performed well during the journey to Saturn and the early orbits), the majority of the science objectives can still be met using the remaining instrument.

The FGM measures the strength and direction of the ambient magnetic field using a mutually perpendicular arrangement of three single-axis sensors, each of which produces a voltage proportional to the component of the magnetic field along its axis. The sensors are mounted on a ceramic block, the low thermal expansion coefficient of which minimizes changes in alignment between the sensors due to temperature variations. The normal

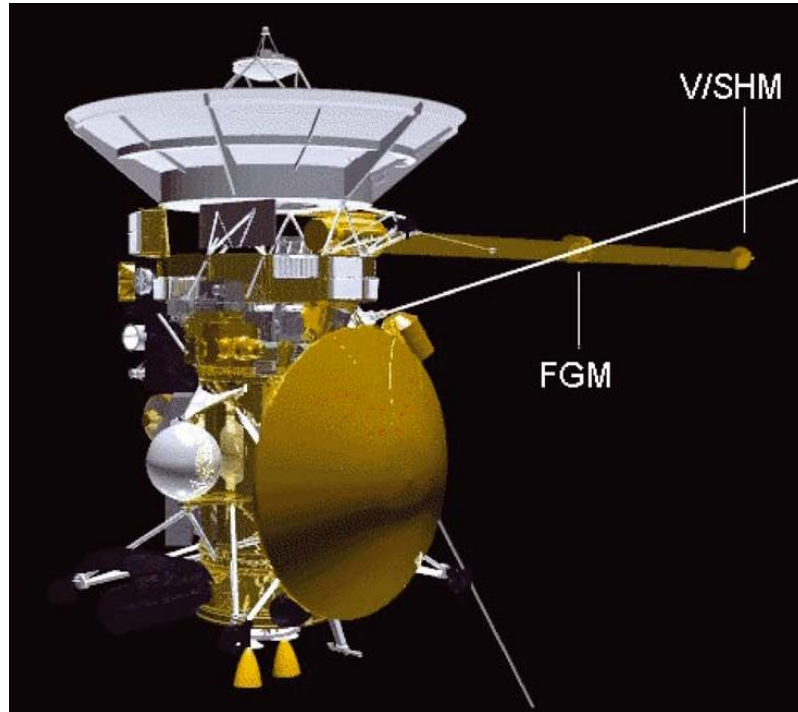


Figure 3.3 The figure shows the placement of the FGM and V/SHM magnetometers on the boom. [From *Dougherty et al.*, 2004.]

sampling rate is 32 vectors s^{-1} , but in Chapters 4, 6, and 7 we use data averaged to 1 min resolution.

Figure 3.4 shows a schematic diagram of a single-axis sensor in which H_{ext} represents the component of the external magnetic field along the sensor's axis of sensitivity. A ring core made of a highly magnetically permeable (high μ) alloy is wrapped in a drive coil and completely enclosed in a sense winding. (The Cassini FGM operates in closed loop and has a third, feedback, winding.) For simplicity it is helpful to think of the ring core as two separate half cores, shown in blue and green in the figure. A square wave is driven through the coil, generating a magnetic field that sends the half cores into saturation twice per cycle. (During saturation, the magnetic axes of all the atoms in the half core are lined up in the same direction.) Each half core goes through the same cycle (magnetized – unmagnetized – inversely magnetized – unmagnetized – magnetized etc.) but the two half cores differ in phase by 180° , so that while one is magnetized in one direction the other is magnetized in the opposite direction. When $H_{\text{ext}} = 0$ the half cores generate fields that, at any stage of the cycle, have the same strengths but opposite orientations and hence exactly cancel. In the presence of an external field with a non-zero component along the axis of sensitivity, the half core that is (at that stage of the cycle) generating a field in the opposite direction to H_{ext} comes out of saturation sooner (its field being weakened by the external field), while the half core that is generating a field in the same direction as H_{ext} comes out of saturation later (its field being reinforced by the external field). The fields no longer exactly cancel out and the changing flux within the coil induces a voltage in the sense winding with a frequency twice that of the drive frequency and an amplitude proportional to the strength of the external field in the direction of the axis of sensitivity.

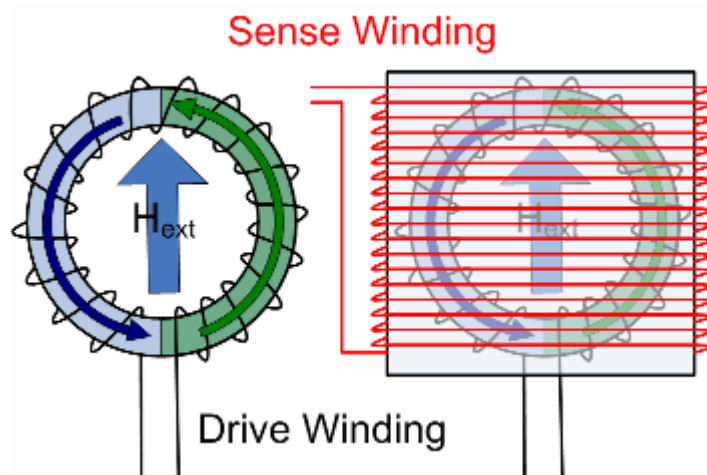


Figure 3.4 A schematic diagram of a single-axis fluxgate sensor. The drive coil is shown in black and the sense winding in red. H_{ext} represents the component of the external field along the sensor's axis of sensitivity. [Courtesy Imperial College London.]

The FGM must maintain high accuracy and resolution over a very wide dynamic range, from less than 1 nT in the solar wind of the outer solar system to several thousand nT at closest approach to Saturn (and in Earth flyby). The instrument has four ranges and switches between them automatically. The ranges, with resolutions in parentheses, are as follows: ± 40 nT (4.9 pT), ± 400 nT (48.8 pT), ± 10000 nT (1.2 nT), and ± 44000 nT (5.4 nT).

3.4 The Cassini Electron Spectrometer

The Cassini Plasma Spectrometer (CAPS) is made up of three sensors: the ion mass spectrometer (IMS), the ion beam spectrometer (IBS), and the electron spectrometer (ELS). Figure 3.5 shows a schematic of Cassini with the fields of view of these instruments and the spacecraft coordinates indicated. Note that the size of the instruments has been greatly exaggerated for clarity (compare with Figure 3.2). The IMS and IBS measure the flux of positively charged atomic and molecular ions as a function of energy per charge, and additionally in the case of the IMS as a function of mass per charge (thereby allowing different species to be distinguished), and angle of arrival at the instrument. The ELS measures the flux of electrons as a function of energy per charge and angle of arrival. Because Cassini is three-axis stabilized, and the view around the spacecraft consequently restricted, CAPS is mounted on a motor-driven platform called an actuator which can sweep the whole suite of sensors in azimuth in the spacecraft $X-Y$ plane through a maximum angle of $\pm 104^\circ$.

Figure 3.6 shows a sketch of the key sensor elements of CAPS, with the ELS at the top of the figure. The ELS is a standard hemispherical top-hat analyzer. Electrons enter the instrument via a baffled collimator, emerging into the narrow gap between a pair of

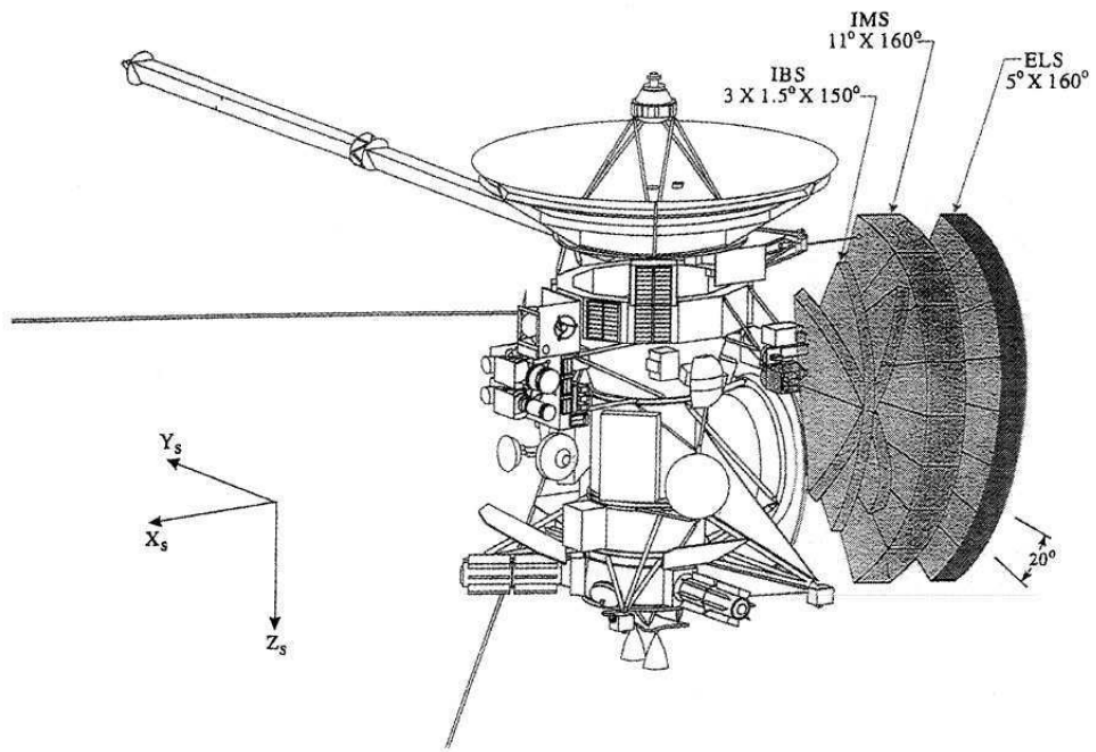


Figure 3.5 The figure shows the fields of view of the three Cassini Plasma Spectrometer (CAPS) sensors and the spacecraft coordinates. For clarity, the size of the sensors is greatly exaggerated. [From Rymer *et al.*, 2001.]

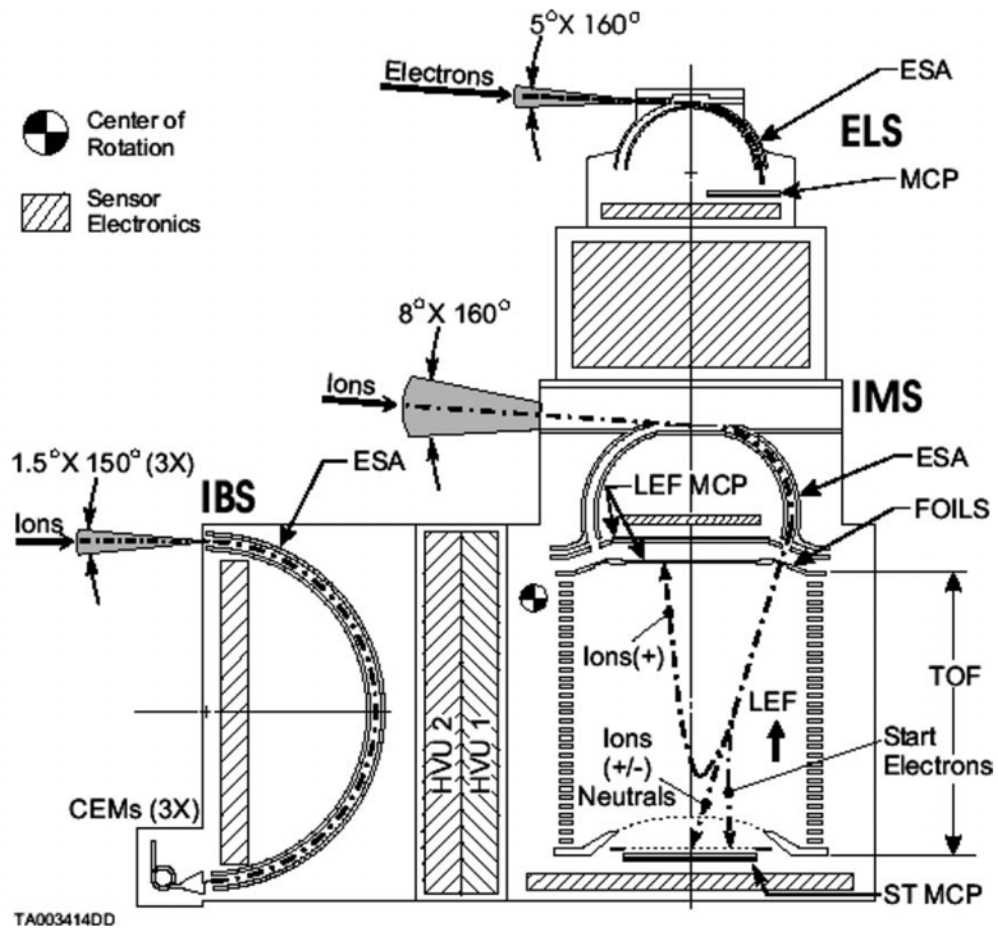


Figure 3.6 Sketch of the key sensor elements of CAPS. Heavy dashed lines indicate the general shape of particle trajectories. [From *Young et al.*, 2004.]

concentric hemispherical electrostatic analyzer (ESA) plates. A potential difference is maintained between the two plates. Only electrons with energies within a narrow range determined by this potential will have trajectories that take them through the analyzer without hitting a wall. Varying the potential allows electrons of different energies to pass through the analyzer. On exiting the analyzer, electrons strike micro-channel plates (MCPs), generating a cascade of secondary electrons that are collected by an arc of eight $20^\circ \times 5^\circ$ anodes (which can be thought of as pixels). The full $5^\circ \times 160^\circ$ field of view is then swept in azimuth by the actuator. In normal operation the analyzer is stepped through a 64-level energy spectrum from 26 keV (bin 1) down to 0.6 eV (bin 63), the 64th level being a fly-back step changing the voltage from the lowest back to the highest energy. Sixty-three values of electron counts can be returned in two seconds for each of the eight anodes, though in this thesis we use 1 min averaged data from anode 5. Anode 5 is chosen because its field of view is not obstructed by spacecraft structures for any angle of the actuator.

In Chapters 4, 6, and 7 we present the results of studies based on data obtained by the FGM and ELS instruments.

Chapter 4

Cassini Observations of Magnetospheric Period Oscillations of Saturn's Magnetopause

4.1 Introduction

In this chapter, in a study based on examination of the first ~20 Cassini orbits, we show that magnetopause oscillations at the magnetospheric period commonly occur, in phase with plasma pressure variations inside the magnetosphere, this being a phenomenon unique to Saturn among the magnetized planets. We present case studies illustrating this behaviour, and make an estimate of the peak-to-trough amplitude of the boundary oscillations and the change in internal pressure required to produce such motions. A qualitative physical picture is proposed in which a compressive wave propagates outward through the sub-corotating outer magnetospheric plasma, originating from a near-corotating source in the nearer-planet region.

4.2 Case Studies: Cassini Revs 16 and 17

In this section we exemplify the evidence for magnetopause boundary oscillations in Cassini data by presenting three successive boundary region passes, specifically the inbound and outbound passes of Rev 16 and the inbound pass of Rev 17. We use 1 min averaged magnetic field data from the fluxgate magnetometer, together with 1 min averaged electron data from the ELS electron spectrometer.

Figure 4.1 shows data for Rev 16, covering the interval from day 281 to day 290 (8-17 October), inclusive, of 2005. The top panel is an electron count rate spectrogram over the energy range 0.6 eV to 26 keV for ELS anode 5, colour-coded according to the

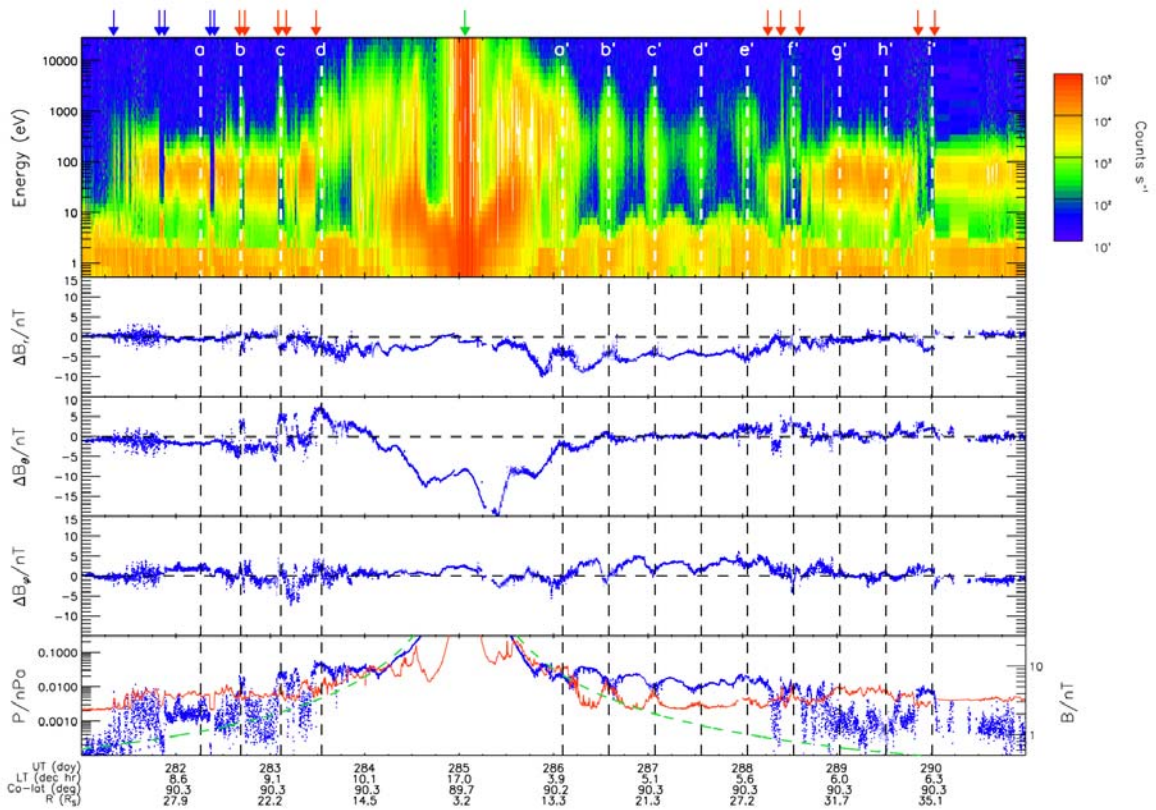


Figure 4.1 The figure shows data from Cassini Rev 16, days 281-290 of 2005. The top panel shows an electron count rate spectrogram, colour-coded according to the scale on the right-hand side. The next three panels show the spherical polar radial (r), colatitudinal (θ), and azimuthal (ϕ) components of the magnetic field referenced to the planet's spin/magnetic axis, with the 'Cassini' internal field model subtracted. In the bottom panel the blue data show the magnetic field pressure (scale on left-hand side) and field magnitude (right-hand scale). The internal field has not been subtracted, and is indicated by the green dashed line. The red data in this panel show the electron pressure, from which the contribution of spacecraft photoelectrons has been eliminated. Arrows at the top of the figure mark principal bow shock (blue) and magnetopause (red) crossings and periapsis (green). Spacecraft positional information is provided at the bottom of the plot.

scale on the right-hand side. Note that at radial distances beyond $\sim 10 R_S$ the intense fluxes below a few eV are spacecraft photoelectrons. The next three panels show the spherical polar radial (r), colatitudinal (θ), and azimuthal (φ) components of the magnetic field with respect to the planet's spin/magnetic axis, with the 'Cassini' internal field model subtracted [Dougherty *et al.*, 2005]. In the bottom panel the blue data show the magnetic field pressure on a logarithmic scale. The internal field has not been subtracted in this case, and is indicated by the green dashed line. Field magnitudes may be read from the scale on the right-hand side. The red line in this panel shows the electron pressure derived from the ELS distributions corrected for spacecraft potential, thus eliminating the photoelectron contribution. Ion pressures are not routinely available for this interval, but in the middle and outer magnetosphere are found typically to be higher than electron pressures by factors of 2-3 [M.F. Thomsen, personal communication, 2006]. At the top of the figure principal bow shock and magnetopause crossings are indicated by the blue and red arrows, respectively, while the green arrow indicates periapsis. At the bottom of the figure we provide spacecraft positional information, specifically local time, colatitude (again with respect to the spin/magnetic axis), and radial distance from the centre of the planet. It can be seen that Cassini was located very close to Saturn's equatorial plane throughout the interval (colatitude $\sim 90^\circ$).

The orbit is also depicted in Figure 4.2, projected onto Saturn's equatorial (X - Y) plane with the Sun to the left. The Z -axis is thus directed along the spin/magnetic axis, the X - Z plane contains the Sun, and Y points towards dusk, completing the orthogonal right-handed triad. The plot covers an interval from one day before to one day after that shown in Figure 4.1, with the dots on the trajectory marking the start of the days numbered. At the

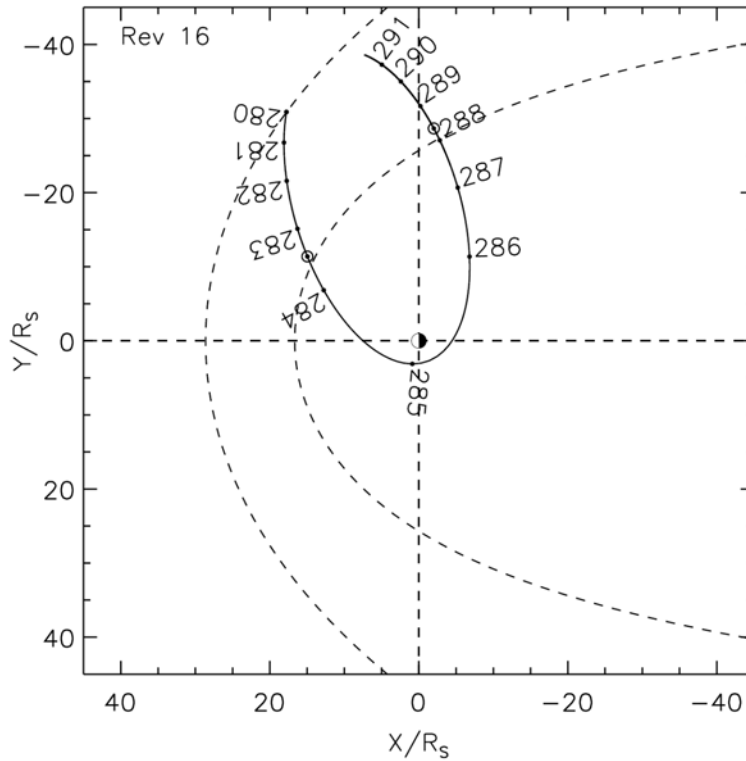


Figure 4.2 Orbit plot for Cassini Rev 16, days 280-291 of 2005, projected onto Saturn's equatorial (X - Y) plane with the Sun to the left. Simple dots on the trajectory mark the start of the days numbered, while circled dots indicate the locations of the last inbound and the first outbound magnetopause crossings observed. The dashed lines show *Arridge et al.* [2006] model magnetopauses, the outer one corresponding to a solar wind dynamic pressure of 0.01 nPa, and the inner one to 0.1 nPa, these spanning the usual range at Saturn.

start of day 281 the spacecraft was inbound in the mid-morning sector at an initial radial distance of $\sim 32.3 R_S$. It underwent periapsis passage at $\sim 3.0 R_S$ near the beginning of day 285, and then passed outbound through the magnetosphere in the dawn sector, reaching a radial distance of $\sim 37.6 R_S$ at the end of day 290. The dashed lines in Figure 4.2 are *Arridge et al.* [2006] model magnetopauses, the outer one corresponding to a solar wind dynamic pressure of 0.01 nPa, the inner one to 0.1 nPa, spanning the usual range of values at Saturn. The circled dots on the trajectory mark the locations of the last inbound and the first outbound magnetopause crossings observed, thus indicating a relatively high solar wind dynamic pressure during the orbit and a relatively compressed magnetosphere.

We focus first on the outbound pass of Rev 16, starting on day 286. Examining the magnetic field data, we see a sequence of four oscillations in field strength and direction on days 286 and 287 (labelled a' to d'), of the form reported previously by *Espinosa et al.* [2003a] and *Cowley et al.* [2006] and discussed in Chapter 2. These oscillations principally involve the radial and azimuthal components, with the colatitudinal component remaining close to zero after the middle of day 286. Looking at the electron spectrogram, we find corresponding oscillations in the electron data over essentially the full range of energies sampled, with maxima in the flux occurring at approximately the same time as minima in the field strength, such that the field and electron pressures vary in anti-phase. In the first three of these flux maxima the electron pressure reached values comparable with the field pressure, which, with the ion pressure added, indicates that $\beta \geq 1$ conditions occurred at these times (β being the ratio of the total plasma pressure to the magnetic pressure). We note that the magnetic field was strongly disturbed during these intervals, characteristic of $\beta \geq 1$, while in the regions between where the electron pressures were much smaller than

the field pressures, the field was more smoothly varying, characteristic of low β conditions. Using the combined field and plasma data we are able to determine the period of the oscillations, and find an essentially constant period of ~ 11.75 h, as indicated by the vertical dashed lines which approximately mark electron flux maxima and field strength minima. This period is significantly longer than the magnetospheric period of ~ 10.80 h [Kurth *et al.*, 2008; Provan *et al.*, 2009a], due principally to the Doppler shift resulting from the spacecraft's radial motion through the wave field [Cowley *et al.*, 2006].

If we project the 11.75 h sequence forward into day 288, we see that it correctly predicts the timings of two further maxima in the electron flux, labelled e' and f' . The first of these is characterized by a different magnetic signature than hitherto, in which a small increase in the field strength took place in phase with the increase in electron pressure. The electron pressure increased from ~ 0.0025 to ~ 0.0045 nPa at the maximum (potentially indicative of a total plasma pressure increase from ~ 0.01 to ~ 0.015 nPa if the ion pressure is ~ 2 - 3 times the electron pressure as indicated above), while the magnetic pressure increased from ~ 0.015 to ~ 0.02 nPa. With reasonable allowance for the ion pressure, therefore, we estimate an increase in total pressure from ~ 0.025 to ~ 0.035 nPa in the oscillation. Similar electron pressures were also reached in the second flux maximum f' . Between these maxima, however, a brief magnetosheath encounter took place, evidenced by the intense fluxes of low-energy (~ 10 - 100 eV) electrons, and corresponding changes in the field strength and orientation. That is to say, the magnetopause moved inward across the spacecraft during the low-pressure phase of the oscillation, and then out again as the internal pressure rose once more. These magnetopause crossings occurred at radial distances of ~ 28.8 (into the magnetosheath) and $\sim 29.2 R_S$ (back into the magnetosphere),

and are marked by red arrows at the top of the plot. Such observations provide primary evidence for modulation of the magnetopause boundary by internal pressure variations at the magnetospheric period. Extrapolating the sequence into days 289 and 290 with lines marked g' , h' and i' , we find that while no magnetospheric entries occurred around the times of g' and h' , a transient encounter did take place at i' near the start of day 290 at a radial distance of $\sim 35 R_S$. We infer that this encounter was associated with a fall in solar wind dynamic pressure that brought the oscillating boundary once more within range of the spacecraft (see section 4.3), allowing a transient entry around the time of the internal pressure peak.

We now examine the data from the inbound pass. As mentioned above, the magnetosphere was relatively compressed during Rev 16, such that the spacecraft spent only a short interval inside the magnetosphere prior to periapsis. In this case there is no opportunity to observe a long sequence of variations at around the magnetospheric period. However we note two transient magnetosphere encounters labelled b and c with midpoints at radial distances of ~ 24.1 and $\sim 21.4 R_S$, respectively, which are separated by ~ 10.25 h and are followed by a final magnetopause crossing ~ 8.5 h later (red arrows). We infer that these are the result of boundary oscillations similar to those observed outbound. The ~ 10.25 h period is shorter than the magnetospheric period, however, due to the Doppler shift associated with the spacecraft's radial inward motion. Projecting the 10.25 h sequence forward in time, we find that d corresponds to a local maximum in the magnetospheric magnetic and electron pressures. Projecting the sequence backward to earlier times, there is no magnetosphere encounter at a , but we note a brief excursion into the solar wind between a and b , indicated by the interval of low electron flux above ~ 10 eV and the simultaneous low magnetic field strengths (the bow shock crossings are indicated by blue

arrows). This may indicate that the bow shock is also modulated, moving closer to the planet in the low-pressure phase of the oscillation. An earlier transient solar wind encounter late on day 281 does not obey this phasing sequence, however, at least with the period as determined here, perhaps because of additional boundary motion due to changes in solar wind pressure.

Figure 4.3 shows data for the Rev 17 inbound pass in the same format as Figure 4.1, for days 298-302 (25-29 Oct) inclusive. The orbit is very similar to Rev 16 and is not shown here. The magnetosphere is now more expanded due to lower solar wind dynamic pressure (see section 4.3), such that we again observe a series of electron flux maxima inside the magnetosphere, associated with modest increases in electron pressure, of order ~ 0.001 nPa. The period of ~ 10.25 h is the same as that used (on a less well-constrained basis) for Rev 16 inbound. The main feature of note is the transient magnetosheath entry occupying the low flux region between b and c (at $\sim 29.5 R_S$), again indicating boundary modulation with the magnetospheric period oscillation. Looking to earlier times, no magnetopause encounters are seen near a , suggesting that the spacecraft was then beyond the range of the oscillating boundary.

4.3 The Amplitude of the Boundary Oscillations

We now consider the implications of the above observations for the amplitude of the boundary oscillations, and for the changes in internal pressure required to produce them. An initial estimate of the amplitude can be obtained by examining the radial range of observed boundary locations on a given pass, this having the nature of a lower limit to the peak-to-trough amplitude assuming an approximately steady solar wind dynamic pressure. To provide a consistent pass-to-pass estimate we have mapped the observed boundary

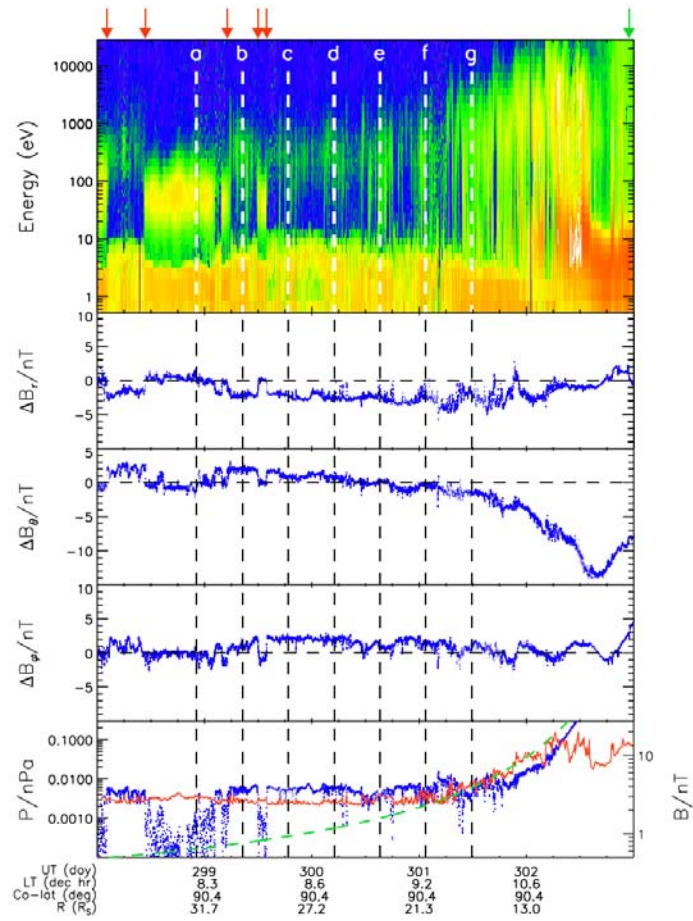


Figure 4.3 The figure shows data from Cassini Rev 17 inbound, days 298-302 of 2005, in the same format as Figure 4.1.

locations to the planet-Sun line using the magnetopause shape given by the model of *Arridge et al.* [2006], this procedure assuming for simplicity that the variation in oscillation amplitude with local time around the boundary is in rough proportion to the mean boundary distance. Since the *Arridge et al.* [2006] model is parameterized in terms of the solar wind dynamic pressure D_p , we also consider the value of this quantity appropriate to the above intervals, validating and quantifying the inferences made in section 4.2. In this model the radial distance of the magnetopause boundary, R_{MP} , is given by

$$R_{MP}(\theta) = R_{MP_{SS}} \left(\frac{2}{1 + \cos \theta} \right)^\kappa, \quad (4.1)$$

where $R_{MP_{SS}}$ is the subsolar magnetopause radius, and θ is the angle to the planet-Sun line. Fits to Cassini boundary observations then show that $R_{MP_{SS}} \approx 9.7 D_p^{-0.24} R_S$ and $\kappa \approx 0.77 - 1.46 D_p$, where D_p is in nPa. If we consider the inbound pass of Rev 16, for example, the mean position of the last three magnetopause crossings on day 283 (at $R_{MP} \approx 21.5 R_S$ and $\theta \approx 45^\circ$) indicate a dynamic pressure of ~ 0.05 nPa according to equation (4.1), with a subsolar radius of $\sim 19 R_S$, i.e. a relatively compressed magnetosphere as indicated in section 4.2. A check can also be made by considering the pressure observed inside the magnetopause boundary, P_M , related to D_p by $P_M \approx k D_p \cos^2 \Psi$, where $k \approx 0.88$ for a high-Mach number flow [*Spreiter and Alksne*, 1970] and Ψ is the angle between the solar wind flow and the boundary normal. Using the *Arridge et al.* [2006] model to estimate Ψ ($\sim 25^\circ$ in the present case) then yields the estimate $P_M \approx 0.04$ nPa, which can be seen to be in good agreement with the generally dominant magnetospheric magnetic pressures (corresponding to field strengths $\sim 9-11$ nT) observed inside the inbound

magnetopause in Figure 4.1. The main point here, however, is that if we use the model boundary shape to map the observed boundary radii to the planet-Sun line, the range of subsolar magnetopause distances implied by the observed boundary positions lies between ~ 17.1 and $\sim 21.3 R_S$, such that the subsolar peak-to-trough oscillation amplitude is at least $\sim 4.2 R_S$. Repeating this analysis for the first three crossings on the outbound pass yields a similarly high dynamic pressure of ~ 0.07 nPa with a subsolar magnetopause radius of $\sim 18 R_S$, consistent (for $\Psi \approx 60^\circ$) with magnetospheric pressures of ~ 0.02 nPa (field strengths $\sim 6-7$ nT) observed inside the boundary in Figure 4.1. The range of magnetopause distances mapped to the subsolar point then varies between ~ 17.3 and $\sim 18.5 R_S$, corresponding to a peak-to-trough oscillation amplitude of at least $\sim 1.2 R_S$. However, the final outbound magnetopause crossings on Rev 16 at the end of day 289 indicate a lower dynamic pressure of ~ 0.03 nPa with a more expanded subsolar magnetopause at $\sim 22 R_S$, consistent (for $\Psi \approx 50^\circ$) with magnetospheric pressures of ~ 0.01 nPa (field strengths $\sim 4-5$ nT) observed inside the boundary. These crossings are therefore not taken to form part of the initial outbound boundary oscillation sequence as previously outlined in section 4.2. Finally, the last three magnetopause encounters on the Rev 17 inbound pass indicate an even lower dynamic pressure of ~ 0.015 nPa with a subsolar magnetopause at $\sim 25 R_S$, consistent (for $\Psi \approx 35^\circ$) with magnetospheric pressures of ~ 0.01 nPa observed inside the boundary (Figure 4.3). The range of magnetopause distances mapped to the subsolar point then varies between ~ 24.4 and $\sim 25.4 R_S$, indicating a peak-to-trough oscillation amplitude of at least $\sim 1.0 R_S$.

Although the above estimates individually are subject to uncertainty due both to their nature as lower limits and to the possibility of boundary motion due to changing solar wind dynamic pressure during a particular pass, they collectively suggest a peak-to-trough

boundary oscillation amplitude of a few Saturn radii. Another indication may be obtained from the frequency with which such multiple crossings are observed in the Cassini data, the results already discussed suggesting that they are not rare. We will consider this topic in greater depth in Chapter 6, but initial investigation suggests that multiple boundary crossings (typically three) separated by intervals near the magnetospheric period occur in roughly half of all well-observed boundary-region passes. For sinusoidal boundary oscillation, an observer moving uniformly across the boundary region has almost equal probability of experiencing either one or three boundary crossings, depending on the relative phasing of the oscillation, if they spend one full oscillation period crossing the region. Our initial results thus suggest that the time typically spent by the spacecraft within the region of oscillations is roughly one magnetospheric period of ~ 10.80 h. Since the speed of the spacecraft in the boundary region normal to the *Arridge et al.* [2006] model magnetopause is typically $\sim 3.5 \text{ km s}^{-1}$, the implied width of the region (i.e. the peak-to-trough amplitude) is $\sim 2.3 R_S$ at the spacecraft location, or $\sim 2 R_S$ on the planet-Sun line, consistent with the above individual estimates. We thus estimate that the peak-to-trough oscillation amplitude is typically $\sim 10\%$ of the mean radial distance of the boundary. If the typical amplitude is significantly smaller than this then multiple boundary crossings at the magnetospheric period would not be observed at all, while if the amplitude is much larger, then larger numbers of multiple crossings would be the norm, neither of which is the case. We will return to these issues in Chapter 5 in which we develop a simple theoretical model of an oscillating planar boundary, and in Chapter 6 in which we apply the theory to a data set derived from ~ 40 Cassini orbits.

4.4 The Physical Origins of the Boundary Oscillations

In line with the discussions of *Espinosa et al.* [2003b] and *Cowley et al.* [2006], we suppose that a compressive wave propagates outward into Saturn's magnetosphere from some near-corotating source near the planet, leading to field and plasma oscillations at the magnetospheric period at any fixed position within the system. This is illustrated in Figure 4.4, where we sketch the system in the equatorial plane at intervals of one quarter of the magnetospheric period. In these diagrams the long-dashed lines represent surfaces of constant plasma pressure, falling with distance from the planet, while the dotted lines show the phase fronts of the wave corresponding to the peaks and troughs of the pressure, which form a spiral pattern due to the outward propagation of the wave combined with the corotation of the source. As the pressure 'fronts' sweep through the sub-corotating plasma in the outer magnetosphere, the magnetopause shown by the outer solid line is displaced outward and inward at the magnetospheric period, as observed. For comparison, the averaged position of the magnetopause is shown by the short-dashed line. Although not shown explicitly, the changing shape of the magnetospheric obstacle will also inevitably lead to magnetospheric period oscillations in the bow shock position. Only modest evidence for this effect has been found in the data presented, but in Chapter 7 we show that bow shock oscillations at the magnetospheric period do commonly occur.

We finally make a simple estimate of the magnitude of the internal pressure perturbations required to displace the boundary through typical peak-to-trough amplitudes of $\sim 10\%$ of the mean position. We first note that for oscillations on the time scale of the magnetospheric period, the boundary position will always be determined by near-equilibrium between the solar wind dynamic pressure and the local pressure inside the boundary. If the boundary were to be displaced from its equilibrium position, the

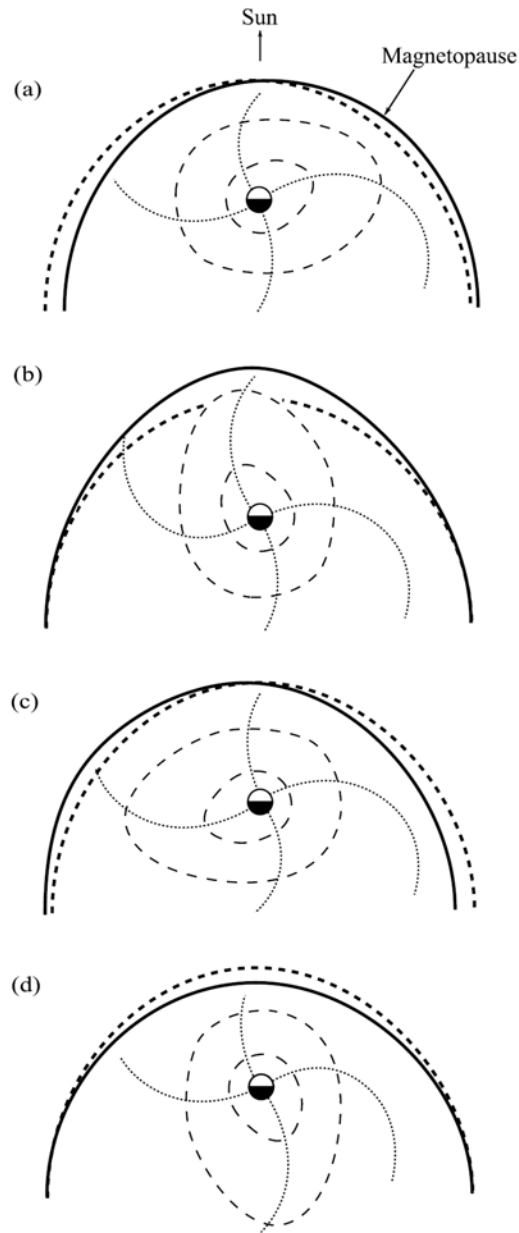


Figure 4.4 Sketch of Saturn's magnetosphere in a cut through the equatorial plane, shown at intervals of one quarter of the magnetospheric period. The long-dashed lines indicate surfaces of constant plasma pressure, the dotted lines the phase fronts of the wave which correspond to peaks and troughs of the pressure, the solid line the instantaneous magnetopause position, and the short-dashed line its average position.

exponential time scale required to move back to equilibrium is $\sim R_{MP}/3V_{SW}$ (this expression is derived in the Appendix), where V_{SW} is the solar wind speed, which is of order ~ 15 min at Saturn, much less than the magnetospheric period. Correspondingly, for the amplitudes indicated, the speed of the boundary motion is of order $\sim 10 \text{ km s}^{-1}$, which is thus negligible compared with the speed of the solar wind. The boundary pressure balance equilibrium condition is taken to be

$$P_{SW} \approx \frac{2(1+\beta)B_{eq}^2}{\mu_o} \left(\frac{R_S}{R_{MP}} \right)^\gamma + \Delta P_w(t) , \quad (4.2)$$

where P_{SW} on the left side is the total pressure of the shocked solar wind outside the boundary, taken to be a constant. The first term on the right side is that of a dipole field compressed by a factor 2 by the boundary currents, and augmented by the background plasma β also assumed constant. B_{eq} is the effective field at the planet's equator, as increased in the outer magnetosphere by the effect of the ring current. The exponent γ describes the compressibility of the magnetosphere. As discussed in section 1.3, the estimated values of this exponent at Saturn range between 6.1 (low compressibility, terrestrial-type magnetosphere) and 4.3 (more compressible, jovian-type magnetosphere). The second term on the right side is the pressure perturbation due to the wave, varying between zero and some maximum value ΔP_{wmax} , taken as a first approximation to be independent of radial distance. With regard to the latter assumption, we note specifically that the amplitude of the wave field is expected to fall with distance much less rapidly than does the background field, such that while wave effects may be negligible compared with the background in the near-planet region, they can readily become comparable with the

background at larger distances. If the boundary position when $\Delta P_w = 0$ is written as R_{MP0} , the value of ΔP_w required to move the boundary to a radius $R_{MP} \geq R_{MP0}$ is then given by

$$\Delta P_w \approx \frac{2(1+\beta)B_{eq}^2}{\mu_o} \left(\frac{R_S}{R_{MP0}} \right)^\gamma \left(1 - \left(\frac{R_{MP0}}{R_{MP}} \right)^\gamma \right) \approx P_{SW} \left(1 - \left(\frac{R_{MP0}}{R_{MP}} \right)^\gamma \right). \quad (4.3)$$

If we put $(R_{MP}/R_{MP0}) \approx 1.1$ for a maximum $\sim 10\%$ increase in the boundary position say, as indicated by the above results, we find $\Delta P_{wmax} \approx 0.44 P_{SW}$ for $\gamma = 6$, and $\Delta P_{wmax} \approx 0.32 P_{SW}$ for $\gamma = 4$. The increase in pressure must thus be a significant fraction of the background pressure just inside the magnetosphere, hence also a significant fraction of the solar wind pressure outside. Increases in pressure of such magnitude due to the magnetospheric period oscillations are entirely compatible with the observations presented here. For example, if we consider flux maximum e' observed near the boundary on the Rev 16 outbound pass, we estimated in section 4.2 above (after reasonable allowance for the ion pressure) that the total pressure increased from ~ 0.025 to ~ 0.035 nPa in the oscillation, corresponding to an increase of just $\sim 40\%$, in excellent agreement with the above estimate.

4.5 Summary and Conclusions

The principal results reported in this chapter are as follows.

- (a) Examination of Cassini magnetic field and plasma data in the outer regions of Saturn's magnetosphere shows that the magnetic oscillations at the magnetospheric period which are ubiquitously present are accompanied by corresponding variations in the electron flux over the energy range from < 10 eV to > 10 keV.
- (b) Magnetopause boundary oscillations at the magnetospheric period also commonly occur, which are in phase with the plasma pressure variations inside the magnetosphere.

Related oscillations in the bow shock position are then also expected, though only marginal evidence for them has been found in the data examined here.

(c) The peak-to-trough amplitude of the magnetopause oscillation on the planet-Sun line is estimated to be typically $\sim 2 R_S$, corresponding to a $\sim 10\%$ change in the boundary radius.

(d) The increase in pressure inside the boundary required to produce such motions is estimated to be $\sim 30 - 40\%$ of the background values, and hence $\sim 30 - 40\%$ of the solar wind dynamic pressure. Such increases are compatible with the observations presented here when reasonable allowance is made for the ion pressure.

We propose that these effects are produced by a global-scale compressive wave which propagates outward through the sub-corotating outer magnetospheric plasma, originating from a near-corotating source in the nearer-planet region. It seems likely that this wave has a profound effect on the plasma dynamics of the outer magnetospheric region, and is the basic causative agent of other oscillating phenomena at Saturn such as modulated kilometric radio emissions [e.g., *Kaiser et al.*, 1980].

Chapter 5

A Simple Theoretical Model of Motion Through an Oscillating Planar Boundary

5.1 Introduction

In Chapters 6 and 7 we examine the oscillations of Saturn's magnetopause and bow shock near the magnetospheric period through statistical studies of the occurrence and timing of multiple boundary encounters during passes of the Cassini spacecraft. It is first instructive, however, to consider expectations based on a simple theoretical formulation, showing, for example, how the number and timing of observed oscillations depends on the motion through the boundary region. The theory developed here is equally applicable to the magnetopause and the bow shock.

5.2 Mathematical Formulation

We consider a planar boundary parallel to the x - y plane that is executing simple harmonic motion in the z -direction about $z = 0$ with amplitude z_{B0} and period τ_B . With regard to the applicability of this simple model to the present problem we note that on the few- R_S spatial scales of magnetopause oscillation estimated in Chapter 4, neither the curvature of the undisturbed magnetopause, nor the variation of oscillation phase with LT around the boundary (as, in effect, a $m = 1$ wave, where m is the azimuthal wave number), are likely to be major effects. The position and velocity of the model boundary can thus be expressed as

$$z_B(t) = z_{B0} \sin\left(\frac{2\pi t}{\tau_B}\right) \quad \text{and} \quad v_B(t) = v_{B0} \cos\left(\frac{2\pi t}{\tau_B}\right), \quad (5.1a,b)$$

where the velocity amplitude of the boundary is

$$v_{B0} = \left(\frac{2\pi z_{B0}}{\tau_B}\right). \quad (5.1c)$$

We assume that the spacecraft is moving normal to the layer with a constant relative speed v_S , which in general will be due to the combined effect of the motion of the spacecraft and the mean motion of the magnetopause due e.g. to solar wind effects. On the above planar boundary assumption, the transverse motion of the spacecraft can be ignored. Its position can thus be expressed as

$$z_S(t) = v_S t + z_{S0}, \quad (5.2)$$

where the arbitrary position z_{S0} at $t = 0$ determines the arbitrary phasing of the spacecraft pass relative to the boundary oscillation. In what follows we will consider only ‘outbound’ passes with $v_S > 0$, but the extension to ‘inbound’ passes with $v_S < 0$ is trivial.

It is useful to normalize the above equations, with velocities being normalized to the velocity amplitude of the boundary, v_{B0} , and times being normalized to the oscillation period, τ_B , such that distances are normalized to $2\pi z_{B0}$. Denoting normalized quantities by primes, the motions of the boundary and the spacecraft are thus represented by

$$z'_B(t') = \frac{1}{2\pi} \sin(2\pi t') \quad \text{and} \quad v'_B(t') = \cos(2\pi t') \quad (5.3a,b)$$

and
$$z'_S(t') = v'_S t' + z'_{S0}, \quad (5.4a)$$

where
$$v'_S = \left(\frac{v_S}{v_{B0}}\right) \quad \text{and} \quad z'_{S0} = \left(\frac{z_{S0}}{2\pi z_{B0}}\right). \quad (5.4b)$$

In normalized units the boundary motion is thus a fixed oscillation, with all the information concerning the relative speed through the layer and the relative phasing being contained in equation (5.4) describing the spacecraft motion.

5.3 Number of Observed Oscillations

We first discuss how the number of oscillations N observed on a given pass depends on the relative speed v'_s and the phasing determined by z'_{s0} . Here an ‘observed oscillation’ means e.g. a ‘re-entry’ into the magnetosphere on an outbound pass due to the motion of the magnetopause, such that a pass with N observed oscillations corresponds to a total of $(2N + 1)$ boundary crossings. It is first evident that no oscillations will be observed if $v'_s \geq 1$, i.e. if the normal speed of the spacecraft equals or exceeds the maximum speed of the boundary, since once having crossed the boundary, the latter cannot then overtake the spacecraft on that pass. However, oscillations may be observed for all $v'_s < 1$, evidently in increasing numbers as v'_s declines towards zero. This is illustrated in Figure 5.1, where in each panel a set of spacecraft trajectories with fixed v'_s are shown by the dashed straight lines, z' versus t' , together with the sinusoidal boundary motion given by equation (5.3), with the value of v'_s declining from the top panel to the bottom.

It is found that a set of critical velocities occurs, written here as v'_N , for which exactly N oscillations are observed independent of the phasing of the pass. At velocities v'_s lying between v'_{N+1} and v'_N , passes with both $N + 1$ and N oscillations (but no other numbers) can occur depending on the relative phasing, with the probability of observing $N + 1$

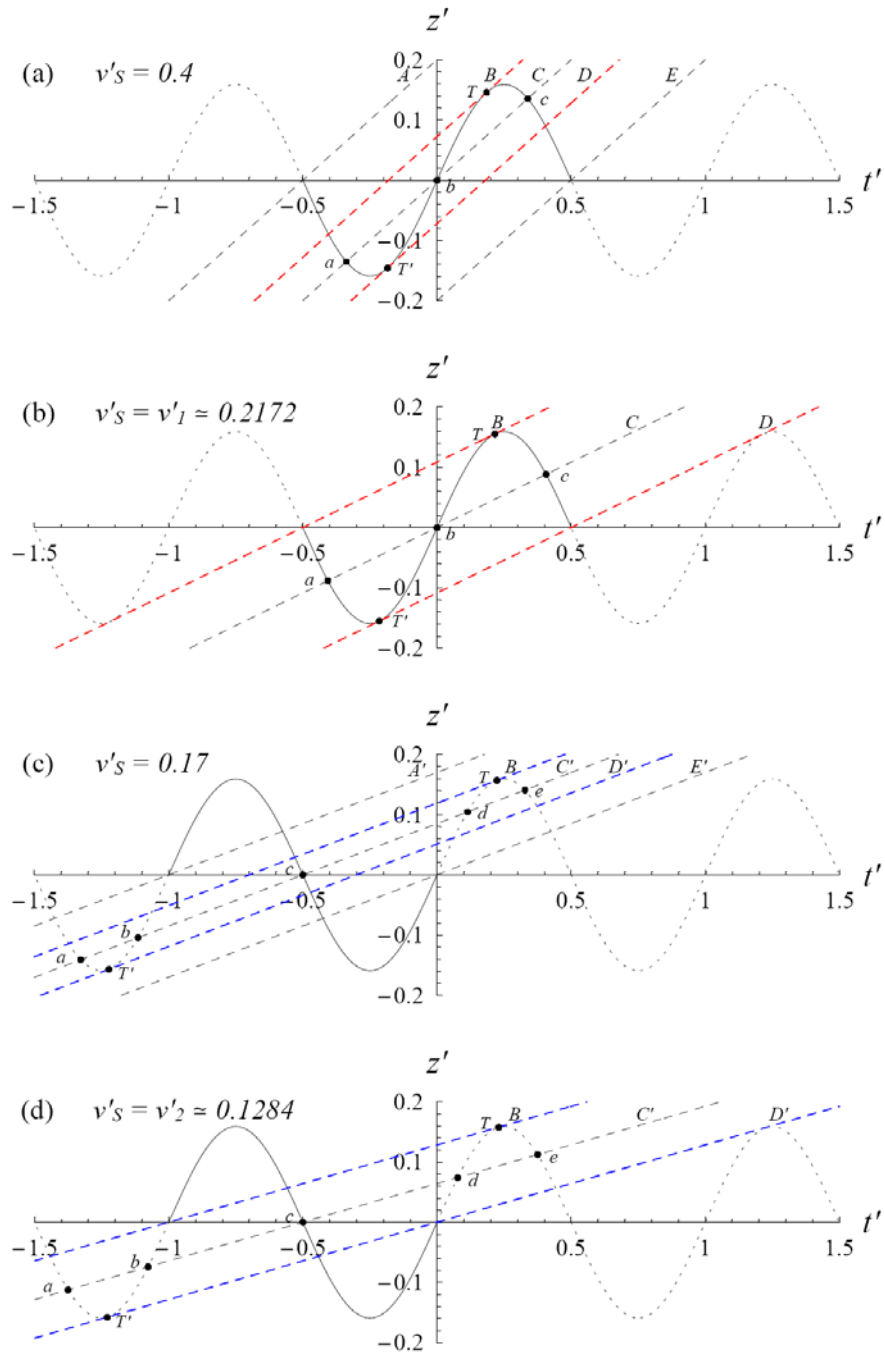


Figure 5.1 Plots of normalized displacement z' versus normalized time t' for a spacecraft with normalized perpendicular velocity v'_s crossing a planar boundary that is in simple harmonic motion. The sinusoid indicates the boundary motion, while the inclined dashed straight lines correspond to spacecraft trajectories.

oscillations decreasing from unity to zero as v'_S increases from v'_{N+1} to v'_N , while the probability of observing N oscillations correspondingly increases from zero to unity.

The top panel in Figure 5.1 shows the situation for $v'_S = 0.4$, lying between v'_1 and v'_0 . Five spacecraft trajectories are shown, labelled A to E , that pass through $z' = 0$ during the interval of the central boundary oscillation indicated by the solid black line. Equivalent trajectories (not shown) then occur periodically in time during preceding and succeeding boundary oscillations shown by the black dotted lines on either side. Trajectories between A and B , and between D and E , pass through the boundary only once, and so do not detect an oscillation, thus corresponding to a $N = 0$ pass. However, trajectories between B and D , centred on trajectory C , pass through the boundary three times, hence observing one oscillation corresponding to a $N = 1$ pass. Limiting trajectories B and D shown by the red dashed lines in panel (a) are tangent to the boundary oscillation curve at points T and T' respectively. They, and their equivalents in other periods, divide the trajectories into separate ‘temporal corridors’ of $N = 0$ and $N = 1$ passes. The $N = 0$ ‘corridors’ are centred on those trajectories that pass through $z' = 0$ at the same time as the boundary surface with the latter moving in the opposite direction to the spacecraft, while the $N = 1$ ‘corridors’ are centred on trajectories that similarly pass through $z' = 0$ at the same time as the boundary surface with the latter moving in the same direction as the spacecraft. The probability of observing $N = 0$ or $N = 1$ passes for this v'_S is then determined from the relative temporal widths of these ‘corridors’, assuming that all phases are equally probable.

We now consider how this diagram changes as v'_s decreases, so that the dashed trajectory lines become less steeply inclined to the horizontal. It is seen from panel (a) of Figure 5.1 that in this case the $N=1$ ‘corridor’ becomes wider and the $N=0$ ‘corridor’ narrower, such that $N=1$ passes become increasingly probable and $N=0$ passes decreasingly probable as v'_s decreases. A critical condition is reached when tangent trajectory B passes through $z'=0$ at time $t'=-0.5$, and simultaneously tangent trajectory D through $z'=0$ at $t'=0.5$, such that trajectories A and B , and D and E then in effect coalesce. This condition occurs at $v'_s = v'_1 \approx 0.2172$ as will be quantified below, and is shown in panel (b). In this situation $N=0$ trajectories disappear, and all trajectories pass through the boundary just three times corresponding to $N=1$ passes, the probability for which is then unity.

As v'_s declines further, ‘corridors’ of $N=2$ passes then appear, as shown for $v'_s = 0.17$ in panel (c) of Figure 5.1. In this diagram the $N=2$ ‘corridor’ occurs between the blue dashed lines B and D' that are tangent to the oscillating boundary curve at T and T' , respectively. Between these lines, e.g. on trajectory C' , the trajectories cross the boundary five times, corresponding to two observed oscillations, while outside this ‘corridor’ between trajectories A' and B , and D' and E' , $N=1$ passes with three boundary crossings continue to occur. The relative probability of $N=1$ and $N=2$ passes is again given by the relative widths of these ‘corridors’ over one oscillation of the boundary, with the $N=1$ ‘corridor’ again being centred on trajectories such as A' and E' that pass through $z'=0$ at the same time as the boundary travelling in the same direction, while the $N=2$ ‘corridor’ is centred on trajectories such as C' that pass through $z'=0$ at the same time as the boundary travelling in the opposite direction. With further decrease of

v'_s , a second critical velocity is then reached at $v'_s = v'_2 \approx 0.1284$, when tangent trajectory B passes through $z' = 0$ at $t' = -1$, and simultaneously trajectory D' passes through $z' = 0$ at $t' = 0$, such that trajectory B in panel (c) coalesces with A' , and D' coalesces with E' . In this case, depicted in panel (d), all trajectories pass through the boundary just five times, corresponding to $N = 2$ passes with a probability of unity. Equivalent effects then continue to unfold as v'_s decreases further.

To determine the values of the critical velocities we now focus on the lines marked B in Figure 5.1 that are tangent to the boundary curve at the points marked T . The tangent condition $v'_s = \cos(2\pi t'_T)$ readily yields the position of the tangent point as

$$t'_T = \frac{1}{2\pi} \cos^{-1} v'_s \quad \text{and} \quad z'_T = \frac{1}{2\pi} \sqrt{1 - v'^2_s} . \quad (5.5a,b)$$

At critical velocity v'_N this line also passes through $z' = 0$ at times $t' = -N/2$ (e.g. panel (b) of Figure 5.1 for $N = 1$ and panel (d) for $N = 2$). Thus on these trajectories the spacecraft moves distance z'_T in time $(N/2 + t'_T)$, at a speed corresponding to v'_N , i.e. we have the condition $v'_N = z'_T / (N/2 + t'_T)$. Substituting from equation (5.5) and rearranging we thus have the condition

$$v'_N (\pi N + \cos^{-1} v'_N) = \sqrt{1 - v'^2_N} , \quad (5.6)$$

where we specifically focus on the value of the inverse cosine function between 0 and $\pi/2$ for v'_N positive. Equation (5.6) is readily solved numerically (using Newton's method) for v'_N , giving the values shown in Table 5.1 for $N = 0$ to 8. We note that $v'_0 = 1$, since only passes of type $N = 0$ (with one boundary crossing) are observed when the speed of the

| N | Normalized relative velocity for $P_N = 1$ v'_N (see Fig 5.2) | Approximation to $v'_N \approx \frac{1}{\left(\pi\left(N + \frac{1}{2}\right)\right)}$ | $k_B = \tau'_C = (\tau_C / \tau_B)$ at $v'_S = v'_N$ for N odd & even (red & blue curves in Fig 5.3 respectively) | $k_A = (z_L / z_{B0})$ at $v'_S = v'_N$ for N odd & even (red & blue curves in Fig 5.5 respectively) |
|-----|---|---|--|---|
| 0 | 1.0 | 0.636620 | 0.0 | 0.0 |
| 1 | 0.217234 | 0.212207 | 0.812825 | 1.10944 |
| 2 | 0.128375 | 0.127324 | 0.875253 | 1.41196 |
| 3 | 0.091325 | 0.090946 | 0.915408 | 1.55828 |
| 4 | 0.070914 | 0.070736 | 0.931856 | 1.64524 |
| 5 | 0.057972 | 0.057875 | 0.944946 | 1.70310 |
| 6 | 0.049030 | 0.048971 | 0.952597 | 1.74446 |
| 7 | 0.042480 | 0.042441 | 0.959144 | 1.77554 |
| 8 | 0.037475 | 0.037448 | 0.963573 | 1.79977 |

Table 5.1 Values associated with the theoretical boundary crossing analysis in this chapter.

spacecraft and the maximum speed of the boundary are equal, and that v'_N decreases towards zero as N increases. A close approximation for large N can be obtained by noting that in this limit $t'_T \approx 1/4$ and $z'_T \approx 1/2\pi$, which yields the result

$$v'_N \approx \frac{1}{(\pi(N+1/2))} , \quad (5.7a)$$

values for which are also given in Table 5.1. For N reasonably large

$$v'_N \approx 1/\pi N \quad (5.7b)$$

is an adequate approximation.

Related considerations also yield expressions for the probability of observing $N+1$ and N oscillations when v'_S lies between v'_{N+1} and v'_N . We again consider the trajectory that is tangent to the boundary curve between $0 \leq t' \leq 0.25$, corresponding to the trajectories labelled B in the panels of Figure 5.1. At critical velocity v'_N this passes through $z' = 0$ at $t' = -N/2$ as just indicated. For a somewhat smaller speed (but larger than v'_{N+1}) it passes through $z' = 0$ at a somewhat earlier time that we denote as $t' = -(N/2 + \Delta t')$, such that $v'_S = z'_T / (t'_T + N/2 + \Delta t')$ where the tangent positions z'_T and t'_T are given by equation (5.5). Rearranging, we thus obtain $\Delta t' = (z'_T / v'_S) - N/2 - t'_T$. The displacement $\Delta t'$ then defines the width of the ‘corridor’ of $N+1$ passes, given by $P_{N+1} = 2\Delta t'$ (see e.g. panel (c) of Figure 5.1). Substitution of equation (5.5) into the expression for $\Delta t'$ then yields

$$P_{N+1} = \frac{1}{\pi} \left(\frac{\sqrt{1-v'^2_S}}{v'_S} - \cos^{-1} v'_S \right) - N , \quad (5.8a)$$

where again the angle given by the inverse cosine function is taken to lie between 0 and $\pi/2$ for v'_s positive. Since perforce we must also have $P_{N+1} + P_N = 1$, we also have

$$P_N = 1 - P_{N+1} . \quad (5.8b)$$

These probabilities are plotted versus v'_s in Figure 5.2, where the solid black dots indicate the critical velocities v'_N , as marked at the top of the plot. The sequence of blue curves shows the probabilities for even N , for $N = 0, 2$, and 4 on moving from right to left in the figure, which peak at unity at v'_0, v'_2 , and v'_4 as shown. Similarly the sequence of red curves shows the probabilities for odd N , for $N = 1, 3$, and 5, which peak at unity at v'_1, v'_3 , and v'_5 . In section 6.8 these results will be compared with observed statistics of numbers of boundary oscillations to estimate the typical boundary speed from the spacecraft speed normal to the boundary.

5.4 Timing of Boundary Crossings

We now consider two related topics concerning the timing of boundary crossings. The first concerns the time between successive like crossings of the boundary (e.g. from ‘inside’ to ‘outside’), through which we may expect to relate the observed oscillations to the other oscillatory magnetospheric phenomena discussed in Chapter 2. Specifically, we focus here on the time between the first, third, fifth etc. boundary crossings, if such there be. It can be seen from Figure 5.1 that due to the motion of the spacecraft through the boundary, these intervals are always less than the boundary oscillation period, a result that holds for both outbound and inbound passes. For example, if we examine trajectory C in panel (a), the interval between crossings a and c is clearly less than one oscillation period,

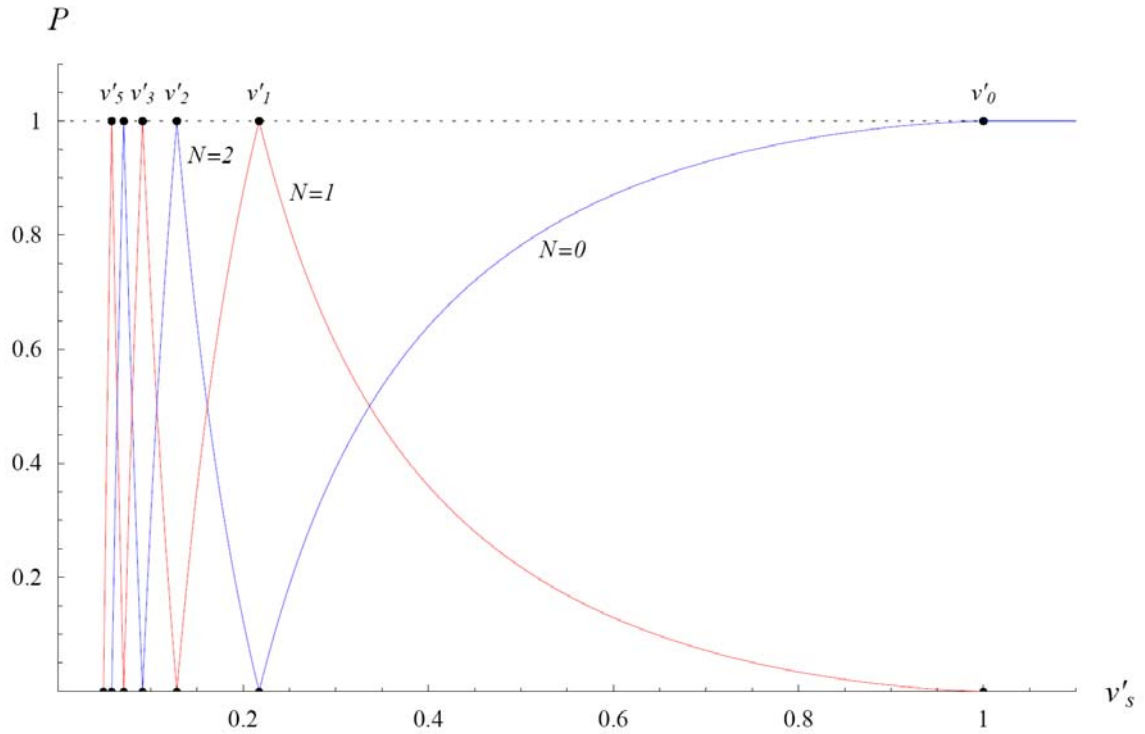


Figure 5.2 The probability P of observing N boundary oscillations, plotted versus the normalized velocity of the spacecraft v'_s . The sequence of blue curves shows the probabilities for $N = 0, 2$, and 4 , while the sequence of red curves shows the probabilities for $N = 1, 3$, and 5 . Solid black dots at the top and bottom of the plot indicate critical velocities v'_N , at which only N oscillations (and no other number) can be observed.

as are the intervals between a and c , and c and e in panel (c). While it is evident that the exact value of these intervals depends on the detailed phasing of the pass, examination shows that representative values can be obtained by considering the trajectories at the centre of each ‘temporal corridor’ of given N . For example, representative values for $N=1$ passes between v'_2 and v'_0 are obtained from the condition (from equations (5.3a) and (5.4a) with $z'_{s0} = 0$ at the centre of the ‘corridor’, see Figure 5.1 panels (a)-(c))

$$v'_s t' = \frac{1}{2\pi} \sin(2\pi t') . \quad (5.9)$$

This equation gives three roots for t' corresponding to points a , b , and c in panel (a) of Figure 5.1, namely t_c , $t_b = 0$, and $t_a = -t_c$, from which the time between the first and third boundary crossings is given by $\tau'_C = 2t_c$ (compared with the true normalized boundary period of $\tau'_B = 1$). The red line in Figure 5.3 shows the value of τ'_C versus v'_s , from which it can be seen that the value is ~ 0.9 when $v'_s = v'_2$, but falls monotonically towards zero as v'_s increases towards 1. The intervals between such crossings can thus become much shorter than the true boundary period as v'_s approaches unity, though Figure 5.2 shows that the probability of observing such crossings is low. Roots corresponding to point c on trajectory C in panel (a) of Figure 5.1 can continue to be determined from equation (5.9) for speeds v'_s below v'_2 , then corresponding to the centre oscillation only of all odd N passes. For example, between v'_4 and v'_2 the red line in Figure 5.3 shows the interval between the third and fifth (of seven) boundary crossings at the centre of the $N=3$ ‘corridor’. These intervals then continue to provide representative values that approach $\tau'_C \rightarrow 1$ (i.e. the true boundary period) as $v'_s \rightarrow 0$. The blue line in Figure 5.3 between v'_3

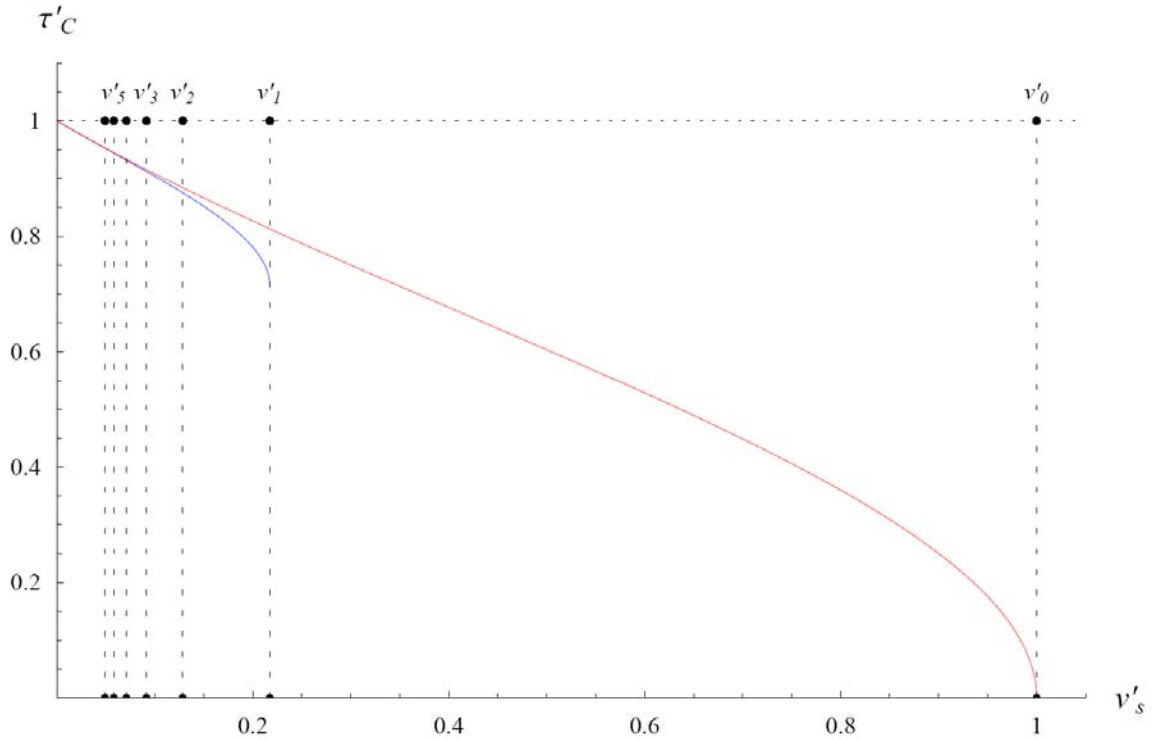


Figure 5.3 Normalized time τ'_C between successive crossings from ‘below’ to ‘above’ the boundary shown in Figure 5.1, approximating the true boundary oscillation period to which τ'_C is normalized, plotted versus v'_s . The red line shows τ'_C for the middle oscillation for odd numbers of oscillations ($N = 1, 3, 5 \dots$), thus corresponding to the red lines in Figure 5.2, while the blue line shows τ'_C for the middle two oscillations for even numbers of oscillations ($N = 2, 4, 6 \dots$), thus corresponding to the blue lines in Figure 5.2. In all cases the value of τ'_C shown is the representative value corresponding to the centre of the ‘corridor’ of spacecraft trajectories of given N for given v'_s (e.g. the trajectories marked A' , C , C' or E' in Figure 5.1). Solid black dots mark the critical velocities v'_N , as in Figure 5.2.

and v'_1 similarly shows τ'_C values at the centre of the $N = 2$ ‘corridor’ corresponding to the (equal) intervals between points a and c , and c and e on trajectory C' in panel (c) of Figure 5.1. These are smaller than, but comparable to, those shown by the red line at the same v'_S values, ~ 0.7 to ~ 0.9 , showing that when multiple oscillations are observed, the observed period is expected to be shorter than but reasonably close to the true period, unless other influences on the boundary position are simultaneously present (due e.g. to solar wind variations). For speeds v'_S less than v'_3 , the blue line in Figure 5.3 then corresponds to the intervals associated with the central two oscillations only of all even N passes. These again provide representative values, showing a similar increase to $\tau'_C \rightarrow 1$ as $v'_S \rightarrow 0$ as for odd N . The values of these quantities at v'_N are given in Table 5.1 for future use in section 6.8.

The second related topic concerns the determination of the oscillation phase from boundary crossing observations. If we consider panel (a) of Figure 5.1, for example, it can be seen (in this case) that the ‘re-entry’ inside the boundary between points b and c on trajectory C , while spanning a boundary maximum, is not centred on the latter, because of the spacecraft motion through the oscillation layer. In other words, the ‘centre’ of such a ‘re-entry’, occurring at time $t' = t_c/2$, is not contemporaneous with the boundary maximum at $t' = 0.25$, but occurs at an earlier time. This effect thus results in the centre times of observed oscillations occurring earlier than boundary maxima on outbound passes, and correspondingly later than boundary maxima on inbound passes (as readily seen by reversing the direction of trajectory motion in Figure 5.1). At the centre of the $N = 1$ band

in panel (a), for example, the time difference is $\Delta t' = (0.25 - t'_c/2)$, where t'_c is obtained from equation (5.9), which may conveniently be expressed as a phase difference

$$\Delta\psi = 360\Delta t' = 360(0.25 - t'_c/2) \text{ deg} . \quad (5.10)$$

This phase difference is shown versus v'_s as the red line in Figure 5.4, where again for $v'_s \leq v'_2$ this corresponds to the centre oscillation of all odd N passes at the centre of the corresponding ‘corridor’, as in Figure 5.3. It can be seen that the phase shifts can become very large, approaching 90° , as v'_s approaches 1. However, as shown in Figure 5.2, observations of such oscillations are of increasingly low probability. Observations of oscillations become reasonably probable only for $v'_s \leq 0.5$, say, for which values the phase shifts are typically a few tens of degrees or less, with $\Delta\psi \rightarrow 0$ as $v'_s \rightarrow 0$. The two blue lines in Figure 5.4 between v'_3 and v'_1 then correspond to the phase shifts of the two $N = 2$ oscillations observed between these v'_s values, where the upper solid line corresponds to the first of these oscillations (e.g. the phase shift corresponding to points b and c in panel (c) of Figure 5.1), and the lower dashed line to the second (e.g. points d and e in the same figure). Again, these phase shifts are modest in the region where such oscillations are reasonably probable (see the blue lines peaked at v'_2 in Figure 5.2). For $v'_s \leq v'_3$ the blue lines then relate to the two centre oscillations of all even N passes at the centres of the corresponding ‘corridors’, as in Figure 5.3, again showing how the phase shift falls towards zero as v'_s nears zero. These results will be discussed in section 6.7.

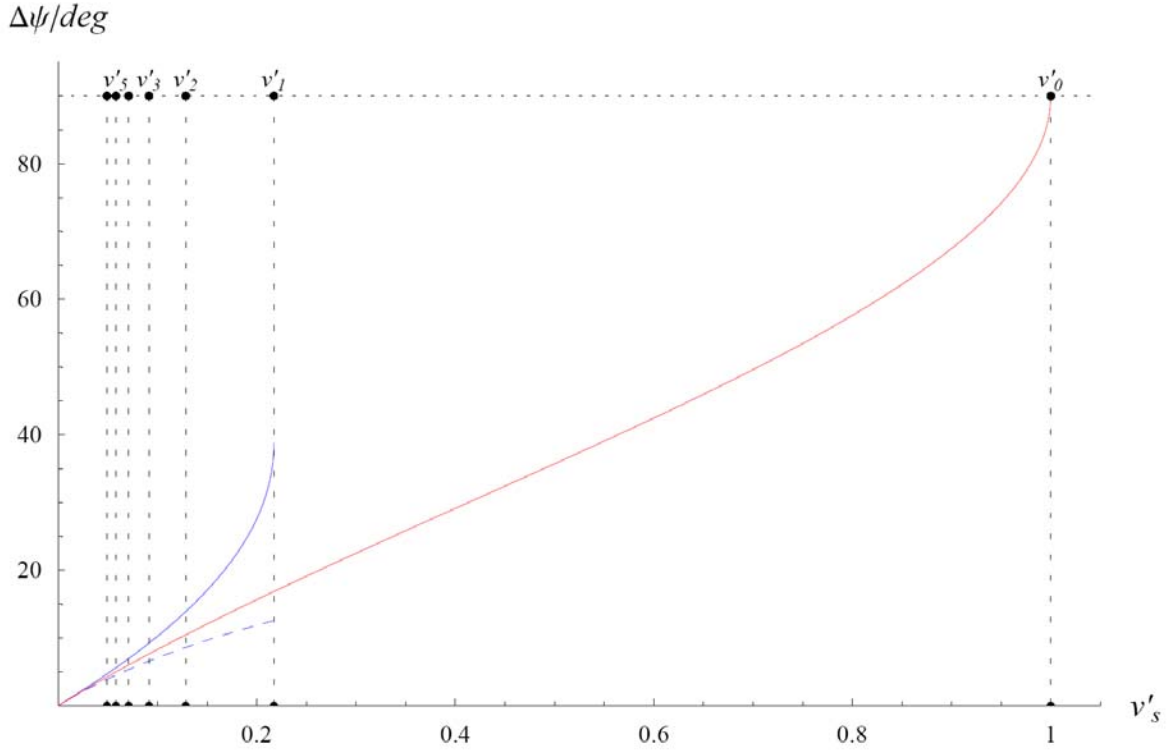


Figure 5.4 Plot of phase shift $\Delta\psi$ versus v'_s , where $\Delta\psi$ is the phase difference between the phase of the observed centre time of a boundary oscillation and the phase at the true centre time of the oscillation (where phase difference $\Delta\psi$ is related to time difference Δt by $\Delta\psi = 360\Delta t/\tau_B$ deg). The red line shows the phase shift for the centre oscillation for odd numbers of oscillations ($N = 1, 3, 5\dots$), while the blue lines show the phase shift for the two centre oscillations for even numbers of oscillations ($N = 2, 4, 6\dots$), where the upper solid line corresponds to the first of the two oscillations and the lower dashed line to the second. In all cases the value of $\Delta\psi$ shown is the representative value corresponding to the centre of the ‘corridor’ of spacecraft trajectories of given N for given v'_s . Solid black dots mark the critical velocities v'_N as in Figure 5.2.

5.5 Width of the Oscillation Layer

A simple approach to estimating the amplitude of the boundary oscillations is to examine the spacecraft displacement normal to the boundary between first and last contacts, as will be discussed in section 6.8. It is evident from Figure 5.1 that this displacement will always be less than twice the amplitude, considerably so under some circumstances, depending on the speed relative to the boundary and the detailed phasing of the crossing. Examination again shows, however, that results determined from the centre trajectories within the ‘temporal corridors’ of given N provide representative values, with results shown in Figure 5.5. Here we show the displacement of the spacecraft normal to the boundary between first and last magnetopause encounters z_L , representing an estimate of the width of the oscillation layer, normalized to the oscillation amplitude of the boundary z_{B0} , plotted versus v'_S . (We note that in the normalized units of section 5.2 $(z_L/z_{B0}) = 2\pi z'_L$ since in these units the boundary oscillation amplitude is $1/2\pi$, as in Figure 5.1.) From right to left in the figure the sequence of red lines corresponds to $N = 1$ plotted between v'_2 and v'_0 , $N = 3$ plotted between v'_4 and v'_2 , and so on, while the sequence of blue lines corresponds to $N = 2$ plotted between v'_3 and v'_1 , $N = 4$ plotted between v'_5 and v'_3 , and so on, up to the final red and blue lines corresponding to $N = 7$ and 8. It can be seen that a broad range of (z_L/z_{B0}) values is possible ranging e.g. from ~ 1.1 to 2 for $N = 2$. However, according to the results shown in Figure 5.2, the probability of observing a crossing of given N is generally strongly peaked at speed v'_N , and these points are marked by dots on the appropriate curves. Focusing on these points of maximum probability, it can be seen that we expect $(z_L/z_{B0}) \sim 1.1$ for $N = 1$, increasing to ~ 1.4 for

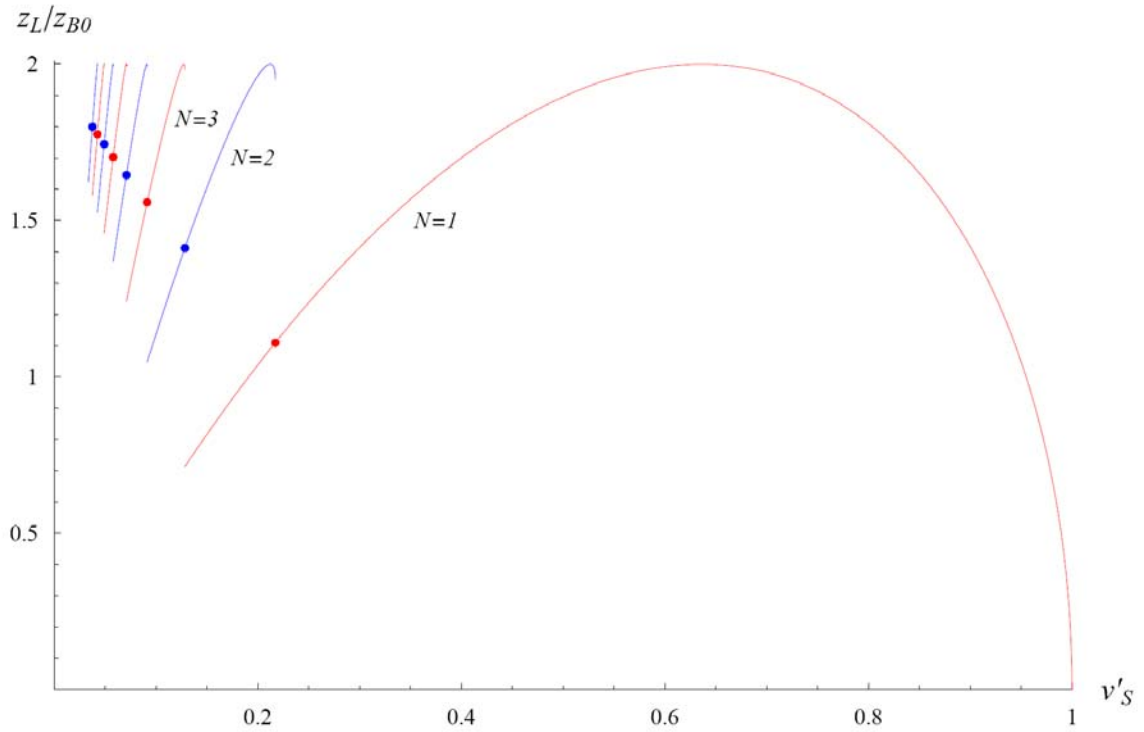


Figure 5.5 Displacement of the spacecraft normal to the boundary between the first and last boundary crossings z_L , normalized to the oscillation amplitude of the boundary z_{B0} , plotted versus v'_S . From right to left the sequence of red lines corresponds to $N = 1, 3, 5,$ and 7 , while the sequence of blue lines corresponds to $N = 2, 4, 6,$ and 8 , plotted in each case between the corresponding values of v'_{N+1} and v'_{N-1} . The solid dots mark the values of (z_L/z_{B0}) at the critical velocities v'_N , at which velocity the probability of observing a crossing with the given N is unity (see Figure 5.2). The values shown are again representative values corresponding to the centre of the ‘corridor’ of spacecraft trajectories of given N for given v'_S .

$N = 2$, and to ~ 1.8 for $N = 8$. These values are also recorded for future reference in Table 5.1, for use in sections 6.8 and 7.5.

5.6 Summary and Discussion

In this chapter we have developed a model consisting of a planar boundary undergoing simple harmonic motion and a spacecraft moving perpendicular to the boundary layer at a constant relative velocity, normalized to the boundary velocity amplitude, of v'_S . The principal results of this theoretical study and the main uses to which they are put in the data-based studies of Chapters 6 and 7 are as follows.

(a) We find that there is a set of critical velocities v'_N for which exactly N oscillations occur independent of the phasing of the pass. At velocities v'_S lying between v'_{N+1} and v'_N , passes with both $N + 1$ and N oscillations can occur depending on the relative phasing. As v'_S increases from v'_{N+1} to v'_N , the probability of observing $N + 1$ oscillations decreases from unity to zero while the probability of observing N oscillations correspondingly increases from zero to unity. In section 6.8 we use Figure 5.2 to estimate a representative value of v'_S for our set of $N = 1$ magnetopause oscillation episodes from the relative numbers of $N = 1$ and $N = 0$ episodes in our data set. This value of v'_S is then used to estimate the typical velocity amplitude of the magnetopause and thence (since the oscillation period is known) the typical displacement amplitude.

(b) Due to the motion of the spacecraft through the boundary, the observed interval between successive like crossings of the boundary should always be shorter than the oscillation period (if no other sources of boundary motion are present). This result holds

for both inbound and outbound passes. In Chapters 6 and 7 we select boundary oscillation events for analysis by imposing timing windows that specify a range of intervals between successive like crossings. These windows are not ‘capped’ at the magnetospheric period, because a range of phenomena additional to the magnetospheric period oscillation will also affect the boundary position such that the observed intervals can be longer (or shorter) than would be expected from theoretical considerations.

(c) The ‘centre time’ of a re-entry does not coincide with the time of maximum outward boundary displacement, but occurs at a later time for inbound passes and at an earlier time for outbound passes. However, within the range of v'_s in which the observation of boundary oscillations is reasonably likely the associated phase shifts are modest (no more than a few tens of degrees). This result supports our use, in Chapters 6 and 7, of the phase at the centre time of a re-entry as a proxy for the phase at the time of maximum outward boundary excursion. In section 6.7 we examine our data for evidence of these systematic phase shifts and find that they are not discernible, hence their effect must be small compared with the overall scatter.

(d) We have examined how the ratio of the displacement of the spacecraft normal to the boundary between the first and last crossings of an episode (which gives a lower limit to the peak-to-trough amplitude if no other boundary motions are present) and the boundary’s true oscillation amplitude depends upon v'_s . In sections 6.8 and 7.5 we use representative values of this ratio to ‘correct’ the mean observed displacements and thus obtain estimates of the true amplitude.

Chapter 6

Magnetospheric Period Oscillations of Saturn's Magnetopause: Occurrence, Phase, and Amplitude

6.1 Introduction

In Chapter 4, we used magnetic and plasma data from two Cassini orbits to exemplify our discovery that Saturn's magnetopause moves in and out in response to periodic variations in the total (i.e. magnetic plus plasma) magnetospheric pressure. In this chapter we make a first systematic study of the magnetospheric period magnetopause oscillations, using data from ~ 40 Cassini orbits that crossed the magnetopause during 2004-2007, and the theory developed in Chapter 5. In Chapter 7 we extend this analysis to the bow shock. Because the motion of the spacecraft through the boundary region, combined with other boundary effects, produces a broad spread in timings between successive like crossings (e.g. from 'inside' to 'outside'), boundary oscillation events are selected for analysis using a broad timing window between 0.4 and 1.6 of the magnetospheric period. These events are found to be highly organized by the phase of the interior field oscillations, showing that they relate to boundary oscillations that have a closely common period. We determine the proportion of spacecraft passes through the boundary region on which such oscillations are observed, consider the spatial distribution of the oscillations, and estimate their amplitude. Finding that the oscillation phase depends somewhat on radial distance to the boundary, we make estimates of the radial phase speed. We conclude this chapter by examining the relationship between the magnetopause boundary oscillations and some of the other oscillatory phenomena discussed in Chapter 2.

6.2 *Data Set Employed*

In this section we outline the Cassini data set employed in the study, based on magnetic field and plasma electron data. We use data from SOI up to the inbound pass of Rev 55 in late December 2007, the latter being the limit of the interval in which the phase of the ‘core’ magnetic field oscillations has been determined by *Provan et al.* [2009a], to which the boundary oscillations will be related. Most of the data (SOI–Rev 28 and Revs 46–55) are near-equatorial, with the spacecraft remaining within $\sim 20^\circ$ of the planetary equator, except for a high-inclination interval (Revs 29–45) during late 2006 and the first half of 2007 in which the orbit plane was tilted significantly out of the equatorial plane. However, during mid- to late-2006 (Revs 24–37) apoapsis was located on the nightside so no magnetopause crossings were then observed. The orbits employed thus divide into two intervals, the first of which (SOI–Rev 23) involves crossings of the dawn to noon magnetopause at low latitudes, while the second (Revs 38–55) involves crossings of the noon to post-noon magnetopause, some of which are at latitudes significantly away from the equator.

Boundary transitions are identified using 1 min averaged field data from the Cassini fluxgate magnetometer, together with 1 min averaged electron data in the energy range 0.6 eV to 26 keV from anode 5 of the electron spectrometer (ELS) sensor. On crossing from the magnetosheath to the magnetosphere the magnetometer typically observes an increase in the field strength, generally accompanied by a change in direction to southward orientations and a reduction in variability, while the ELS instrument records a substantial reduction in the electron flux in the ~ 10 to ~ 100 eV energy range and an increase at ~ 100 eV to ~ 1 keV. Transitions are usually sharp, allowing crossings to be timed to the

nearest minute or few minutes, uncertainties of this order being insignificant compared with the ~ 11 h time scales of interest. When multiple crossings on time scales of less than ~ 15 min were identified, the time at the midpoint was recorded. In addition, brief boundary crossings on similar or shorter time scales occurring within otherwise continuous magnetosphere or magnetosheath intervals were disregarded. Where ELS and magnetic data were both available, they were used in combination. If there was a gap in the magnetic data, the identification and timing of crossings was made from the ELS data alone, and vice versa. Significant simultaneous gaps in both records necessitated the exclusion of 8 passes (4 inbound, 4 outbound), as indicated in Table 6.1 to be introduced in section 6.5. Several other passes are affected to varying degrees by data gaps lasting from a few minutes to several hours, but are not rendered wholly unusable. In all, timings and positions of magnetopause crossings were recorded for ~ 40 Cassini orbits.

6.3 Relation to the Magnetic Oscillation Phase in the ‘Core’ Magnetosphere

The data set contains several examples of multiple magnetopause encounters on a given pass, such as those described in Chapter 4. Examples in which there are several re-entries separated by intervals of ~ 11 h provide convincing evidence of such boundary oscillations. Much more frequently, however, only one or two such re-entries are observed on a pass, these showing a broad spread in the boundary crossing interval that is no doubt due both to the finite speed of the spacecraft through the oscillation layer (section 5.4), combined with the effects of other phenomena that cause boundary motions such as changes in solar wind dynamic pressure or surface waves. Such examples provide evidence that is rather less clear-cut. In this section we thus examine whether these re-entries,

defined within a relatively broad timing window about the magnetospheric period, are indeed related to large-scale oscillations of the boundary at this period by examining whether their phasing is related to the phase of the field oscillations observed within the magnetospheric ‘core’. Demonstration of a clear phase relationship implies that they are related oscillatory phenomena with a closely common synodic period.

In conformity with observations, *Provan et al.* [2009a] express the oscillatory field in spherical polar components in the ‘core’ (defined to be dipole $L \leq 12$) by

$$B_{r,\theta}(\varphi,t) = B_{0r,\theta} \cos(\Psi_{Mc}(\varphi,t)) \quad \text{and} \quad B_{\varphi}(\varphi,t) = B_{0\varphi} \sin(\Psi_{Mc}(\varphi,t)) \quad , \quad (6.1a)$$

where ‘core’ phase function $\Psi_{Mc}(\varphi,t)$ is given by

$$\Psi_{Mc}(\varphi,t) = \Phi_M(t) - \varphi \quad . \quad (6.1b)$$

In equation (6.1b) $\Phi_M(t)$ is the phase function of the magnetic field oscillations to be discussed below, while φ is azimuth measured from the noon meridian, positive in the sense of increasing LT. The r and θ field components are thus in phase with one another, while being in leading quadrature with the φ field component, as outlined in Chapter 2. Note that if $B_{0r} = B_{0\varphi} = B_0$, the oscillatory field lying in the equatorial plane, described by the r and φ field components, takes the form of a uniform unidirectional field of magnitude B_0 , that at any instant of time points at an azimuthal angle relative to the solar direction given by

$$\varphi_M(t) = \Phi_M(t) \quad , \quad (6.2)$$

where φ_M is again measured anti-clockwise from noon in the sense of increasing LT. The field direction then rotates in the sense of planetary rotation as $\Phi_M(t)$ increases with time, e.g. pointing towards the Sun at successive instants given by

$$\Phi_M(t) = 360N \text{ deg} , \quad (6.3)$$

where N is any integer and Φ_M is expressed in degrees. These times then also correspond to times at which B_θ maxima in the ‘core’ region lie on the noon meridian.

In the *Provan et al.* [2009a] model, valid over the interval from SOI to Rev 55 (July 2004-December 2007), the phase function $\Phi_M(t)$ is expressed as a fifth order polynomial in time t , determined from fits to filtered residual field data during successive periapsis passes of Cassini through the ‘core’, using the SKR phase of *Kurth et al.* [2008] as an exact ‘guide’ phase. That is, the magnetic phase function is written as $\Phi_M(t) = \Phi_{SKR}(t) - \psi_M(t)$, where $\Phi_{SKR}(t)$ is the SKR phase function of *Kurth et al.* [2008], expressed as a fifth order polynomial in t , and relative phase $\psi_M(t)$ is expressed as a third order polynomial in t . The resulting expression for $\Phi_M(t)$ is

$$\Phi_M(t) = \frac{360t}{\tau_0} - \Delta\Phi_M(t) \text{ deg} , \quad (6.4a)$$

where $\tau_0 = 0.4497$ days, and $\Delta\Phi_M(t)$ is given by the sum of

$$\Delta\Phi_{SKR}(t) = k_0 + k_1t + k_2t^2 + k_3t^3 + k_4t^4 + k_5t^5 \quad (6.4b)$$

and

$$\psi_M(t) = k_{M0} + k_{M1}t + k_{M2}t^2 + k_{M3}t^3 , \quad (6.4c)$$

where $k_0 = 86.6681 \text{ deg}$ $k_1 = -2.7537 \text{ deg day}^{-1}$

$$k_2 = 4.7730 \times 10^{-3} \text{ deg day}^{-2} \quad k_3 = -4.8755 \times 10^{-6} \text{ deg day}^{-3} \quad (6.4d)$$

$$k_4 = 3.5653 \times 10^{-9} \text{ deg day}^{-4} \quad k_5 = -9.1485 \times 10^{-13} \text{ deg day}^{-5} ,$$

and $k_{M0} = 209.2 \pm 41.9 \text{ deg}$

$$k_{M1} = -0.5718 \pm 0.1719 \text{ deg day}^{-1} \quad (6.4e)$$

$$k_{M2} = (1.1446 \pm 0.2160) \times 10^{-3} \text{ deg day}^{-2}$$

$$k_{M3} = (-0.5995 \pm 0.0836) \times 10^{-6} \text{ deg day}^{-3} .$$

In these expressions t is the epoch time in days since the start of 1 January 2004. The deviation of this phase from linear behaviour in one oscillation is very small, such that the instantaneous rotation period of the field perturbation (the ‘magnetospheric period’) is well approximated by

$$\tau_M(t) = \frac{360}{\left(\frac{d\Phi_M}{dt} \right)} , \quad (6.5)$$

where Φ_M is again expressed in degrees. Over the interval studied here, the period increased near-monotonically from $\sim 10.77 \text{ h}$ at SOI to $\sim 10.83 \text{ h}$ at Rev 55.

6.3.1 Preliminary Study

Using the data set described in section 6.2, we divided each apoapsis pass into a whole number of oscillations of Provan phase, starting with the oscillation containing the first magnetopause crossing outbound and finishing with the oscillation containing the last magnetopause crossing inbound. We then considered each oscillation of Provan phase

separately. Each oscillation was divided into thirty-six 10° bins. Each bin was assigned a value of 1 if the spacecraft was inside the boundary (i.e. within the magnetosphere), or 0 if outside the boundary (i.e. in the magnetosheath or solar wind), or if a magnetopause crossing had taken place in that bin, a value between 0 and 1 calculated from the proportion of the bin spent in each of the two regimes. Oscillations without crossings or that held data gaps were discarded and the remaining oscillations summed. The value held in each bin was then divided by the total number of oscillations of Provan phase contributing, to give the probability of being inside rather than outside the boundary when in the boundary region as a function of the Provan phase (modulo 360°). Results are shown in Figure 6.1, in which the horizontal dashed line marks the mean value of the computed probability. It can be seen that there is a broad ‘preferred sector’ of Provan phase centred on $\sim 150^\circ - 160^\circ$ in which the spacecraft has an enhanced probability of being inside the boundary rather than outside. The existence of this ‘preferred sector’ (and the corresponding ‘depleted sector’) is evidence of outward (and inward) excursions of the boundary at the magnetospheric period. Note that in this preliminary study we have not employed any timing window to select events for analysis.

6.3.2 Main Study

We first surveyed each pass through the boundary region for successive like crossings that might potentially be related to the internal field oscillations. We note from section 5.4 and Figure 5.3 that the intervals between these crossings should always be less than the true oscillation period of the boundary, but that those with very much shorter intervals should be relatively rare (see Figure 5.2). However, we recognize that the position of the boundary

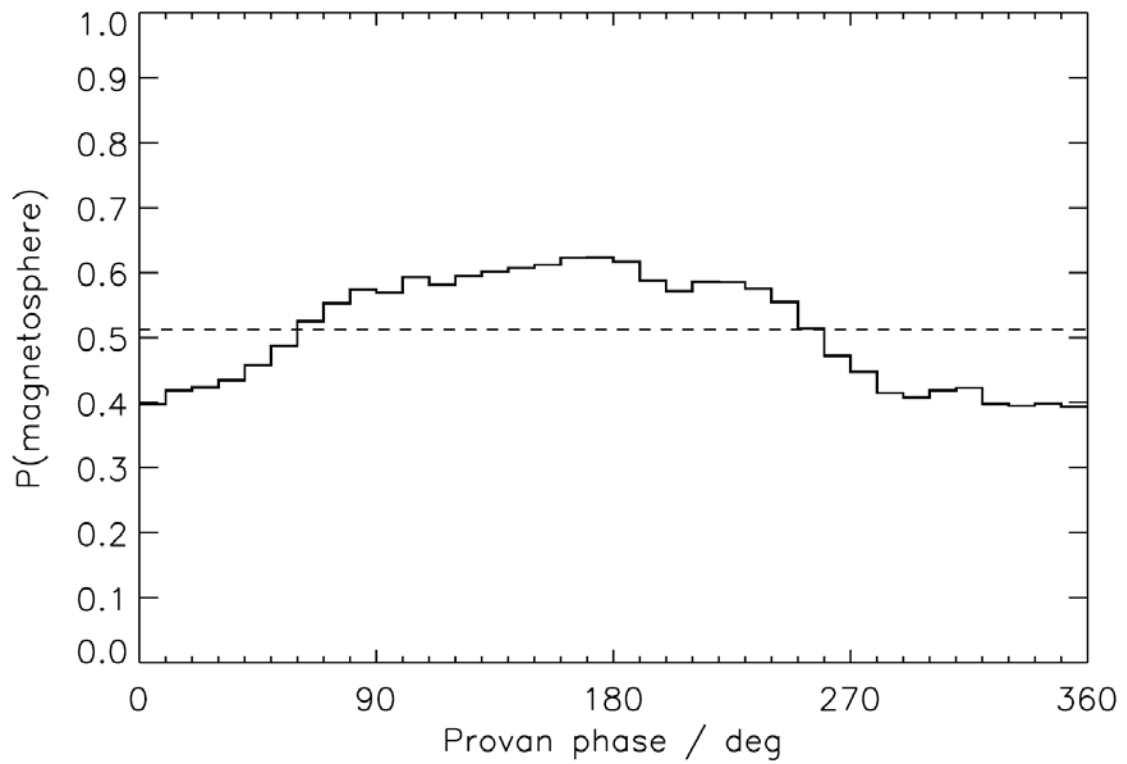


Figure 6.1 The computed probability of being inside rather than outside the magnetopause boundary when in the boundary region as a function of the Provan phase (modulo 360°). The dashed horizontal line indicates the mean probability.

will also respond on various time scales to a range of other phenomena such as variations in solar wind dynamic pressure [Slavin *et al.*, 1983; Arridge *et al.*, 2006], surface waves associated with the Kelvin-Helmholtz instability [Lepping *et al.*, 1981; Masters *et al.*, 2009], and magnetic reconnection [McAndrews *et al.*, 2008], all of which have previously been extensively studied at Earth (see e.g. the reviews by De Keyser *et al.* [2005] and Phan *et al.* [2005]), as well as, possibly, to variable mass loading of Saturn’s magnetodisc [Achilleos *et al.*, 2008]. We have therefore set relatively broad limits for inclusion in the data set, choosing to include successive like crossings of the boundary that lie between 0.4 and 1.6 of the magnetospheric period given by equation (6.5). We then test the extent to which such crossings are organized by the ‘Provan phase’ given by equation (6.1b).

For each boundary oscillation satisfying this criterion, a total of 92 over the data set as a whole, we then determine the Provan phase $\Psi_{Mc}(\varphi, t)$ (modulo 360°) at the centre of each magnetosphere re-entry as a proxy for the phase of maximum outward excursion of the boundary. We recall from the discussion in section 5.4 that this ‘centre phase’ is in general shifted relative to the phase of the maximum boundary excursion due to the motion of the spacecraft through the boundary region, to smaller phases outbound and to larger phases inbound. However, the results in Figure 5.4 show that the shift is typically only a few tens of degrees in the regime where observations of oscillations are reasonably probable. We will briefly examine in section 6.7 whether these anticipated phase shifts significantly affect the data set within the overall scatter of the data, and find no measureable effect.

In Figure 6.2 we show a histogram displaying the number of boundary oscillations in the data set versus the Provan phase (modulo 360°) at the centre of the oscillation (specifically the centre of the magnetosphere interval), divided into 30° bins of phase. Overall results are represented by the black line, showing that the magnetopause oscillation data are indeed highly organized by the Provan phase, with 88% of the oscillations occurring within the 180° phase range from 90° to 270° , and only 12% from 270° to 90° via 360° . The mean phase value is 160° , marked by the vertical black arrow in the figure, while the half-width at half maximum (HWHM) of the distribution is 75° . We note the consistency of this mean phase with the results of our preliminary study in section 6.3.1. The red line then shows the corresponding histogram for all oscillations occurring in episodes of 3 or more successive oscillations on a given pass i.e. $N \geq 3$ passes in the nomenclature of Chapter 5 (a total of 47 oscillations). Here an ‘episode’ is defined to be a sequence of crossings each with separations near the magnetospheric period, followed by a gap of at least one such period. The mean phase is 159° and the HWHM of the distribution is 45° , these not differing significantly from the overall values. Similarly, the green line shows the histogram for cases of only one oscillation observed during the boundary crossing i.e. $N = 1$ passes (a total of 35 oscillations). The mean phase of 156° and HWHM of 75° are again almost the same as the overall values, thus indicating that the boundary oscillations selected by the above algorithm, despite the wide timing criterion employed, represent an essentially homogenous set that is highly organized by the Provan phase, for both low and high numbers of boundary oscillations. More detailed examination (see section 7.4 in Chapter 7 below) shows that such organization of the oscillation phase data is present throughout the timing window between 0.4 and 1.6 of the magnetospheric

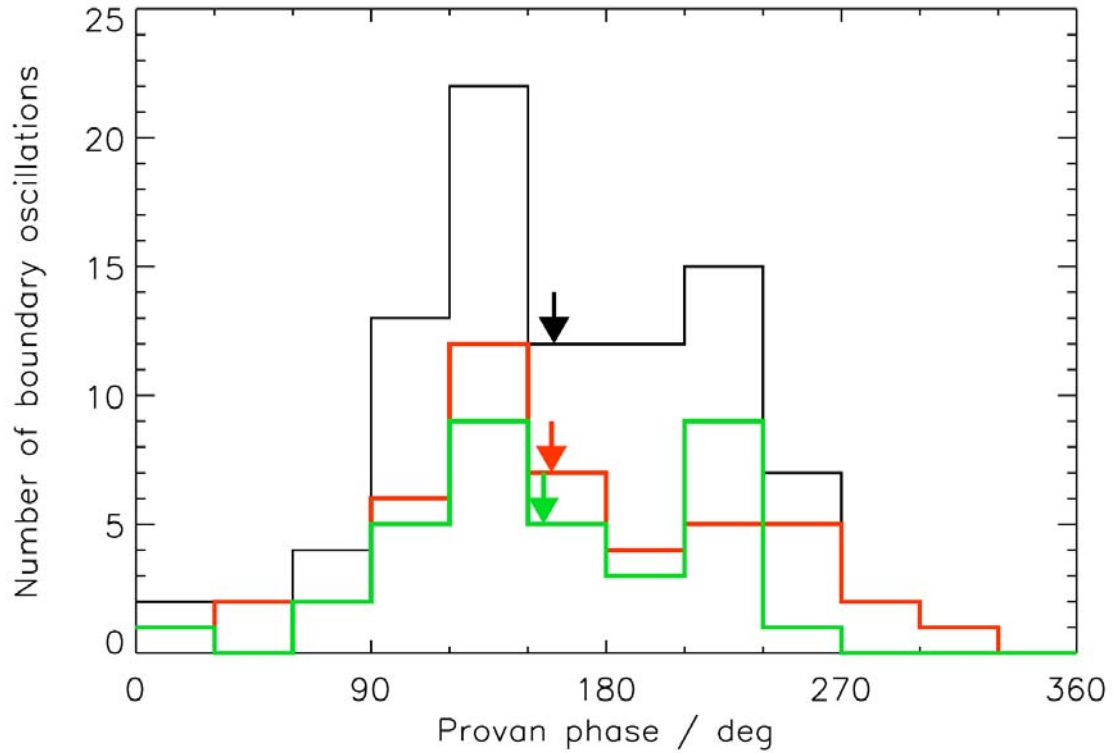


Figure 6.2 Histograms of the number of observed magnetopause oscillations versus the Provan phase (modulo 360°) at the centre of the magnetosphere interval of the oscillation. Overall results are shown by the black histogram, while the red histogram shows the results for all oscillations occurring in groups of 3 or more (i.e. $N \geq 3$ episodes), and the green histogram shows results for cases of a single oscillation ($N = 1$ episodes). Arrows with the same colour-coding mark the mean values of the Provan phase in each case.

period, though with the effect becoming somewhat less marked towards each end of the range.

The results in Figure 6.2 show that the re-entries selected within our timing window are well organized by the phase of the magnetic field oscillations within the ‘core’, and must therefore relate to boundary oscillations with a closely common period. It is evident, for example, that phase variations between the two phenomena exceeding $\pm 180^\circ$ over the interval of the study would completely destroy the effect observed, whether resulting from short-term ‘phase jitter’ (due e.g. to the effect of other boundary phenomena), or to longer-term phase drifts due to differences in the oscillation periods. Simple consideration of the latter effect then shows that the period of the boundary oscillations must match that of the interior field oscillations to better than ~ 20 s over the 3.5 year interval of the study in order to yield the above result. With a difference in the period of this magnitude ($\sim 0.05\%$ of the total period) or greater, the two oscillations would have varied between fully in phase to fully out of phase and back over the course of the interval, thus yielding a null result. The phase results in Figure 6.2 thus prove that the boundary oscillations must occur at essentially the same period as the interior field oscillations throughout the interval of the study, within the above narrowly-defined limit.

With regard to the mean phase values in Figure 6.2, we note from equation (6.2) that they imply that at the times of maximum outward boundary excursions the rotating equatorial field in the ‘core’ points at angle $\varphi_M \approx 160^\circ + \varphi_S$ anti-clockwise from the Sun as viewed from the north, where φ_S is the azimuth of the spacecraft. That is, the equatorial ‘core’ field points $\sim 160^\circ$ anti-clockwise of the radial vector to the outwardly-displaced boundary as viewed from the north i.e. approximately away from the boundary at these

times. Since oscillations in the θ field component are approximately in phase with those in the r component within the ‘core’, we can also say that maximum outward boundary excursions occur $\sim 160^\circ$ of phase behind maxima in the θ field component in the ‘core’ at the azimuth of the spacecraft, or equivalently $\sim 20^\circ$ of phase ahead of θ component minima. The relation of the boundary oscillations to the internal field oscillations will be examined further in section 6.7.

6.4 Examples of Magnetopause Boundary Oscillations

Three representative examples showing the magnetopause oscillations are presented in Figures 6.3-6.5. The top panel in each figure shows an electron count rate spectrogram colour-coded according to the scale on the right. The four panels below show 1 min averaged values of the spherical polar radial (r), colatitudinal (θ), and azimuthal (φ) components of the magnetic field referenced to the planet’s spin/magnetic axis, together with the magnitude of the field. The bottom panel shows the Provan phase $\Psi_{Mc}(\varphi, t)$, modulo 360° , the line being colour-coded according to whether the spacecraft is in the magnetosphere (red), or the magnetosheath or solar wind (blue). Vertical dashed lines mark the centre of the magnetosphere intervals during oscillation episodes, while the red stars in the bottom panel indicate the corresponding Provan phase as employed in the histogram in Figure 6.2. At the bottom of the plots we provide spacecraft positional information, specifically LT, colatitude (again with respect to the spin/magnetic axis), and radial distance from the planet’s centre.

Figure 6.3 shows 4 days of data (days 280.75 to 284.75 of 2005) from Rev 16 inbound, which we present here as an example of a $N = 2$ pass. During this interval the

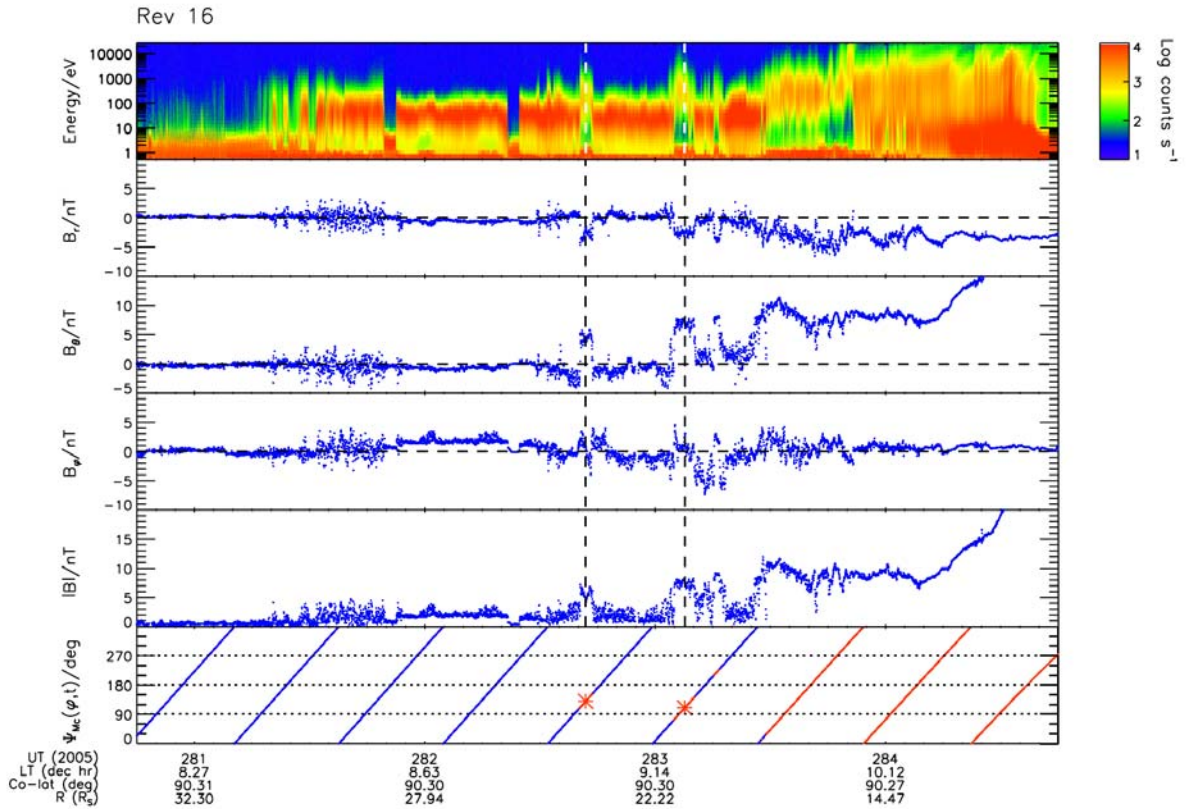


Figure 6.3 Example of a $N = 2$ pass, showing 4 days of data from Rev 16 inbound. The top panel shows an electron count rate spectrogram from anode 5 of the ELS instrument. The next four panels show 1 min averaged values of the spherical polar radial (r), colatitudinal (θ), and azimuthal (φ) components of the magnetic field referenced to the planet's spin/magnetic axis, together with the magnitude of the field. The bottom panel shows the Provan phase $\Psi_{Mc}(\varphi, t)$ modulo 360° , the line being colour-coded according to whether the spacecraft is in the magnetosphere (red), or the magnetosheath or solar wind (blue). Vertical dashed lines mark the centre of the magnetosphere intervals during oscillation episodes, while the red stars in the bottom panel indicate the corresponding Provan phase as employed in the histogram in Figure 6.2. Spacecraft positional information is provided at the bottom of the plot.

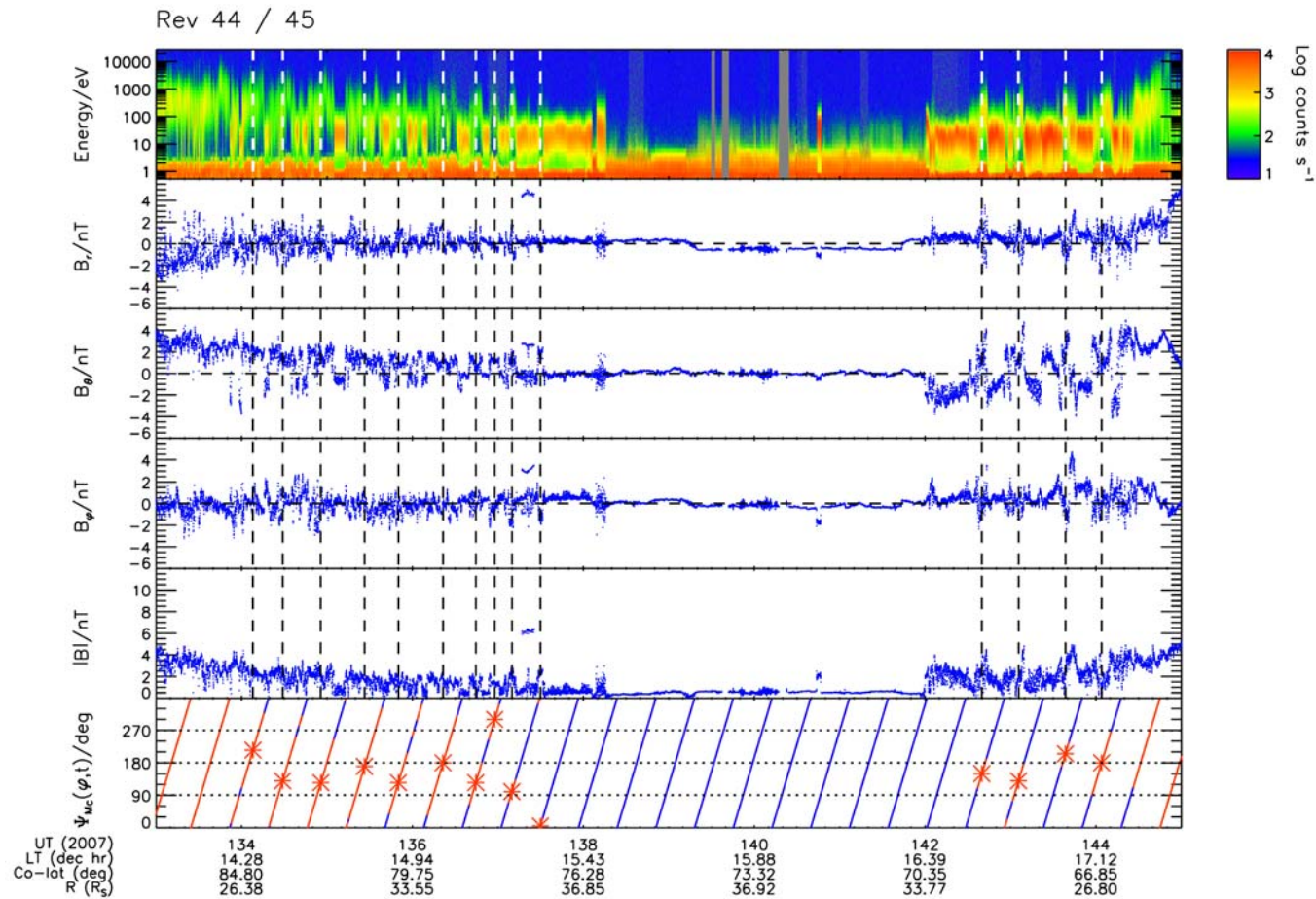


Figure 6.4 The figure shows 12 days of data from the apoapsis interval of Rev 44/45 in the same format as Figure 6.3. This orbit, with a $N=10$ outbound pass and a $N=4$ inbound pass, exhibits the largest number of magnetospheric period magnetopause oscillations observed in the data set examined (though we note the scattered phase values of the last three oscillations outbound).

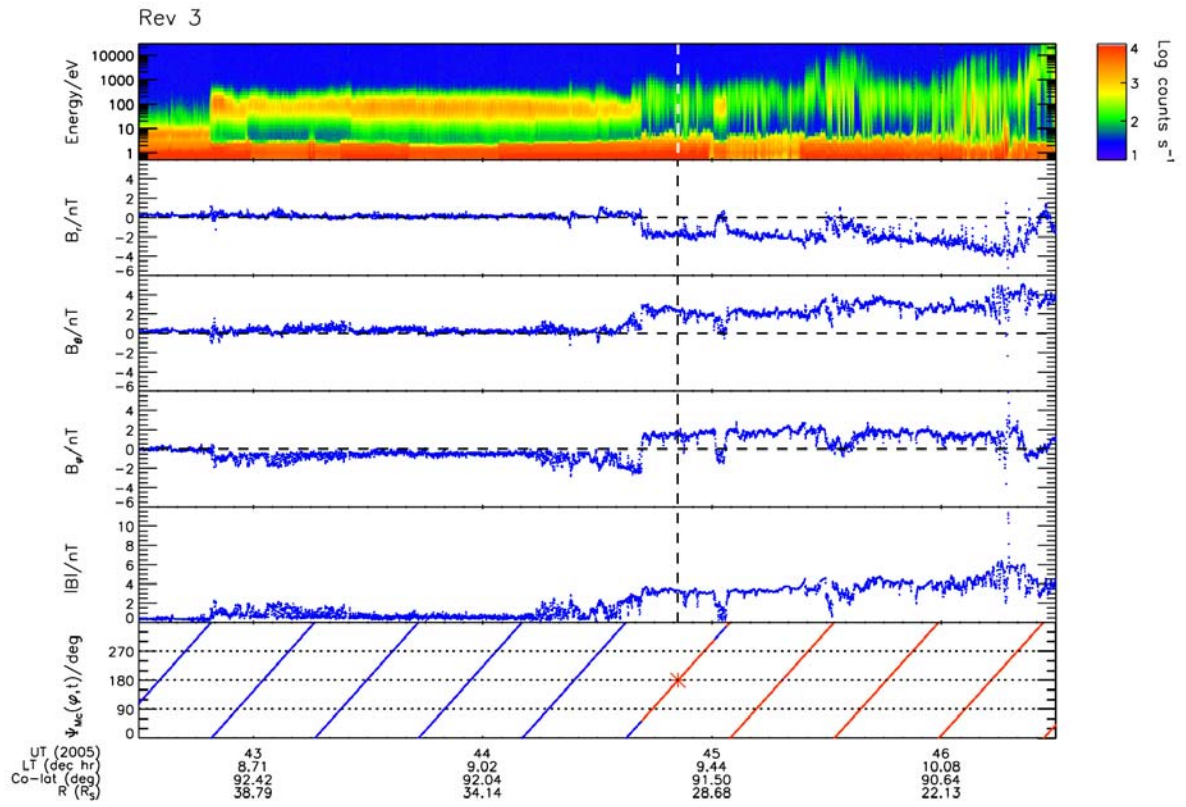


Figure 6.5 Example of a $N = 1$ pass, showing 4 days of data from Rev 3 inbound in the same format as Figure 6.3.

spacecraft is located in the equatorial mid-morning LT sector, at radial distances ranging from $\sim 34 R_S$ to $\sim 9 R_S$. The spacecraft passes from the solar wind, an environment characterized by magnetic field strengths of $\sim 0.5\text{--}1.0$ nT and low electron fluxes at energies above ~ 10 eV (the large fluxes below ~ 10 eV in this case are largely spacecraft photoelectrons), into the magnetosheath, characterized by increased field strengths and a substantially higher electron flux at energies in the $10\text{--}100$ eV range, at ~ 08 h UT on day 281. There follow multiple transitions between the two regimes. The first crossing of the magnetopause into the magnetosphere occurs at ~ 16 h UT on day 282, the transition being marked by an increase in the field strength, a change to a southward orientation (B_θ positive), and a reduction in variability, and by a reduction in the electron flux in the ~ 10 to 100 eV range and an increase at ~ 100 eV to ~ 1 keV. The occurrence of this magnetosphere interval and the one that follows it, the centres of which are marked by the vertical dashed lines, is indicative of magnetospheric period magnetopause oscillations. Note the consistency in the Provan phases shown by the stars, at 130° and 110° respectively, values that contribute to the histogram peaks in Figure 6.2. Note also the presence of subsidiary short-lived magnetosphere encounters that are not part of the oscillation sequence, which are presumably due either to solar wind variations or to other boundary motions associated e.g. with Kelvin-Helmholtz waves. The presence of such effects will inevitably alter the timings of boundary crossings more generally, thus no doubt contributing to the significant scatter in the phase values in Figure 6.2.

The second example in Figure 6.4 exhibits the largest number of magnetospheric period magnetopause oscillations observed in the data set examined. The figure shows 12 days of data (days 133 to 144 of 2007) from the apoapsis interval of Revs 44 / 45, during

which time the spacecraft is located within $\sim 25^\circ$ of the equator in the post-noon to dusk LT sector, and spans radial distances from $\sim 24 R_S$ at the beginning of the interval, to $\sim 37 R_S$ at apoapsis, and back to $\sim 24 R_S$ at the end. The spacecraft thus passes from the magnetosphere to the solar wind, and back to the magnetosphere again during the interval shown. Multiple magnetopause crossings near the magnetospheric period are observed both outbound and inbound as marked by the vertical dashed lines, with 10 outbound boundary oscillations satisfying our timing criterion, and 4 inbound. The phasing of these oscillations shown by the stars in the lower panel is generally consistent with each other, and with the peak in the histogram shown in Figure 6.2, except for the last three oscillations outbound that are somewhat scattered, presumably due to short-term boundary motions as mentioned above. All of these oscillations are, however, included in the histogram.

Figure 6.5 by contrast, presents a more typical $N=1$ example. It shows 4 days of data from the inbound pass of Rev 3, during which the spacecraft is located in the equatorial mid-morning LT sector at radial distances ranging from $\sim 41 R_S$ to $\sim 18 R_S$. The spacecraft passes from the solar wind across the magnetosheath into the magnetosphere, with one oscillation of the magnetopause being observed, with a centre phase of 180° .

6.5 Occurrence of Magnetopause Oscillations in Cassini Boundary Data

Overall results on boundary oscillations observed by Cassini are shown in Table 6.1. The first two columns give the Rev number and pass type, inbound, outbound, or ‘grazing’, spanning Revs SOI-Rev 23 and Revs 38-55 (the spacecraft being in the tail exclusively for Revs 24-37). A ‘grazing’ pass indicates that there was no full passage from magnetosphere

Table 6.1 Number of magnetopause oscillations observed on each pass together with spacecraft position, oscillation layer width, and normal velocity data. Continued on the next two pages.

| Rev | Pass ^a | Number of oscillations ^b | Radial distance ^c R _S | Local time hours | KSM latitude deg | Width of oscillating layer ^d R _S | Normal velocity ^e km s ⁻¹ |
|---------|-------------------|-------------------------------------|--|---------------------|---------------------|---|--|
| SOI | in | 1 | 33.6 | 7.7 | -3.6 | 2.8 | -6.8 |
| | out | DG | | | | | |
| A | in | 0 | 22.5 | 10.2 | 19.0 | | -4.8 |
| | out | 1 | 46.1 | 4.7 | -20.3 | 1.1 | 3.3 |
| B | in | 0 | 22.5 | 10.2 | 19.0 | | -4.6 |
| | out | 0 | 44.9 | 5.9 | -5.2 | | 2.8 |
| C | in | DG | | | | | |
| | out | 0 | 44.7 | 5.8 | -6.0 | | 2.8 |
| 3 | in | 1 | 29.6 | 9.4 | 15.7 | 1.8 | -3.3 |
| 3 / 4 | out | 0 | 41.3 | 7.2 | 6.9 | | 1.9 |
| | in | 1 | 24.9 | 9.8 | 18.5 | 1.1 | -3.6 |
| 4 / 5 | out | 0 | 32.5 | 6.4 | 2.5 | | 3.5 |
| | in | 1 | 20.8 | 10.2 | 19.4 | 1.3 | -4.4 |
| 5 / 6 | out | 0 | 33.3 | 8.0 | 6.2 | | -1.2 |
| | in | 0 | 19.1 | 9.3 | 10.2 | | -4.3 |
| 6 / 7 | out | 1 | 28.5 | 6.0 | -3.8 | 3.0 | 4.0 |
| | in | 1 | 25.5 | 9.3 | -2.0 | 0.9 | -3.1 |
| 7 / 8 | out | 1 | 31.5 | 6.3 | -3.8 | 2.5 | 3.4 |
| | in | 0 | 29.1 | 9.0 | -2.6 | | -2.4 |
| 8 / 9 | out | 1 | 32.5 | 6.3 | -4.1 | 1.9 | 3.2 |
| | in | 0 | 20.5 | 9.8 | -2.2 | | -4.1 |
| 9 / 10 | out | 1, 1 | 38.9, 40.4 | 6.9, 7.2 | -4.4, -4.3 | 0.7, 0.6 | 1.8, 1.1 |
| | in | 0 | 22.5 | 9.6 | -2.7 | | -3.7 |
| 10 / 11 | out | DG | | | | | |
| | in | 1 | 20.2 | 9.9 | -2.7 | 2.4 | -4.4 |
| 11 / 12 | out | 1 | 31.6 | 6.1 | -5.2 | 0.9 | 3.6 |
| | in | 0 | 25.7 | 9.2 | -3.7 | | -3.0 |
| 12 / 13 | out | 0 | 32.1 | 6.1 | -5.5 | | 3.3 |
| | in | 0 | 27.7 | 8.9 | -4.2 | | -2.6 |
| 13 / 14 | out | 0 | 34.6 | 6.3 | -3.7 | | 2.3 |
| | in | 1 | 19.8 | 9.0 | 0.7 | 2.7 | -4.0 |
| 14 / 15 | out | DG | | | | | |
| | in | DG | | | | | |
| 15 / 16 | out | 2, 3 | 39.8, 41.2 | 6.8, 7.2 | 3.6, 5.6 | 2.0, 1.3 | 1.5, 0.7 |
| | in | 2 | 22.3 | 9.2 | 14.3 | 4.4 | -3.7 |
| 16 / 17 | out | 1 | 29.9 | 5.8 | -1.2 | 2.8 | 3.6 |
| | in | 1 | 30.1 | 8.4 | 11.2 | 1.1 | -2.2 |
| 17 / 18 | out | 0 | 37.3 | 4.6 | -7.2 | | 3.4 |
| | in | 0 | 45.7 | 7.2 | 5.6 | | -1.0 |

| | | | | | | | |
|---------|---------|---------|------------------|---------------|-----------------------|----------|-----------------|
| 18 / 19 | grazing | 1, 1 | 36.8, 44.7 | 4.5, 5.1 | -7.2, -4.7 | | 3.4, 2.5 |
| 19 / 20 | out | 0 | 43.2 | 5.0 | -5.2 | | 2.2 |
| | in | 1 | 46.1 | 6.2 | 0.9 | 0.0 | 0.0 |
| 20 / 21 | grazing | 1, 1, 1 | 64.5, 67.1, 67.9 | 4.2, 4.5, 4.6 | -8.4, -7.2, -6.6 | | 1.5, 1.2, 1.0 |
| 21 / 22 | grazing | 3, 3, 1 | 44.7, 37.2, 29.3 | 4.4, 5.0, 5.6 | -7.4, -4.8, -2.1 | | 0.1, -0.8, -1.7 |
| 22 / 23 | out | 0 | 68.2 | 2.9 | -12.7 | | 0.8 |
| | in | 3 | 62.6 | 3.5 | -10.8 | 0.4 | 0.2 |
| 38 / 39 | grazing | 6 | 17.8 | 12.8 | -36 – 17 ^f | | 1.2 |
| 39 / 40 | out | NC | | | | | |
| | in | NC | | | | | |
| 40 / 41 | out | 1 | 26.2 | 14.9 | 32.4 | 0.7 | 0.5 |
| | in | 0 | 30.4 | 17.6 | 50.7 | | -2.2 |
| 41 / 42 | grazing | 1 | 32.4 | 15.9 | 40.1 | | -0.7 |
| 42 / 43 | grazing | 1, 1 | 27.1, 33.1 | 14.6, 15.4 | 23.3, 32.0 | | 1.7, 0.1 |
| 43 / 44 | out | 0 | 21.1 | 13.8 | 13.2 | | 3.5 |
| | in | 4 | 35.8 | 16.1 | 31.2 | 2.8 | -1.4 |
| 44 / 45 | out | 10 | 32.9 | 14.9 | 18.8 | 7.3 | 1.2 |
| | in | 4 | 29.3 | 16.9 | 25.1 | 9.2 | -3.4 |
| 45 / 46 | out | 0 | 24.7 | 14.1 | 12.9 | | 3.2 |
| | in | 4 | 33.5 | 16.3 | 17.1 | 6.7 | -2.5 |
| 46 / 47 | out | 1 | 19.8 | 13.6 | 11.0 | 3.9 | 4.7 |
| | grazing | 1 | 37.5 | 15.3 | 8.7 | | 0.2 |
| | in | 1 | 29.3 | 16.6 | 5.7 | 2.8 | -3.4 |
| 47 / 48 | out | 4, 2 | 28.7, 39.9 | 14.4, 15.3 | 9.4, 7.7 | 7.4, 1.5 | 3.1, 1.5 |
| | in | 0 | 39.3 | 17.2 | 2.5 | | -2.7 |
| 48 / 49 | out | 1 | 25.9 | 12.3 | 11.4 | 2.2 | 4.6 |
| | in | 0 | 28.6 | 17.9 | 0.7 | | -5.2 |
| 49 / 50 | out | 1 | 31.3 | 12.7 | 8.8 | 1.4 | 3.7 |
| | in | 1 | 42.2 | 16.2 | -1.2 | 1.9 | -3.2 |
| 50 / 51 | out | DG | | | | | |
| | in | DG | | | | | |
| 51 / 52 | out | 2 | 30.5 | 12.4 | 10.8 | 5.2 | 3.5 |
| | in | 1 | 38.9 | 15.3 | 10.3 | 2.5 | -2.8 |
| 52 / 53 | out | 3 | 31.4 | 12.4 | 12.5 | 3.9 | 2.3 |
| | in | 0 | 21.3 | 15.2 | 16.5 | | -5.2 |
| 53 / 54 | out | 1 | 24.5 | 11.8 | 12.3 | 2.5 | 3.8 |
| | in | DG | | | | | |
| 54 / 55 | out | 2 | 22.0 | 11.6 | 11.5 | 5.4 | 4.1 |
| | in | 0 | 32.9 | 14.3 | 35.4 | | -2.3 |

^a A ‘grazing’ pass indicates that there is no full passage from magnetosphere to magnetosheath or vice versa.

^b Two or more numbers are given when there is more than one separate episode of boundary oscillations observed on a given pass; NC indicates no contact with the boundary

on the pass; DG indicates that data from the pass cannot be employed in the study due to one or more significant data gaps.

^c Positional data indicate values at the centre of the magnetosphere interval in the case of one oscillation in a given episode; in the case of more than one oscillation in an episode, an average is given over the values at the centres of the individual magnetosphere intervals. Where no oscillations are observed during a pass, positional data is given for the time of the single magnetopause crossing if only one took place, and for the time halfway between the first and last crossings in the case of multiple crossings.

^d The displacement of the spacecraft perpendicular to the magnetopause between the first and last crossings of each oscillation episode. Values are provided for all episodes from non-‘grazing’ passes.

^e Computed using the *Arridge et al.* [2006] magnetopause model at the centre of the magnetosphere interval in the case of single oscillation episodes; where there is more than one oscillation in an episode, an average is given over the velocities at the centres of the individual magnetosphere intervals. Where no oscillations are observed during a pass, the normal velocity is computed for the time of the single magnetopause crossing if only one took place, and for the time halfway between the first and last crossings in the case of multiple crossings.

^f A single representative value is inappropriate here since the range (as given) is so large.

to magnetosheath or vice versa on that pass. In the third column we then show the number of boundary oscillations N observed on each pass that satisfied the timing criterion. Occasionally on a given pass the spacecraft observed more than one episode of boundary oscillations, separated by at least one oscillation period, in which case they are recorded separately in this column. Passes which could not be used due to prolonged or cumulative data gaps are indicated by ‘DG’, while ‘NC’ indicates passes during which there was no contact with the magnetopause. Columns four to six in the table record the position of the spacecraft at the centre of the magnetopause oscillation interval on that pass (defined in table footnote ‘c’ according to circumstance), giving the radial distance (R_S), the LT (h), and the KSM latitude (deg), respectively. (KSM coordinates are defined in section 6.6 below.) Column seven shows the width of the oscillation layer i.e. the spacecraft’s displacement normal to the magnetopause between the first and last crossings of each non-‘grazing’ oscillation episode, estimated using the normal to the *Arridge et al.* [2006] model boundary that passes through the centre point given in the previous columns, details of which are discussed in section 6.8 below. Column eight of Table 6.1 finally shows the spacecraft velocity normal to the magnetopause, positive outwards, also estimated from the *Arridge et al.* [2006] model.

The distribution of the number of oscillations observed on each non-‘grazing’ pass is shown in the histogram in Figure 6.6, taken from the third column of Table 6.1. Here we plot the number of passes versus the number of observed oscillations on the pass, the latter for this purpose being summed over all oscillation episodes on the pass if there is more than one. The histogram shows that 43% (26 of 61) of all eligible passes exhibit no oscillations near the magnetospheric period, as identified here, 38% exhibit one oscillation, 7% two

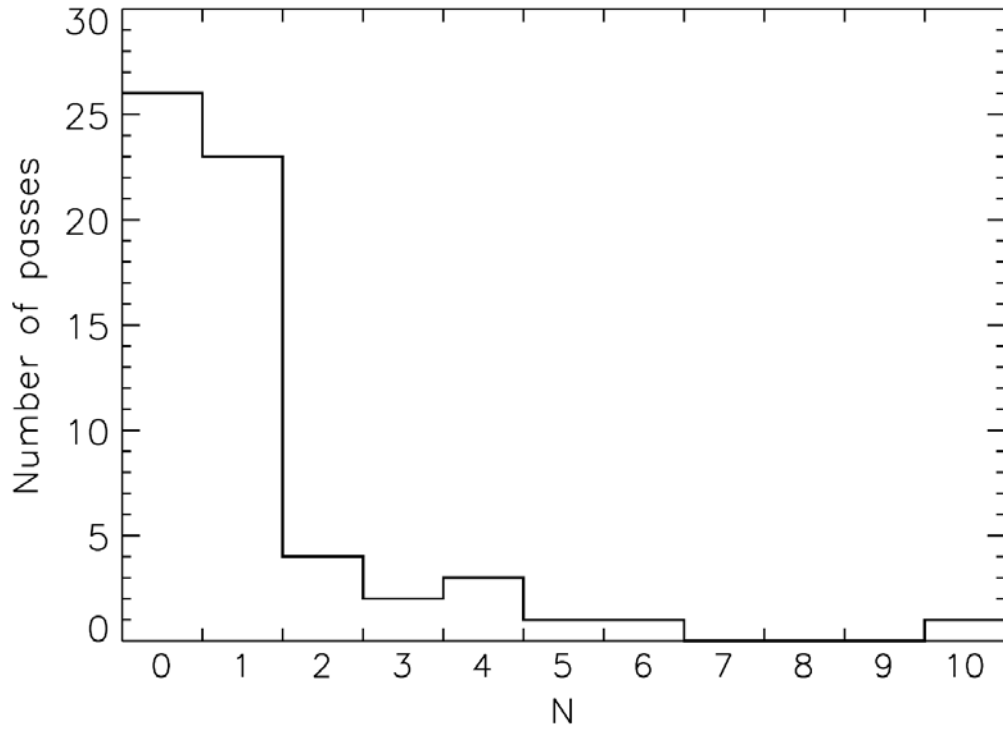


Figure 6.6 Histogram showing the number of passes versus the number of oscillations N observed on the pass. ‘Grazing’ passes, during which there is no full passage from magnetosphere to magnetosheath or vice versa, are excluded. The number of oscillations is summed over all episodes on a pass if there is more than one episode.

oscillations, and 12% three or more. Taken as a whole, these results show that such oscillations are common in the Cassini data set, with 57% of passes showing one or more oscillations, though large numbers of multiple crossings are relatively rare. These results will be discussed further in section 6.8 in relation to the speed and amplitude of the boundary.

6.6 Spatial Coverage of Magnetopause Oscillation Observations

In Figure 6.7 we show the overall spatial distribution of the intervals containing magnetopause oscillations. Here the grey short-dashed lines in panels (a) to (c) show the trajectory of the spacecraft for Revs SOI to 55 inbound, projected onto each of the three principal planes in KSM coordinates. The KSM system is the most appropriate for magnetopause studies, with the X -axis pointing from the planet's centre towards the Sun, approximately opposite to the solar wind flow direction, the X - Z plane containing the co-aligned spin and magnetic axes of the planet, while Y completes the right-handed set. Panels (a) to (c) thus show the trajectory projected onto the X - Y , X - Z , and Y - Z planes, respectively. In panels (a) and (b) we also show the magnetopause model of *Arridge et al.* [2006] (blue dashed lines) and the bow shock model of *Masters et al.* [2008] (green dashed lines), modelled as figures of revolution about the KSM X -axis, in the equatorial and noon-midnight meridians respectively. The outer and inner lines correspond to solar wind dynamic pressures of 0.01 and 0.1 nPa, respectively, spanning the usual range at Saturn. Intervals containing observations of magnetopause oscillations are shown by the red segments along the spacecraft trajectory. These specifically show the whole of each 0° – 360° rotation of Provan phase containing an observed oscillation, so that each

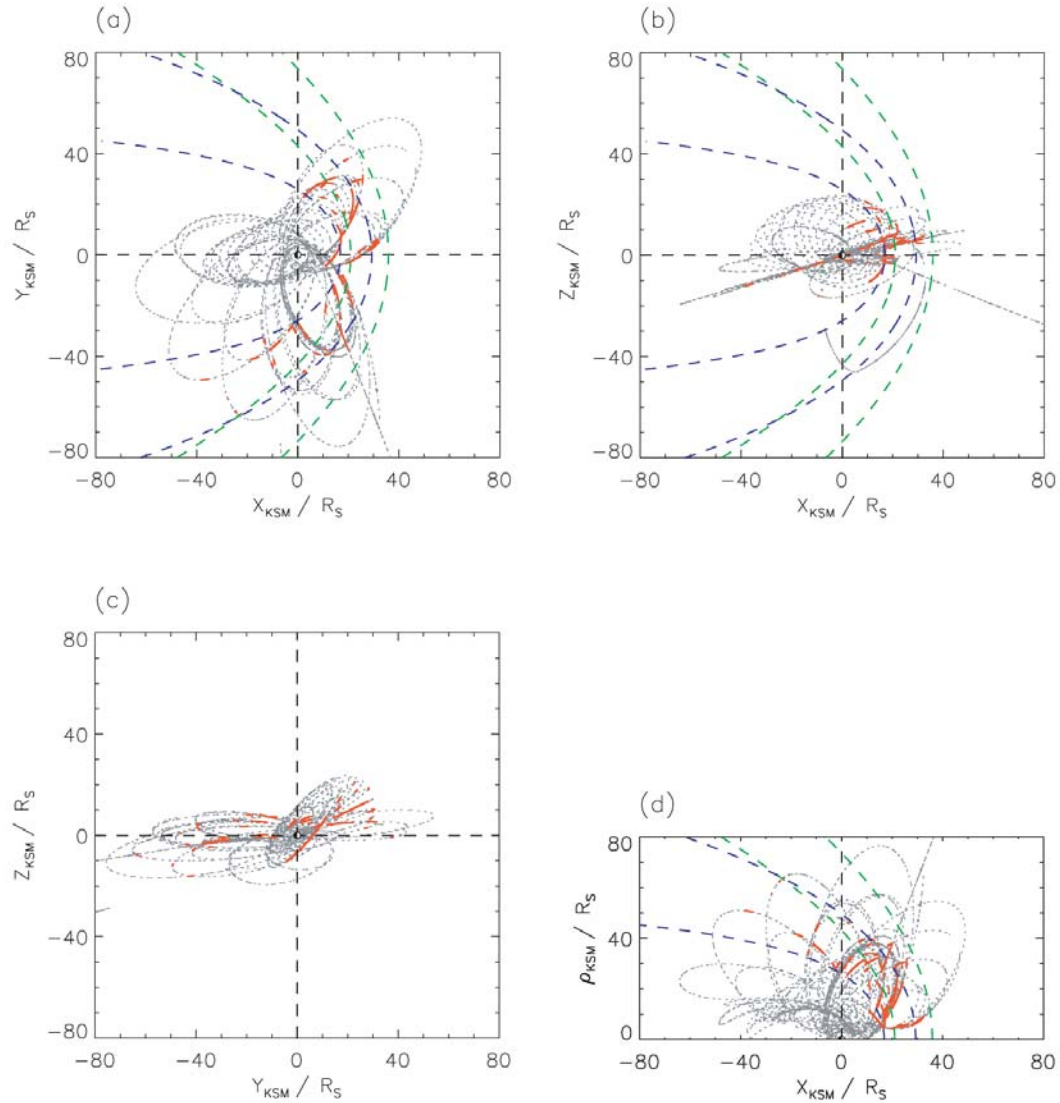


Figure 6.7 Plots showing the overall spatial distribution of intervals containing magnetopause oscillations. The grey short-dashed lines show the trajectory of the spacecraft for Revs SOI to 55 inbound. Panels (a), (b) and (d) also show the magnetopause model of Arridge *et al.* [2006] (blue dashed lines) and the bow shock model of Masters *et al.* [2008] (green dashed lines), the outer of each pair of lines corresponding to a solar wind dynamic pressure of 0.01 nPa, and the inner to 0.1 nPa, spanning the usual range. Intervals containing observations of magnetopause oscillations are shown by the red segments along the spacecraft trajectory.

‘episode’ containing more than one oscillation on a given pass is shown by a continuous red line. It can be seen that oscillations are observed over the whole range of LTs spanned by the spacecraft trajectory when it intersected the magnetopause, extending from ~ 3.5 h LT in the pre-dawn sector to ~ 17 h LT at dusk, and also over a range of (KSM) latitudes in the noon and post-noon sector extending from -36° in the south to 40° in the north. We thus conclude that boundary oscillations near the magnetospheric period are a spatially widespread phenomenon. They are also observed over a broad range of radial distances spanning the whole region between the two model magnetopause boundaries, thus suggesting they are observed over the whole range of solar wind dynamic pressure conditions that determine the size of the magnetosphere. To see this free from the trajectory projection effects that are present in panels (a) to (c), in panel (d) we show the spacecraft trajectory, model boundaries, and magnetopause oscillation intervals in cylindrical X - ρ coordinates, where $\rho = \sqrt{Y^2 + Z^2}$, noting again that the model boundaries are figures of revolution about the KSM X -axis. This figure clearly shows that the boundary oscillation intervals span the whole region between the model magnetopause surfaces that correspond to the usual range of solar wind dynamic pressure.

6.7 Magnetopause Boundary Oscillation Phase

We now continue the analysis of section 6.3 examining the phase of the boundary oscillations relative to those of the magnetic field oscillations within the magnetosphere. We begin by examining whether the Provan phase of the oscillation varies with position on the boundary. We note at the outset that due to the strong correlation between the radial distance and LT of the boundary encounters evident in Figure 6.7, it is not possible to

clearly separate individual dependencies on these two spatial parameters. In Figures 6.8a and 6.8b we thus plot the Provan phase of each oscillation (stars) versus radial distance and LT, respectively. Despite the large scatter in the phase values previously noted, the data provide evidence for the presence of positional variations, with the phase increasing with radial distance, and decreasing with LT from dawn to noon, while increasing again between noon and dusk. These variations have been made a little more apparent in these figures by the addition of open squares, which show the averaged phase and position in 10 R_S bins of radius in Figure 6.8a (10-20, 20-30 R_S , and so on), and in 3 h bins of LT in Figure 6.8b (3-6, 6-9 h, and so on). The non-monotonic behaviour about noon compared with the near-monotonic behaviour with radius suggests that the principal effect could be with radius, due to outward propagation of the corresponding magnetospheric oscillation with finite speed from the inner magnetosphere. On this basis we have made a linear least-squares fit to the phase data versus radius in Figure 6.8a such that the oscillation Provan phase is represented by $\psi'(r/R_S) + \psi_0$, where ψ' is the phase slope, r the radial distance, and ψ_0 the intercept at zero radius, resulting in values of $\psi' = 2.1 \pm 0.6 \text{ deg } R_S^{-1}$, and $\psi_0 = 89 \pm 20 \text{ deg}$, as shown by the straight line in the figure. We note, however, that the correlation coefficient is only 0.37, meaning that only 14% of the data variation is explained by this radial dependency. The outward propagation speed corresponding to the slope is given by

$$v_r = \frac{360R_S}{\tau_M \psi'} \quad , \quad (6.6)$$

where $R_S = 60,268 \text{ km}$ is Saturn's radius, τ_M is the oscillation period given by equation (6.5) in seconds, and ψ' is the phase slope in $\text{deg } R_S^{-1}$. Substituting $\tau_M = 10.8 \text{ h}$ as a representative value (varying only between 10.77 and 10.83 h during the whole

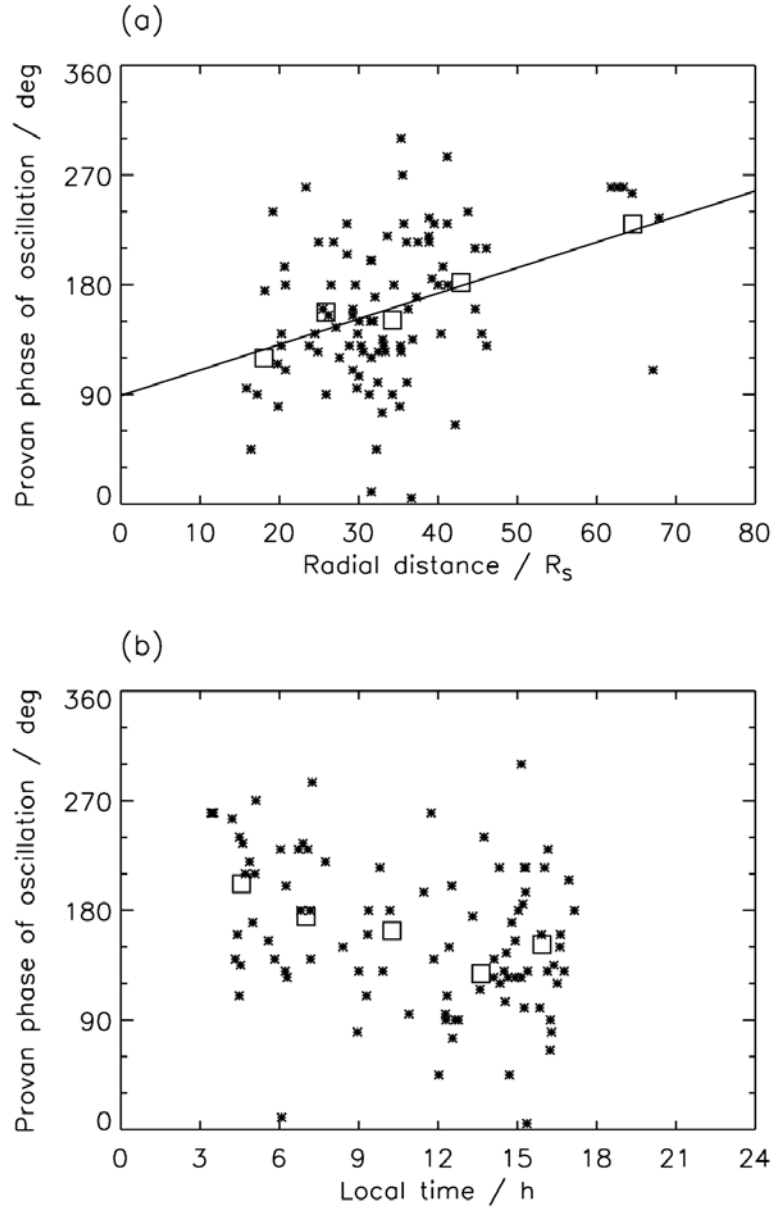


Figure 6.8 Plot of the Provan phase (modulo 360°) of each observed oscillation versus (a) radial distance and (b) LT. The open squares show the averaged phase and position in 10 R_S bins of radius (10-20, 20-30 R_S , and so on) in panel (a), and in 3 h bins of LT (3-6, 6-9 h, and so on) in panel (b). The straight line in panel (a) represents a least-squares fit to the phase data versus radius with a phase slope of $\psi' = 2.1 \pm 0.6 \text{ deg } R_S^{-1}$, and an intercept at zero radius of $89 \pm 20 \text{ deg}$.

interval) and $\psi' = 2.1 \text{ deg R}_S^{-1}$ yields a value of $270 \pm 80 \text{ km s}^{-1}$. Although detailed profiles of characteristic phase speeds in the near-equatorial plasma have yet to be published for Saturn's magnetosphere, we note that values of the Alfvén speed and sound speed suggested by the plasma bulk parameters presented by *Wilson et al.* [2008] and *McAndrews et al.* [2009] are of this order.

The variation in phase of the equatorial magnetic field oscillations with radius and azimuth within Saturn's magnetosphere has recently been investigated by *Andrews et al.* [2010]. In their study the band-pass filtered residual magnetic field data are binned in radius and LT, and fitted to a function

$$B_i(r, \varphi, t) = B_{i_0}(r, \varphi) \cos(\Psi_{Mc}(\varphi, t) - \psi_i^*(r, \varphi)) \quad , \quad (6.7)$$

where $\Psi_{Mc}(\varphi, t)$ is the 'core' Provan phase given by equations (6.1b) and (6.4), thus determining for field component i the radial and LT variations of both the oscillation amplitude B_{i_0} and the phase ψ_i^* relative to the 'core' (compare equation (6.7) with equation (6.1a)). The most appropriate field component for study in the present context is the θ component, directed parallel to the planetary field in the equatorial plane and thus related to changes in magnetic pressure within the 'core' region, which is also found to have a relatively simple phase behaviour with radial distance. In the study presented by *Andrews et al.* [2010] the phases were determined to a radial distance of 30 R_S , which we extend here as data availability allows to 50 R_S , thus covering most of the radial range encompassed by the magnetopause data (see Figure 6.8a). We also consider the LT range from 03 to 18 h (see Figure 6.8b). For the present study the θ field data have been binned into 5 R_S bins of radius and 3 h bins of LT, with results shown in Figure 6.9a. Here we plot

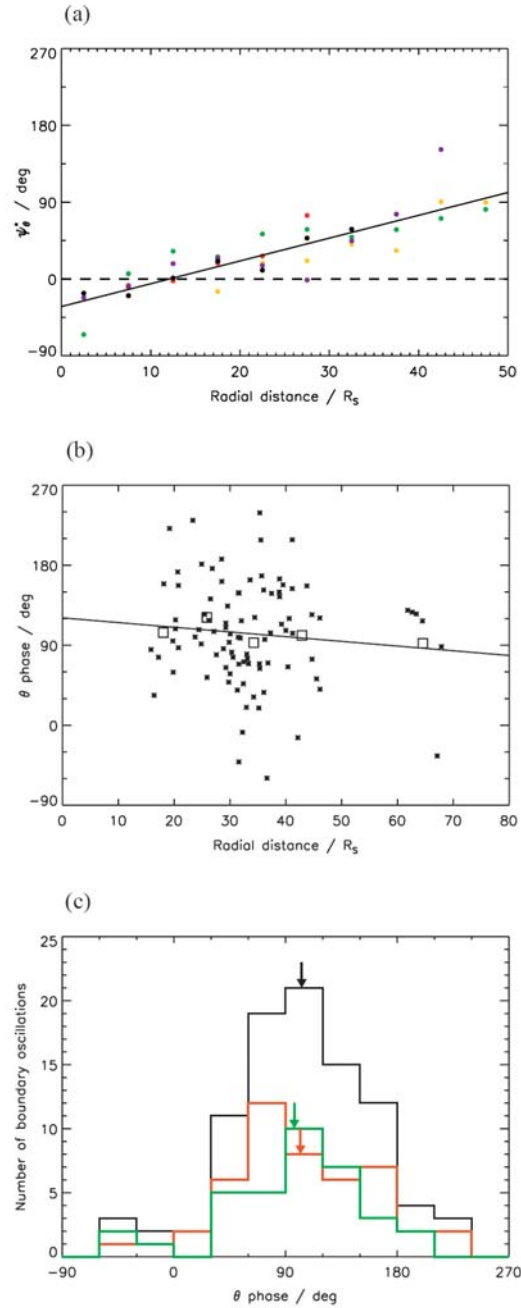


Figure 6.9 (a) Plot of the phase of the oscillations in the θ component of the magnetic field in the equatorial region relative to the Provan phase ψ_{θ}^* , versus radius. (b) Plot of the θ phase at the centre of the magnetosphere interval of each observed magnetopause oscillation, plotted versus radial distance. (c) Histograms of the number of observed oscillations versus θ phase.

the phase ψ_θ^* versus radius, with green, yellow, red, purple, and black data points corresponding to 03-06, 06-09, 09-12, 12-15, and 15-18 h LT, respectively. It can be seen that ψ_θ^* generally increases with radius from near-zero values in the inner region, consistent with the Provan phase model given by equation (6.1), to $\sim 90^\circ$ at $\sim 50 R_S$. There is little apparent systematic variation with LT over the range, within the scatter of the data. It thus seems reasonable simply to fit a least-squares straight line to these data, so that over the above regime the phase of the θ field component oscillations is given by

$$\Psi_\theta(r, \varphi, t) = \Psi_{Mc}(\varphi, t) - \psi_\theta^* = \Phi_M(t) - \varphi - \left(a \left(\frac{r}{R_S} \right) + b \right), \quad (6.8)$$

where from the linear fit $a = 2.63 \pm 0.25 \text{ deg } R_S^{-1}$, and $b = -31.8 \pm 6.7 \text{ deg}$. We note that this slope is close, within errors, to the slope of the linear fit to the magnetopause phase data in Figure 6.8a, and if again interpreted in terms of the effect of outward radial propagation via equation (6.6), yields a propagation speed of $210 \pm 20 \text{ km s}^{-1}$, consistent within errors with the radial speed deduced from the magnetopause phase data. Using equation (6.8) we can now determine the phase of the magnetopause oscillations relative to the θ field component at the radius of the boundary, in effect by subtracting the appropriate value of $\psi_\theta^*(r)$ from the Provan phase value shown in Figure 6.8a. The results are shown in Figure 6.9b in the same format as Figure 6.8a, from which we can see that the radial dependency evident in the latter figure has now in essence been removed. A linear least-squares fit gives a slope of $-0.53 \pm 0.56 \text{ deg } R_S^{-1}$ (this being consistent with zero) and an intercept of $121 \pm 20 \text{ deg}$, with a correlation coefficient of only 0.10.

In Figure 6.9c we plot histograms of the number of boundary oscillations versus the ‘ θ phase’ given by equation (6.8) in the same format as Figure 6.2, except now over the range from -90° to 270° on the horizontal axis. For the overall distribution shown by the black line, the mean phase is 103° (shown by the black vertical arrow in the figure) with a HWHM of 75° . We also see that 82 of the 92 phase values (89%) lie within the most ‘popular’ 180° phase sector between 30° and 210° , so that the magnetopause oscillations may be regarded as being very well organized by the θ phase i.e. by the phase of the compressional field component at the radial distance of the magnetopause. The histograms corresponding to $N=1$ and $N \geq 3$ episodes, shown by the green and red lines (as in Figure 6.2), respectively, exhibit essentially similar behaviour. Recalling that the phases shown in Figures 6.2, 6.8, and 6.9 correspond approximately to that of the maximum outward boundary excursion, the implication of the phase results in Figure 6.9c is that the maximum boundary excursions occur $\sim 100^\circ$ later in phase than local maxima in B_θ , or equivalently $\sim 80^\circ$ earlier in phase than local minima in B_θ i.e. approximately in lagging quadrature. This result will be discussed in section 6.9.

As indicated in section 6.3, the phases shown here correspond to the midpoints of the magnetosphere intervals observed during boundary oscillations, employed as a proxy for the maximum outward boundary excursion. However, as discussed in section 5.4, the midpoints of such intervals do not correspond exactly to the maxima, due to the finite speed of the spacecraft relative to the oscillating boundary. As shown in Figure 5.4, for a boundary undergoing simple harmonic oscillations, the phase shift for boundary crossings in which only a few (e.g., $N \approx 1-3$) oscillations are observed, as is typical here, is $\sim 10^\circ - 20^\circ$, to later phases for inbound passes, and to earlier phases for outbound passes.

We have examined whether these shifts are discernable in our data set, contributing to the overall phase scatter seen in Figure 6.9. For this purpose, in Figure 6.10 we have separated the oscillations observed on inbound and outbound passes, and have determined the mean θ phase of each distribution. ‘Grazing’ passes have been excluded. The mean value for inbound passes is $105^\circ \pm 9^\circ$ (the error being the standard error of the mean), while that for outbound passes is $101^\circ \pm 10^\circ$, the difference being consistent with zero. The magnitude of this effect is evidently small compared with the overall scatter, such that we conclude that the systematic phase shifts expected due to this effect are only of minor significance in the overall analysis, particularly when inbound and outbound data sets are combined together.

6.8 Estimates of the Boundary Oscillation Amplitude

Estimates of the amplitude of the boundary oscillation can be made using two complementary approaches. First, we can determine the width of the layer in which oscillations were observed by determining the displacement z_L of the spacecraft normal to the boundary between the first and last crossings of each oscillation episode. Values of z_L for all non-‘grazing’ episodes are provided in column seven of Table 6.1. As indicated in section 5.5, this displacement is always less than twice the oscillation amplitude, but an approximate correction can be applied using the results shown in Figure 5.5 and Table 5.1 (fifth column). These provide representative values of the ratio of the observed layer width, z_L , to the oscillation amplitude, z_{B0} , for differing numbers of observed oscillations N , at the relative velocity between the boundary and spacecraft for which observations of that N are most probable. The ratio (z_L/z_{B0}) shown in Figure 5.5 and Table 5.1 increases towards the value of 2 as N increases, because the true width of the layer towards which z_L

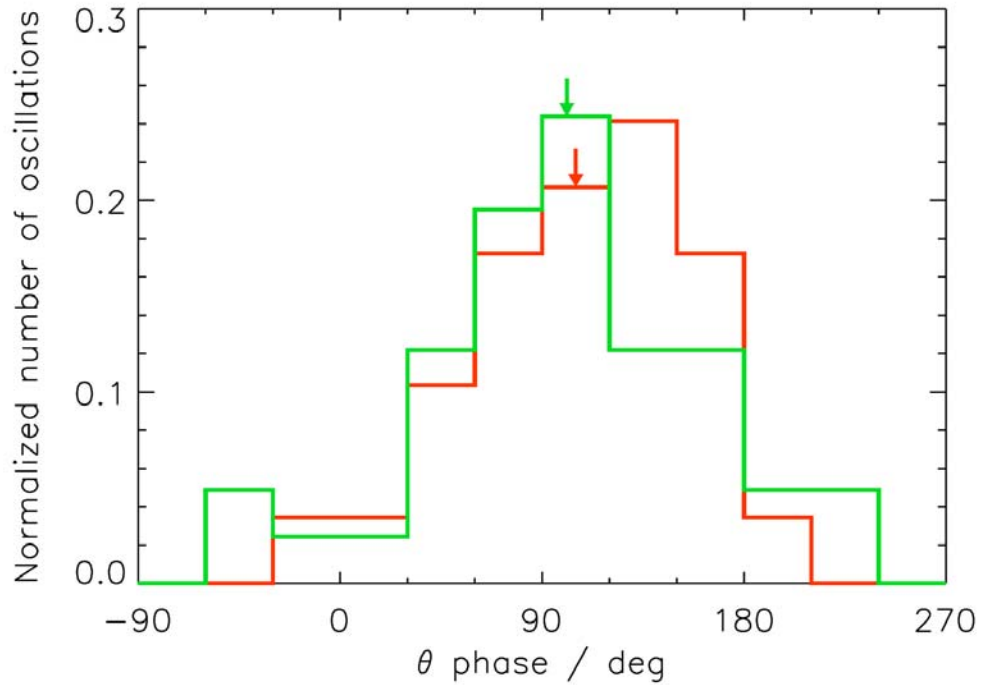


Figure 6.10 Histograms of the normalized number of observed oscillations versus the θ phase at the centre of the magnetosphere interval of the oscillation for inbound passes (red) and outbound passes (green). Normalization is to the total number of oscillations in each case (29 inbound and 41 outbound). ‘Grazing’ passes are excluded. Vertical arrows with the same colour-coding mark the means in the two distributions.

asymptotes as the relative speed becomes small and the number of oscillations N becomes large, is of course just twice the amplitude z_{B0} . Writing these representative values of (z_L/z_{B0}) for given N as $k_A(N)$ for simplicity, we can thus estimate the oscillation amplitude for an episode of N oscillations as

$$z_{B0} \approx \frac{z_L}{k_A(N)}, \quad (6.9)$$

where z_L is the observed width of the layer between first and last crossings.

Second, we pointed out in section 5.3 that the number of oscillations observed is also indicative of the spacecraft speed normal to the boundary relative to the boundary velocity amplitude. Thus, if we know the velocity of the spacecraft normal to the boundary $|v_{Sn}|$ (and knowing the oscillation period), we can estimate the velocity amplitude of the boundary v_{B0} , and hence the displacement amplitude z_{B0} . In other words, if we suppose that an episode of N oscillations corresponds to a certain relative speed $v'_S = (v_S/v_{B0})$, then we can estimate $v_{B0} \approx |v_{Sn}|/v'_S$, and hence

$$z_{B0} \approx \frac{v_{B0}\tau_B}{2\pi} \approx \frac{|v_{Sn}|\tau_B}{2\pi v'_S}. \quad (6.10)$$

Certainly for large N , for example, it would be reasonable to estimate $v'_S \sim v'_N$, the speed at which the probability of observing N oscillations is a maximum, as given in the second column of Table 5.1.

We thus have two independent methods of estimation, but it is easy to see that they should give comparable results from the fact that z_L in equation (6.9) is equal to $|v_{Sn}|$ multiplied by the time the spacecraft remains in contact with the oscillating boundary.

Representative values of the time between successive like crossings of the boundary τ_C for given N , normalized to the true boundary period τ_B , are shown in Figure 5.3 and in Table 5.1 (fourth column). Writing these representative values of the ratio (τ_C/τ_B) for given N as $k_B(N)$ for simplicity, we can then write the total time in contact with the boundary as approximately $N\tau_C \approx k_B(N)N\tau_B$, such that the observed width of the oscillation layer is approximately $z_L \approx k_B(N)N\tau_B|v_{Sn}|$. Then for the first estimation method we obtain from equation (6.9)

$$z_{B0} \approx \frac{k_B(N)}{k_A(N)} N |v_{Sn}| \tau_B, \quad (6.11a)$$

while if we put $v'_S \approx v'_N \approx 1/\pi N$ in equation (6.10) for the second estimation method (see equation (5.7b) and the third column of Table 5.1) we have

$$z_{B0} \approx \frac{1}{2} N |v_{Sn}| \tau_B. \quad (6.11b)$$

If we take e.g. $k_A(N) \sim 1.5$ from Figure 5.5 (fifth column of Table 5.1), and $k_B(N) \sim 0.9$ from Figure 5.3 (fourth column of Table 5.1), then $k_B/k_A \sim 0.6$, which is essentially the same as the equivalent value $1/2$ in (6.11b). The two estimation methods should thus produce similar results, as expected.

One point to note about the estimates of z_{B0} given by equations (6.9) and (6.10) is that we have assumed in their derivation that the mean speed of the boundary is negligible during the crossing, while v'_S in the theory in Chapter 5 is the true normalized relative velocity that depends not only on the spacecraft speed but also on the mean boundary speed. If account is taken of a possible finite boundary velocity $\langle v_B \rangle$ during an oscillation

episode, where $\langle v_B \rangle$ is taken to be positive in the direction of the spacecraft motion, then it is easy to show that the true oscillation amplitude z_{B0}^* and the amplitude estimate based on assuming $\langle v_B \rangle = 0$ given by z_{B0} from equations (6.9) and (6.10) are related by

$$z_{B0} = \frac{z_{B0}^*}{\left(1 - \frac{\langle v_B \rangle}{v_{Sn}}\right)}, \quad (6.12)$$

a formula that applies to both methods. Thus the amplitude estimated with the assumption $\langle v_B \rangle = 0$ will be larger than the true value if the boundary moves in the same direction as the spacecraft (but with lesser speed) and will be smaller than the true value if it moves in the opposite direction (and will be equal to the true value, of course, if $\langle v_B \rangle = 0$). Of course we have no simple way of determining the boundary motion in individual cases, but over an ensemble of cases, and for $\langle v_B \rangle$ not too large compared with $|v_{Sn}|$, the effect may be expected to approximately cancel out. It may also be noted that because the above factor applies equally to the two methods, mean boundary motion is not expected to result in inconsistencies in the amplitude estimates derived from equations (6.9) and (6.10).

For both these methods we then need to determine the normal to the magnetopause, for which purpose we employ the *Arridge et al.* [2006] model boundary, as used to determine the values of the normal speed given in Table 6.1. This model should provide a good overall description of the boundary shape even in the presence of oscillations, since the latter are expected to have very large spatial scales along the boundary as previously noted in Chapter 5. We also note that the model was, of course, derived from essentially

the same Cassini magnetopause observations as those examined here, though using a much restricted data interval from early in the mission.

As previously mentioned in section 6.6, *Arridge et al.* [2006] assumed that the magnetopause is described by a surface of revolution about the KSM X -axis, such that expressed in spherical polar (r, θ) coordinates relative to this axis (e.g. Figure 6.7d) the boundary is given by

$$r(\theta) = r_0(D_p) \left(\frac{2}{1 + \cos \theta} \right)^{K(D_p)}, \quad (6.13a)$$

where the subsolar radius of the surface at $\theta = 0$, $r_0(D_p)$, is given by

$$r_0(D_p) = a_1 D_p^{-a_2}, \quad (6.13b)$$

where $a_1 = 9.7 R_S$ and $a_2 = 1/4.3$, and exponent $K(D_p)$ is given by

$$K(D_p) = a_3 + a_4 D_p, \quad (6.13c)$$

where $a_3 = 0.77$ and $a_4 = -1.5$. Here D_p is the solar wind dynamic pressure in nPa, treated here simply as a quantity that parameterizes the boundary position and shape. The unit outward normal to the boundary in these coordinates can then be shown to be (see Appendix A3 of *Arridge et al.* [2006])

$$\hat{n} = \frac{\left(\hat{r} - \frac{K \sin \theta}{1 + \cos \theta} \hat{\theta} \right)}{\left(1 + \frac{K^2 \sin^2 \theta}{(1 + \cos \theta)^2} \right)^{\frac{1}{2}}}, \quad (6.14)$$

which can readily be converted to other coordinate systems such as KSM employed here. To determine the normal for a given boundary observation we first iteratively determine

D_p from equation (6.13) such that the model boundary passes through the observation point, and then find the normal direction from equation (6.14). The displacement of the spacecraft normal to the boundary can then be determined from the spacecraft displacement vector $\Delta\mathbf{R}$ between the first and last crossings as $z_L = \Delta\mathbf{R} \cdot \hat{\mathbf{n}}$, while from the spacecraft velocity vector \mathbf{v}_S we determine $v_{Sn} = \mathbf{v}_S \cdot \hat{\mathbf{n}}$ (positive outbound and negative inbound). The values of z_L and v_{Sn} so determined are those given in Table 6.1.

Results are shown in Figures 6.11-6.13. ‘Grazing’ passes are excluded from this analysis, and, in Figures 6.12 and 6.13, if a pass contains more than one episode then for definiteness only the first episode outbound and the last episode inbound are included. The latter restriction is necessary if we are to make a comparison of the relative occurrence of $N=0$ and $N=1$ episodes, since there can, by definition, be no more than one $N=0$ episode during a pass, but it is possible for there to be more than one $N=1$ episode, a fact that would introduce a bias towards $N=1$ episodes if multiple cases on a pass were included.

In Figure 6.11 we show histograms of the number of observed oscillation episodes versus the spacecraft displacement normal to the boundary, z_L , estimated as above, in $1 R_S$ bins, shown separately in panels (a)-(c) for $N=1$, 2, and ≥ 3 oscillation episodes. The mean values of z_L are indicated by the vertical arrows in each panel, having values of 1.8, 3.7, and $4.9 R_S$ for $N=1$, 2, and ≥ 3 , respectively, the distributions being very broad in the last two cases. Overall, these values suggest oscillation amplitudes of a few R_S , increasing with increasing numbers of oscillations observed.

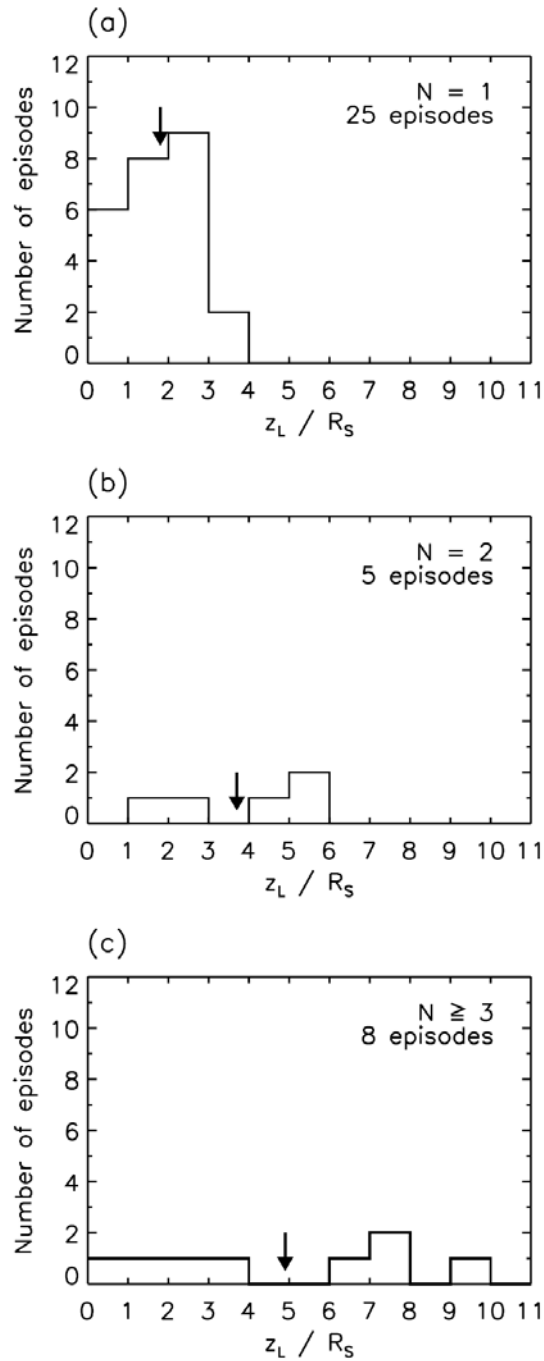


Figure 6.11 Histograms of the number of observed oscillation episodes versus the displacement z_L of the spacecraft normal to the magnetopause between the first and last crossings of each episode, shown separately in panels (a)-(c) for $N = 1, 2$, and ≥ 3 oscillation episodes. Note that episodes from ‘grazing’ passes have been excluded.

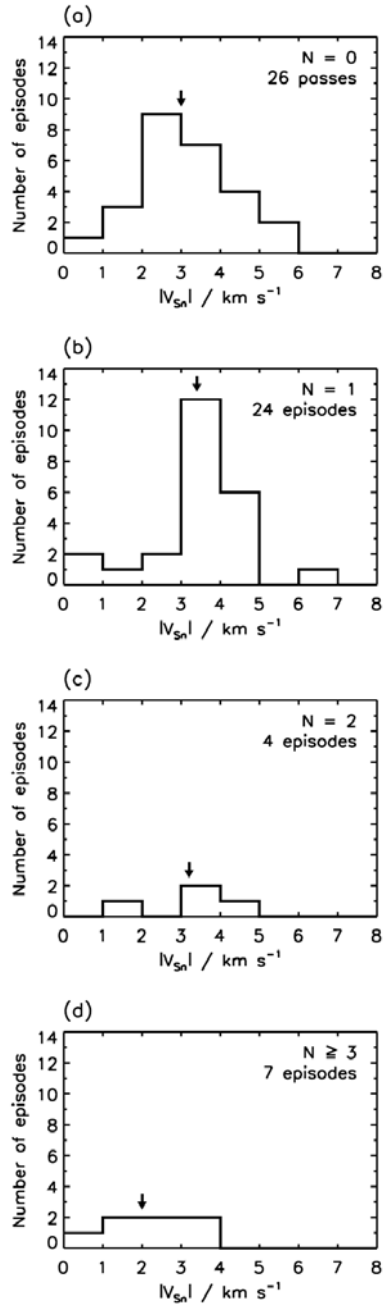


Figure 6.12 Histograms of the number of observed oscillation episodes (or in the case of $N = 0$, the number of passes) versus the spacecraft speed normal to the magnetopause boundary $|v_{sn}|$, shown separately in panels (a)-(d) for $N = 0, 1, 2$, and ≥ 3 . ‘Grazing’ passes are excluded, and if a pass contains more than one episode only the first episode outbound and the last episode inbound are included.

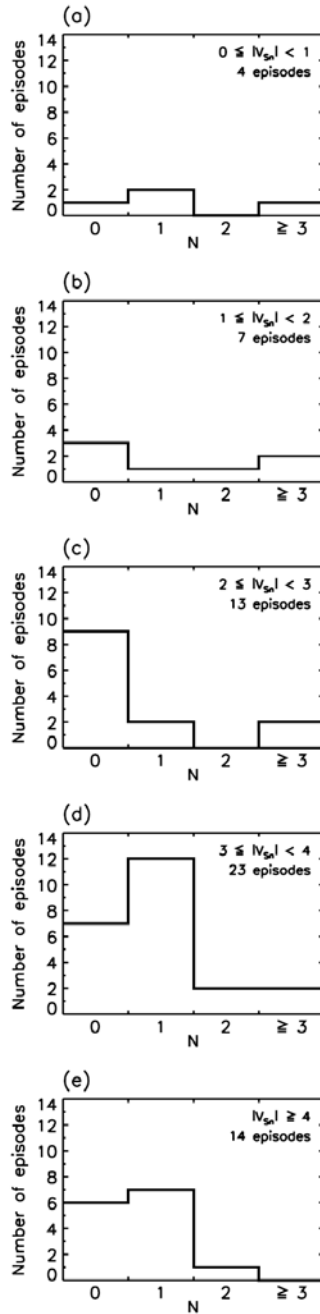


Figure 6.13 Histograms of the number of observed oscillation episodes versus the number of oscillations belonging to each episode N , shown separately for the ranges (in km s^{-1}) of spacecraft speed normal to the magnetopause boundary $|v_{Sn}|$ indicated at top right. ‘Grazing’ passes are excluded, and if a pass contains more than one episode only the first episode outbound and the last episode inbound are included.

In Figure 6.12 we similarly show histograms of numbers of episodes (or in the case of $N = 0$, numbers of passes) versus $|v_{Sn}|$ in 1 km s^{-1} bins, again separately for $N = 0, 1, 2$, and ≥ 3 . The mean values are again shown by the vertical arrows, at $3.0, 3.4, 3.2$, and 2.0 km s^{-1} , respectively. The last of these values suggests that large N is also related to lower boundary normal speed, as expected. The latter point is examined in an alternative way in Figure 6.13, where we instead show the numbers of episodes versus N for $N = 0, 1, 2$, and ≥ 3 , for separate ranges of $|v_{Sn}|$ in 1 km s^{-1} bands. It can be seen that large N cases (≥ 3) are a significant component of the overall distributions for $|v_{Sn}|$ in the ranges $0-1$ and $1-2 \text{ km s}^{-1}$, while the distributions become completely dominated by roughly equal numbers of $N = 0$ and $N = 1$ cases for larger $|v_{Sn}|$, particularly above $|v_{Sn}| \sim 3 \text{ km s}^{-1}$. Since normal speeds are typically $\sim 2 \text{ km s}^{-1}$ and above as can be seen in Table 6.1, the overall distribution of N shown in Figure 6.6 (for passes rather than episodes) is also dominated by $N = 0$ and 1 cases.

We now examine these results in more detail in relation to the above discussion of the boundary oscillation amplitude. Consider first the $N = 1$ cases in panels (a) and (b) of Figures 6.11 and 6.12, respectively, which indicate a mean observed width of the oscillation layer of $z_L = 1.8 R_S$ and a mean spacecraft speed normal to the boundary of 3.4 km s^{-1} . To apply equations (6.9) and (6.10) to these values to estimate the oscillation amplitude we need first to estimate a normalized speed v'_S . We note from Figure 5.2, however, that $N = 1$ oscillations can occur over a wide range of relative normalized speeds $0.2172 \leq v'_S < 1$. However, the above results imply that typical values correspond to those for which $N = 0$ and $N = 1$ passes occur with roughly equal frequency, which suggests

from Figure 5.2 that $v'_S \sim 0.3$ is reasonable. At this value we then find $k_A \sim 1.4$ from Figure 5.5, such that equation (6.9) yields for the mean layer width of $1.8 R_S$ an estimate of the oscillation amplitude of $1.3 R_S$. Using the same value of v'_S in equation (6.10) together with $\tau_B \approx 10.8$ h and a mean normal speed of 3.4 km s^{-1} yields an estimated boundary velocity amplitude of $|v_{Sn}|/v'_S \sim 11 \text{ km s}^{-1}$ and a displacement amplitude of $z_{B0} \sim 1.2 R_S$, which is thus in good accord with the previous estimate.

We similarly consider the results for the $N = 2$ boundary crossings in panels (b) and (c) of Figures 6.11 and 6.12, respectively. In this case Figure 5.2 strongly indicates that the choice $v'_S \approx v'_2 \approx 0.128$ is appropriate, such that a mean z_L value of $3.7 R_S$ together with $k_A \sim 1.4$ from Figure 5.5 and Table 5.1 yields $z_{B0} \sim 2.6 R_S$ from equation (6.9). The mean normal velocity of 3.2 km s^{-1} with the above v'_S value indicates a boundary velocity amplitude of $\sim 25 \text{ km s}^{-1}$ and a displacement amplitude of $z_{B0} \sim 2.6 R_S$. Again, the two values are in good agreement. These results suggest that the modest number of $N = 2$ passes in our data set occur under similar orbital conditions to the more usual $N = 0$ and 1 boundary passes (with comparable mean normal spacecraft speeds), but correspond to larger boundary oscillation amplitudes in these cases by a factor of ~ 2 .

We now consider the results for the $N \geq 3$ passes together, as shown in panels (c) and (d) of Figures 6.11 and 6.12, respectively. The results in Figure 5.2 again suggest that a value of v'_S corresponding to the maximum probability of a given N is the most appropriate, and in view of the overall results shown in Figure 6.6 we choose v'_4 for definiteness, corresponding to $v'_N \approx 0.0709$. With a mean z_L value of $4.9 R_S$ (though with

a very large spread indeed) and $k_A \sim 1.65$ from Figure 5.5 and Table 5.1, we then estimate from equation (6.9) $z_{B0} \sim 3.0 R_S$. Similarly with a mean normal velocity of 2.0 km s^{-1} we estimate from equation (6.10) a velocity amplitude of $\sim 28 \text{ km s}^{-1}$ and a displacement amplitude of $z_{B0} \sim 2.9 R_S$. These two values are again in good agreement, especially given the breadth of the z_L distribution. The results suggest that these cases correspond to the larger amplitude conditions inferred from the $N = 2$ data, but observed on orbits with smaller speeds normal to the boundary.

We finally comment specifically on the four $N \geq 3$ episodes evident in Figure 6.11c which exhibit very large spacecraft displacements within the oscillation layer, with z_L exceeding $6 R_S$, thus apparently implying very large oscillation amplitudes in these cases. As already discussed above, extended intervals spent within the oscillation layer could result from solar wind-induced motions of the boundary that partially match the spacecraft motion, thus leading to overestimates of the oscillation amplitude (given by equation (6.12)). Such boundary motions would have to persist over many-hour intervals during these high- N episodes, however, for this effect to be a major factor in these cases, which may seem unlikely. Indeed, two of these cases correspond to Rev 44 outbound with $N = 10$ and $z_L = 7.3 R_S$ (though noting the scattered phase of the last three of these oscillations), and Rev 45 inbound with $N = 4$ and $z_L = 9.2 R_S$, that are shown as examples in Figure 6.4. In these cases, therefore, we would require on the same apoapsis pass outward motion of the boundary matching the spacecraft motion for ~ 2 days outbound, followed by inward motion of the boundary matching the spacecraft motion for ~ 2 days inbound, which seems very unlikely. Rather, it seems more reasonable to suggest that the

boundary oscillation amplitude was indeed very large during this interval, with an amplitude at modest northern latitudes in the mid-afternoon sector (Table 6.1) of $\sim 4-5 R_S$, compared with a mean boundary radius of $\sim 30 R_S$. We note that the other large-amplitude examples, Rev 46 inbound with $N=4$ and $z_L=6.7 R_S$, and Rev 47 outbound with $N=4$ and $z_L=7.4 R_S$, also occurred in the same epoch at a similar location, although other adjacent passes in the same region show no evidence for this effect (Table 6.1).

6.9 Summary and Discussion

In this chapter we have made a first systematic study of the oscillations of Saturn's magnetopause that are related to the internal field and plasma oscillations near the magnetospheric period (~ 10.8 h), following the case study of Pioneer-11 data by *Espinosa and Dougherty* [2001] and *Espinosa et al.* [2003a] and our own case studies of Cassini data in Chapter 4. We have used magnetic field and plasma electron data from ~ 40 Cassini orbits that crossed the magnetopause, which occurred during the interval from SOI in July 2004 to Rev 55 inbound at the end of 2007. While occasional intervals of multiple boundary crossings separated near the magnetospheric period provide convincing evidence for such boundary oscillations, more frequently only one or two re-entries occur, with a broad range of intervals between like crossings of the boundary that can be due both to the finite speed of the spacecraft through the boundary region (section 5.4) and the effect of other physical processes that also modulate the boundary position. Here, therefore, we selected re-entries for analysis within a broad timing window, between 0.4 and 1.6 of the magnetospheric period, and verified that these events are indeed associated with boundary

oscillations at the magnetospheric period by showing that their phase is well organized by the phase of the internal magnetic field oscillations within the ‘core’ region of the magnetosphere [Provan *et al.*, 2009a]. Such phase organization requires that the two oscillatory phenomena must have a common synodic period within $\sim 0.05\%$ over the ~ 3.5 years of the study.

Further analysis of the magnetospheric period boundary oscillations selected by these means then yields the following main results.

(a) Magnetopause boundary oscillations near the magnetospheric period are commonly observed on Cassini passes that cross the boundary region, with $\sim 60\%$ of such passes showing one or more such oscillations. Of those that do show oscillations, $\sim 65\%$ show one oscillation only, while $\sim 10\%$ show two oscillations, and $\sim 25\%$ show three or more.

(b) Magnetopause oscillations are observed at all LTs in which magnetopause crossings occurred on the Cassini orbit, from ~ 3.5 h LT in the pre-dawn sector, through noon, to ~ 17 h LT near dusk, and at KSM latitudes in the range $\pm 40^\circ$ (though most passes were at low latitudes within $\pm 20^\circ$).

(c) Estimates based on the spacecraft displacement perpendicular to the magnetopause while located in the oscillation region, and on the spacecraft speed normal to the boundary in relation to the number of oscillations observed, suggest a typical oscillation amplitude of $\sim 1.2 R_S$ with a velocity amplitude of $\sim 11 \text{ km s}^{-1}$. Such an oscillation yields approximately equal numbers of passes with zero and one observed oscillation at typical spacecraft normal speeds of $\sim 3.4 \text{ km s}^{-1}$. These values are comparable to estimates made in Chapter 4. Similar estimates for the smaller number of episodes with two observed oscillations suggest amplitudes of about twice this with similar normal velocities, while

observations of episodes of three or more oscillations suggest similar amplitudes of $\sim 3 R_S$ combined with smaller spacecraft normal velocities of $\sim 2 \text{ km s}^{-1}$ (roughly half the typical value). Evidence has also been presented suggesting the occasional occurrence of extreme amplitudes of $\sim 4 - 5 R_S$, all of which were observed in the post-noon sector.

(d) With respect to the magnetic field oscillations within the quasi-dipolar ‘core’ magnetosphere, the distribution of outward boundary displacement maxima is peaked at a field oscillation phase of $\sim 160^\circ$. This result shows that maximum outward boundary excursions typically lag maxima in B_r and B_θ in the ‘core’ at the same LT by $\sim 160^\circ$, and hence maxima in B_ϕ by $\sim 70^\circ$. The quasi-uniform ‘core’ field in the equatorial plane formed by the B_r and B_ϕ field components is thus typically rotated $\sim 160^\circ$ anti-clockwise (as viewed from the north) from the instantaneous position of outward boundary maxima, thus pointing approximately away from the latter.

(e) The oscillation phase is also found to vary with radial distance to the boundary, and hence also with LT, moving to somewhat smaller phases for smaller radial distances (near-noon sector) and to larger phases for larger radial distances (flanks). This suggests an effect associated with outward radial propagation of the pressure disturbance leading to boundary motion, the radial phase dependency indicating an outward phase speed of $\sim 270 \pm 80 \text{ km s}^{-1}$. Using a revised phase model incorporating a constant outward phase speed of 210 km s^{-1} based on analysis of B_θ field oscillations inside the boundary, yields an essentially constant phase for boundary displacement maxima, independent of radial distance, of $\sim 100^\circ$ (with 89% of data falling within the 180° phase range $30^\circ - 210^\circ$), where 0° corresponds to B_θ maxima. Thus maximum outward boundary excursions

typically occur $\sim 100^\circ$ after B_θ maxima in the outer magnetosphere, or equivalently $\sim 80^\circ$ ahead of B_θ minima.

A sketch summarizing these phase relationships and their relation to other oscillatory phenomena discussed in Chapter 2 is shown in Figure 6.14. This shows the equatorial magnetosphere viewed from the north with the direction to the Sun (X) at the top and dusk (Y) to the left. We show the system at one particular phase of the rotation determined by the value of Φ_M (see equations (6.1b) and (6.4)), which for definiteness has been chosen to be $\Phi_M = 210^\circ$, corresponding to the phase at which the emitted power of SKR emissions is a maximum [Andrews *et al.*, 2008; Provan *et al.*, 2009a]. The phase fronts of given ‘core’ magnetic phase Ψ_{Mc} (equation (6.1b)) at this instant are shown by the radial black lines marked with phase values at 90° intervals, with $\Psi_{Mc} = 0^\circ$ located at 2 h LT in the post-midnight sector, increasing clockwise around the diagram. Within the quasi-dipolar ‘core’ region, whose outer boundary is indicated by the black dashed circle at $\sim 15 R_S$, instantaneous maxima of the B_r and B_θ field components then occur at $\Psi_{Mc} = 0^\circ$ at 2 h LT and minima at 180° at 14 h LT according to the Provan *et al.* [2009a] phase model (equation (6.1a)), while maxima of B_ϕ occur at $\Psi_{Mc} = 90^\circ$ at 20 h LT and minima at 270° at 08 h LT. The equatorial B_r and B_ϕ field components then combine to form a quasi-uniform field in the equatorial plane within the ‘core’ shown by the solid black arrows, that is directed (at SKR power maxima) tailward and dawnward, as indicated in Chapter 2. With increasing time this pattern rotates anti-clockwise with the (near-planetary) magnetospheric period given by equation (6.5), giving rise to the observed oscillating fields.

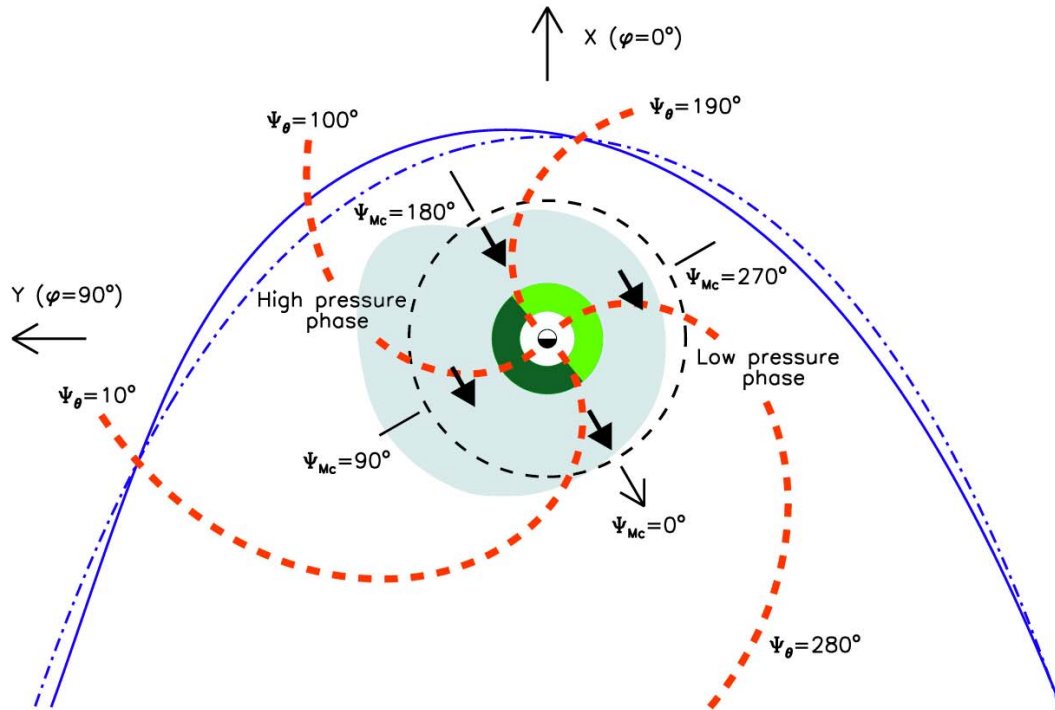


Figure 6.14 Sketch showing the relationships between various oscillatory phenomena in Saturn's equatorial magnetosphere, where the view is from the north with the direction to the Sun (X) at the top of the figure and dusk (Y) to the left. As illustrated, outward excursions of the magnetopause are found to map back along the spiral phase fronts into both the rotating plasma 'bulge' in the outer magnetosphere reported by *Burch et al.* [2009] and the plasma density maximum in the inner Enceladus plasma torus observed by *Gurnett et al.* [2007].

The relationship to the longitudinal plasma asymmetries reported by *Gurnett et al.* [2007] and *Burch et al.* [2009] are shown by the green and pale blue regions, respectively, in Figure 6.14. Specifically, the plasma density asymmetry observed by *Gurnett et al.* [2007] within the inner part of the Enceladus torus, between ~ 3 and $\sim 6 R_S$, is shown schematically by the green shaded region within the inner ‘core’, where dark green indicates enhanced density. The maximum plasma density in the torus occurs at $\Psi_{Mc} = 80^\circ$, at the middle of the dark green segment, located at ~ 21 h LT in the post-dusk sector at the instant depicted, with the minimum density at 260° in the post-dawn sector. (*Gurnett et al.* [2007] express the phase of the density maximum as occurring at $\lambda_{SKR} \approx 330^\circ$ in the SKR-based longitude system they employ, which is related to the magnetic phase employed here by $\Psi_{Mc} \approx \lambda_{SKR} - 250^\circ$ [*Andrews et al.*, 2008; *Provan et al.*, 2009a], thus giving $\Psi_{Mc} \approx 80^\circ$.) The rotating plasma density perturbations in the torus are thus very nearly in phase with the B_ϕ field oscillations within the ‘core’ as indicated by *Gurnett et al.* [2007], and in lagging quadrature with B_r and B_θ . The longitudinal plasma asymmetry reported by *Burch et al.* [2009] is similarly indicated by the pale blue area in the figure. The distribution extends asymmetrically outwards to distances of $\sim 20 R_S$ in the range $\Psi_{Mc} \approx 35^\circ - 160^\circ$ ($\lambda_{SKR} \approx 285^\circ - 50^\circ$), thus centred on $\Psi_{Mc} \approx 95^\circ$ in the post-dusk sector at the instant depicted, similar to the phase of the maximum in the inner torus density.

The red dashed spirals in Figure 6.14 show lines of constant ‘ θ phase’ Ψ_θ given by equation (6.8), where we note that Ψ_θ becomes equal to Ψ_{Mc} at a radial distance of $\sim 12.1 R_S$ in the outer ‘core’ region (where the empirically-determined value of function

ψ_θ^* in equation (6.8) is zero as shown in panel (a) of Figure 6.9). Specifically we show the instantaneous spirals corresponding to $\Psi_\theta = 10^\circ$, 100° , 190° , and 280° , which also rotate with time similarly to the above. According to the results shown in Figure 6.9, maximum outward displacements of the magnetopause occur where the instantaneous spiral for $\Psi_\theta \approx 100^\circ$ intersects the boundary, with the maximum inward displacement occurring at 280° , and zero displacements between at $\Psi_\theta \approx 10^\circ$ and 190° . These results are reflected in the magnetopause positions shown in the outer part of the figure, where the blue dot-dashed line shows the mean model of *Arridge et al.* [2006], specifically for a typical solar wind dynamic pressure of 0.03 nPa, while the blue solid line shows the displaced boundary. The latter is thus maximally displaced outward at ~ 16 h LT where the $\Psi_\theta \approx 100^\circ$ spiral intersects the boundary, has zero displacement at ~ 11 h LT where the $\Psi_\theta \approx 190^\circ$ spiral intersects the boundary, and is displaced inward at earlier LTs in the dawn sector. It may be noted that the radial propagation speed determined in this chapter is much higher than the value of 50 km s^{-1} estimated by *Cowley et al.* [2006], resulting in less tightly wound phase fronts (compare Figures 6.14 and 2.6).

As discussed in Chapter 4, these boundary motions must reflect changes in the total field plus plasma pressure in the outer magnetosphere which cause the magnetopause to move outward or inward to match the (in principle) constant dynamic pressure exerted on the magnetosphere by the solar wind. In this case the $\Psi_\theta \approx 100^\circ$ spiral must correspond to a maximum in the total pressure in the outer magnetosphere, as marked in the figure, and the $\Psi_\theta \approx 280^\circ$ spiral to a minimum in the total pressure. Thus we note that, as depicted in the figure, SKR power maxima occur when the high pressure phase is in the pre-dusk

sector in the outer magnetosphere, and the low pressure phase in the pre-dawn sector. While determination of the physical origin of this relation remains for future work, we note correspondingly that the high pressure sector relates approximately to the sector containing the plasma ‘bulge’ in the outer magnetosphere reported by *Burch et al.* [2009]. Further, if we follow the high-pressure phase front into the inner ‘core’ region it maps closely to the density maximum in the Enceladus torus, as can be seen from the corresponding spiral in the figure. Specifically, at the radius of Enceladus at a distance of $\sim 4 R_S$, $\Psi_\theta \approx 100^\circ$ corresponds to $\Psi_{Mc} \approx 81^\circ$ according to equation (6.8), compared with the phase of maximum density in the torus of $\Psi_{Mc} \approx 80^\circ$ as indicated above. Thus taking account of the empirically-determined radial phase propagation of these phenomena within the magnetosphere, the high-pressure region in the outer magnetosphere which causes outward excursions of the magnetopause is directly connected not only with the plasma ‘bulge’ in the outer magnetosphere, but also with the high-density region of the Enceladus torus. Further studies of combined magnetic field and plasma data are required to further elucidate the physical origins of these phenomena.

Chapter 7

Magnetospheric Period Oscillations of Saturn's Bow Shock

7.1 Introduction

The bow shock is a consequence of the interaction between the supersonic solar wind and the magnetospheric obstacle, such that the positions of the bow shock and magnetopause boundaries should be directly related. Thus the oscillatory motion of the magnetopause discussed in Chapters 4 and 6 should produce similar motion of the shock surface. However, to date no evidence has been presented for such bow shock oscillations, other than that in Chapter 4 which is of a very marginal nature. In this chapter we examine Cassini observations of the bow shock during 2004-2007 and show that such oscillations are indeed commonly present. Two case studies are presented exhibiting both bow shock and magnetopause oscillations on given spacecraft passes, together with a statistical study showing that bow shock oscillations observed within a timing window between 0.6 and 1.6 of the magnetospheric period are significantly organized by the phase of the interior field oscillations. We also provide evidence that their phase and amplitude are comparable with those of the corresponding magnetopause oscillations.

7.2 Data Set Employed

In this chapter we use Cassini data from Saturn Orbit Insertion (SOI) in July 2004 to Rev 55 inbound in late December 2007, this being the interval for which *Provan et al.* [2009a] determined the phase of the 'core' region magnetic field oscillations, and the

interval examined in Chapter 6 for magnetopause oscillations. The orbits used here divide into two intervals, the first of which involves bow shock crossings at low planetary latitudes in the morning sector (SOI to Rev 21), while the second involves crossings in the post-noon to dusk sector (Revs 40 to 55), some of which occur at latitudes significantly away from the equator. The gap between these intervals corresponds mainly to Revs for which apoapsis was located in the nightside sector, and is wider than that in the corresponding magnetopause study since a small number of orbits near the ‘ends’ of the gap cross the magnetopause but do not achieve sufficient radial distances to also encounter the bow shock. Data gaps necessitated the exclusion of one orbit and affected several others to varying degrees without rendering them wholly unusable. In all, 35 Cassini orbits involving crossings of the bow shock are used.

7.3 Examples of Bow Shock Oscillations

Crossings of the bow shock and magnetopause were identified by examination of 1 min averaged magnetic field data from the fluxgate magnetometer, together with 1 min averaged electron data from the ELS electron spectrometer. Transitions across the bow shock from the upstream solar wind to the magnetosheath are readily recognized in the combined magnetic field and thermal electron data by sudden simultaneous increases in the electron flux in the range ~ 10 - 100 eV and in the field strength, while transitions across the magnetopause from the magnetosheath to the magnetosphere are characterized by substantial reductions in the electron flux in the ~ 10 - 100 eV range and increases at ~ 100 eV- 1 keV, along with increases in the field strength, generally accompanied by changes in direction to southward orientations and reductions in variability. Visual

inspection of the data is sufficient to detect many examples of magnetopause oscillations near the magnetospheric period, which analysis shows are closely related to the phase of the magnetospheric field oscillations. Overall, the behaviour of the bow shock appears rather more variable, so that oscillations near the magnetospheric period are generally less obvious. Nevertheless, such oscillatory behaviour is evident on a number of passes, two of which are presented here as examples.

Figure 7.1 shows 4 days of data (days 313-316 of 2007) from the inbound pass of Rev 52. The top panel shows an electron count rate spectrogram from anode 5 of the ELS instrument, colour-coded according to the scale on the right. The next four panels show 1 min averaged values of the spherical polar components of the magnetic field referenced to the planet's spin/magnetic axis, together with the magnitude of the field. The bottom panel shows the phase of the 'core' magnetic field oscillations Ψ_{Mc} (modulo 360°) given by equation (6.1b), evaluated at the spacecraft azimuth $\varphi_s(t)$. The phase values are colour-coded according to whether the spacecraft is situated in the solar wind (green), magnetosheath (red), or magnetosphere (blue). We note that since we can write $\Psi_{Mc}(\varphi_s(t), t) = \varphi_M(t) - \varphi_s(t)$ from equations (6.1b) and (6.2) in the previous chapter, the value of Ψ_{Mc} gives the instantaneous angle of the magnetic field within the 'core' region with respect to the azimuth of the spacecraft (positive anti-clockwise viewed from the north, as for the definition of azimuth φ). Spacecraft positional data, specifically local time, colatitude (again with respect to the spin/magnetic axis), and radial distance from the planet's centre, are given at the bottom of the plot. The pass takes place in the mid-afternoon sector, at ~ 15 h LT, near the planet's equatorial plane, with the data shown in the figure spanning a radial range from 46.3 to 34.7 R_S .

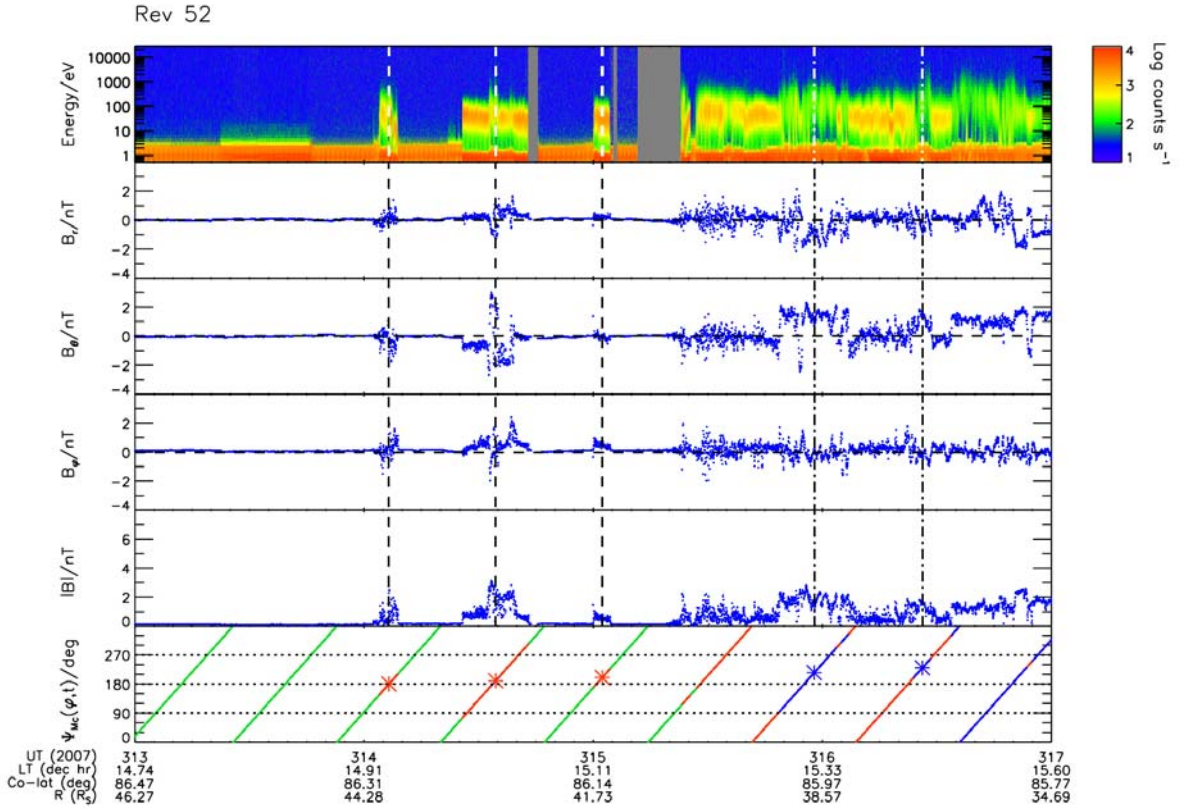


Figure 7.1 The figure shows 4 days of data from the inbound pass of Cassini Rev 52. The top panel shows an electron count rate spectrogram from anode 5 of the ELS instrument. The next four panels show 1 min averaged values of the spherical polar radial (r), colatitudinal (θ), and azimuthal (φ) components of the magnetic field referenced to the planet's spin/magnetic axis, together with the magnitude of the field. The bottom panel shows the Provan phase $\Psi_{Mc}(\varphi, t)$ modulo 360° , the line being colour-coded according to whether the spacecraft is in the solar wind (green), magnetosheath (red), or magnetosphere (blue). Vertical lines mark the centre of magnetosheath intervals during bow shock oscillation episodes (dashed) and magnetosphere intervals during magnetopause oscillation episodes (dot-dashed), while the red and blue stars, respectively, indicate the corresponding Provan phase. Spacecraft positional information is provided at the bottom of the plot.

At the beginning of the interval the spacecraft is located in the solar wind, as is evident from the weak thermal electron fluxes (the intense fluxes at and below a few eV in the spectrogram are principally spacecraft photoelectrons), and the very small field strengths of ~ 0.2 nT. Shortly after the start of day 314 there begins a sequence of three quasi-periodic magnetosheath encounters, the temporal separations between the midpoints of which are ~ 11 h, thus being close to the magnetospheric period. The vertical dashed lines in the top panels mark the midpoints of the encounters, while the stars in the bottom panel show the corresponding Provan phase Ψ_{Mc} at the mid-points, which is near-constant at $\sim 180^\circ$. The latter value means that the ‘core’ equatorial field points approximately away from the spacecraft at the centre times of the magnetosheath encounters, these centre times representing proxies for the times of maximum radial outward displacement of the bow shock. We note that this phasing is essentially the same as that found in Chapter 6 for the maximum outward displacement of the magnetopause. The final crossing into the magnetosheath takes place at ~ 10 h UT on day 315 near to the time of the next expected encounter (when the Provan phase is again $\sim 180^\circ$), following which two quasi-periodic encounters with the magnetosphere are observed, also separated by ~ 11 h as marked by the vertical dot-dashed lines. These have slightly later phases of 215° and 230° , which nevertheless lie well within the usual scatter of magnetopause phase values at this radial distance and local time (section 6.7). After ~ 14 h UT on day 316 the spacecraft finally remains within the magnetosphere on the pass, except for one brief (~ 30 min) excursion into the magnetosheath towards the end of day 316.

The data from this Rev provide good evidence of approximately in-phase (to within a few tens of degrees) magnetospheric period oscillations of the bow shock and

magnetopause on the same pass, which in this case appear to be of considerable amplitude. Assuming that the observed boundary motions are associated wholly with the magnetospheric period oscillations, the radial displacement of the spacecraft between the first bow shock encounter on day 314 and the last on day 315 represents a lower limit for twice the oscillation amplitude. This displacement is $\sim 5 R_S$, thus suggesting an amplitude of $\sim 2.5 R_S$ or more. Indeed, careful inspection of the data during the second quasi-periodic magnetosheath encounter reveals that the spacecraft briefly entered the magnetosphere at the centre of the oscillation, indicating that the boundary motion was sufficient in this particular case to displace both the bow shock and the magnetopause temporarily across the spacecraft. Since the radial separation of the bow shock and magnetopause is typically $\sim 9 R_S$ under the conditions pertaining here [Arridge *et al.*, 2006; Masters *et al.*, 2008], the implied peak-to-trough displacement of the boundary during this particular oscillation must be of comparable magnitude. It may be noted that the examples of particularly large-amplitude oscillations of the magnetopause reported in Chapter 6 were all observed, as here, in the post-noon sector. We also note that the central location of the brief magnetosphere encounter within the transient magnetosheath interval again suggests that the two boundaries oscillate approximately in phase.

The second example in Figure 7.2 shows 9 days of data (days 116-124 of 2007) spanning the apoapsis pass of Revs 43 outbound and 44 inbound. Apoapsis itself occurs at a radial distance of $36.2 R_S$ at ~ 23 h UT on day 122, at ~ 16 h LT. During the first 2 days of the interval the spacecraft passes out from the magnetosphere, across the magnetosheath into the solar wind in the near-equatorial post-noon sector. A number of short-period magnetopause and bow shock encounters are observed, reminding us that the positions of

Rev 43 / 44

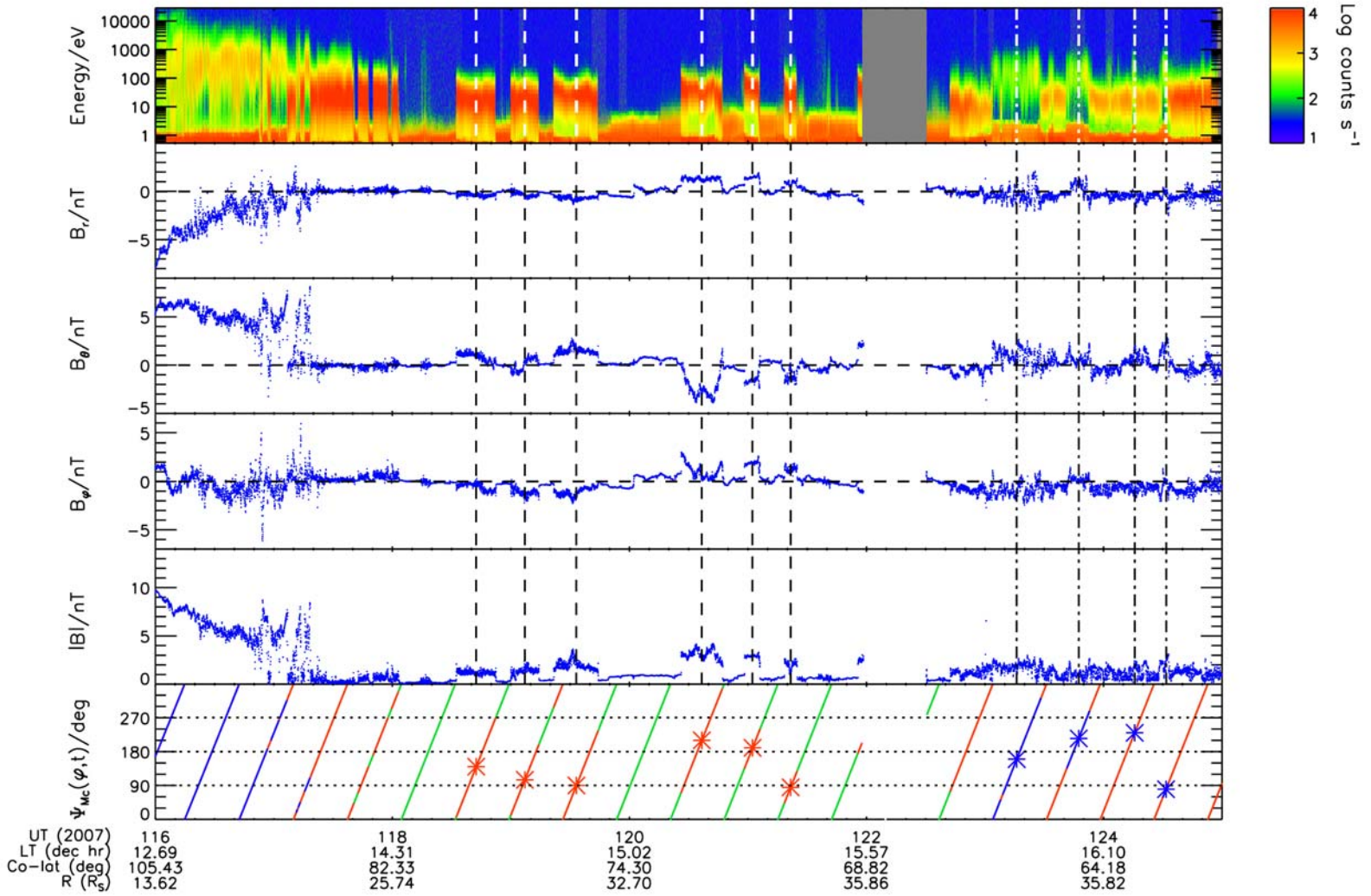


Figure 7.2 The figure shows 9 days of data from the apoapsis interval of Rev 43/44 in the same format as Figure 7.1.

these boundaries are subject to a range of phenomena (e.g., variations in solar wind parameters [Arridge *et al.*, 2006; Masters *et al.*, 2008], magnetic reconnection at the magnetopause [McAndrews *et al.*, 2008], and Kelvin-Helmholtz waves at the magnetopause [Masters *et al.*, 2009], as discussed in section 6.3.2) in addition to the longer-period oscillations studied here. During the approach to apoapsis over the following 4 days, however, a quasi-periodic sequence of magnetosheath encounters near the magnetospheric period are observed, marked by the vertical dashed lines. A sequence of three such encounters occurs on days 118-119, and following one ‘missed’ encounter due possibly to solar wind variations, a further sequence of three encounters takes place on days 120-121. A fourth encounter in the latter sequence is obscured by the data gap beginning near the end of day 121. The Provan phases of these encounters, shown by the red stars in the lower panel, are more scattered than in the previous example, between $\sim 90^\circ$ and $\sim 210^\circ$, but the six values are still grouped within a band of $\sim 120^\circ$ of phase (which also contains the magnetosheath encounter phases in Figure 7.1), avoiding the remaining $\sim 240^\circ$ of phase. After the data gap the spacecraft passes once more between the solar wind and the magnetosheath, and then observes a sequence of four quasi-periodic encounters with the magnetosphere, again marked by the vertical dot-dashed lines. The Provan phases of these magnetosphere encounters are seen to occupy a similar but slightly broader range of phase to those of the magnetosheath encounters ($\sim 80^\circ$ - 230°), but still lying within the usual range of magnetopause phase values at this local time (section 6.7).

7.4 Relation to Magnetic Phase in the ‘Core’ Region

While the examples in Figures 7.1 and 7.2 provide case study evidence for the occurrence of magnetospheric period oscillations of the bow shock related to comparable oscillations of the magnetopause, the evidence in the data from most passes through the boundary region is much less clear cut, consisting in the main of single observed oscillations of the boundaries (if any at all). The approach taken in the study of magnetopause oscillations in Chapter 6 was to apply a timing window to the interval between successive like crossings of the boundary to select those crossings near the magnetospheric period, and then to examine whether this sub-set of crossings is related in phase to that of the magnetic field oscillations within the magnetospheric ‘core’. While spacecraft motion through the boundary region at finite speed results only in crossing intervals that are less than the period of the oscillating boundary (section 5.4), it is recognized that a range of additional phenomena influence these timings as noted above. Consequently, a relatively wide timing window between 0.4 and 1.6 of the magnetospheric period was employed in Chapter 6, it being found that the magnetopause boundary oscillations were significantly organized by the Provan phase over this whole timing window band, though with the numbers of oscillations and the degree of phase organization decreasing towards both ends of the band. This trend is apparent in Figure 7.3 which shows histograms of the number of observed magnetopause oscillations versus Provan phase (modulo 360°) for the non-overlapping set of 0.2 magnetospheric period (mp) timing windows spanning 0.4 to 1.6 of the magnetospheric period (i.e. 0.4-0.6 mp, 0.6-0.8 mp, and so on). Timing windows are specified above each histogram at top right. We have least-squares fitted the histogram values to a sinusoid given by $N = a \cos(\Psi_{Mc} - \Psi_0) + b$ and

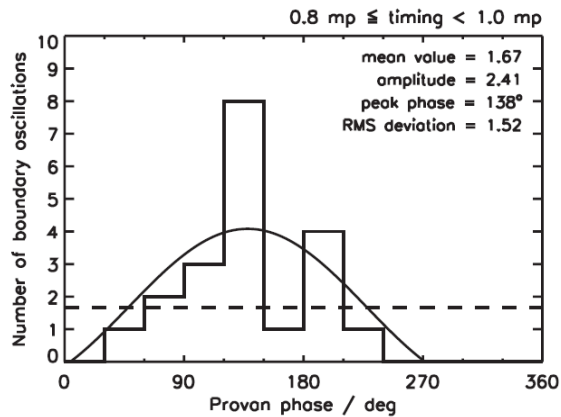
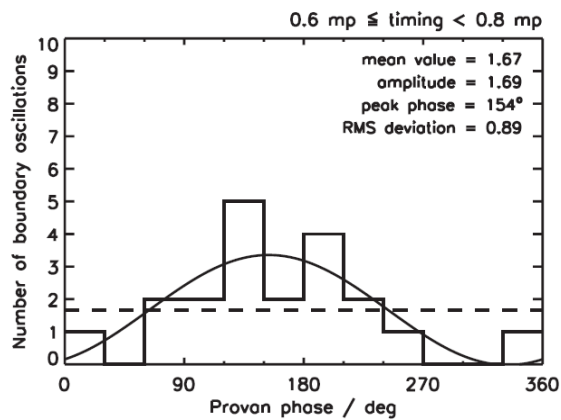
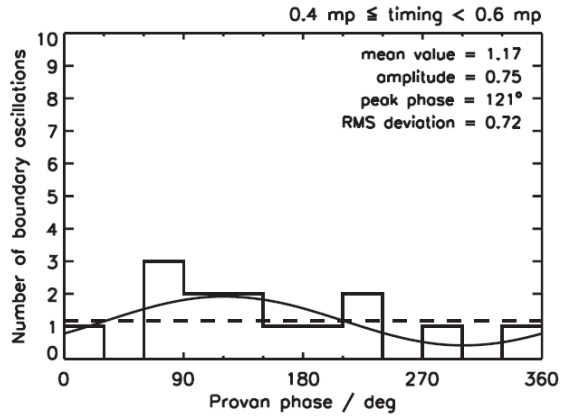


Figure 7.3 (continued overleaf) Histograms of the observed number of magnetopause oscillations versus Provan phase, with fitted sinusoids, for the set of six 0.2 magnetospheric period (mp) timing windows spanning 0.4 to 1.6 of the magnetospheric period. The data set is restricted to those orbits that cross both the magnetopause and the bow shock.

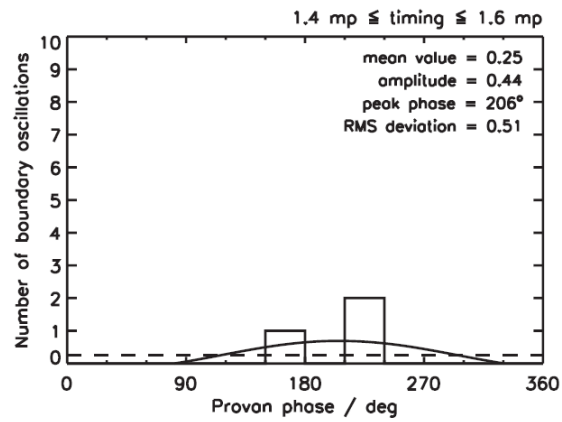
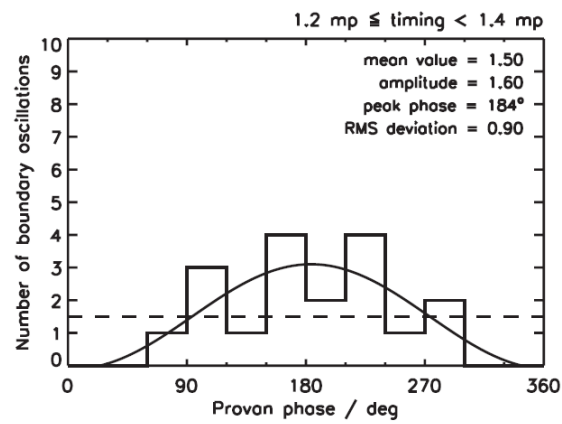
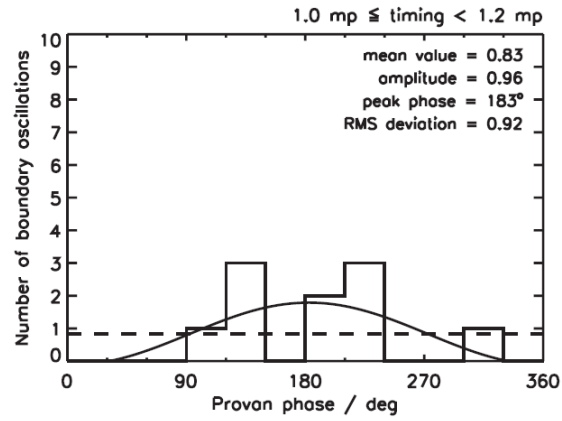


Figure 7.3 (continued from previous page)

plotted the resulting curves. The amplitudes, peak phases, and RMS deviations determined from the fits are given in the individual panels, along with the mean values (the number of oscillations averaged over the twelve 30° bins), the latter also being marked by horizontal dashed lines. (Because of the cyclical nature of the phase, fitting a sinusoid is a more appropriate method of estimating the peak phase than simply calculating the mean phase. However, we should note that in Figures 6.2 and 6.9c of Chapter 6 the distributions go to zero at the edges of the histograms, so the use of the mean as an estimate of the peak phase in that study is not problematic.) To allow direct comparison with the equivalent set of histograms for the bow shock (Figure 7.4, to be introduced below), the data set used in Figure 7.3 is restricted to those orbits that cross both the magnetopause and the bow shock.

Here we have applied the same technique as in Chapter 6 to the ensemble of bow shock encounters observed by Cassini during Revs SOI-55, to examine the extent to which the phasing of the bow shock motions within various timing windows are related to the Provan phase. The results are somewhat more scattered than for the magnetopause, in keeping with our comments in section 7.3 above, but phase organization is found to be present throughout the timing band between 0.6 and 1.6 of the magnetospheric period, with the strongest organization being found between 0.6 and 1.0 of that period. However, in contrast to the results for the magnetopause, no phase organization is found at all between 0.4 and 0.6 of the magnetospheric period. This can be seen in Figure 7.4 which shows histograms of the number of observed bow shock oscillations versus Provan phase, with fitted sinusoids, for the same set of six 0.2 magnetospheric period timing windows as used in Figure 7.3. We have thus adopted a timing window for bow shock oscillations between 0.6 and 1.6 of the magnetospheric period for the results discussed below, and in order to

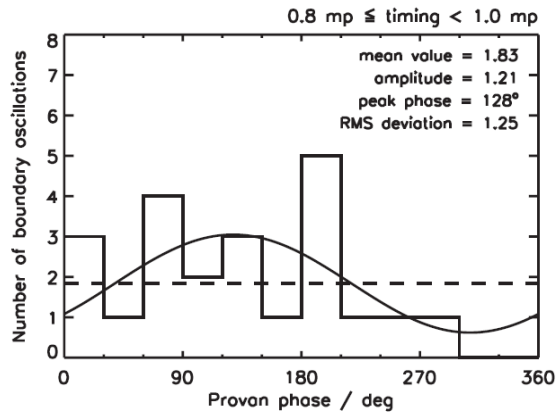
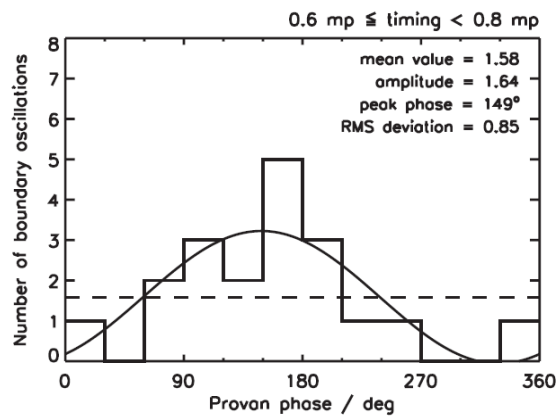
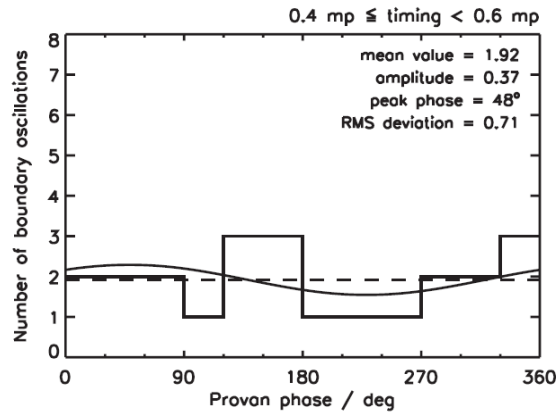


Figure 7.4 (continued overleaf) Histograms of the observed number of bow shock oscillations versus Provan phase, with fitted sinusoids, in the same format as Figure 7.3.

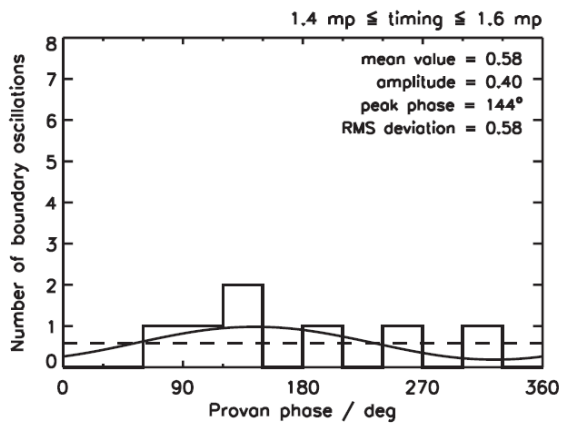
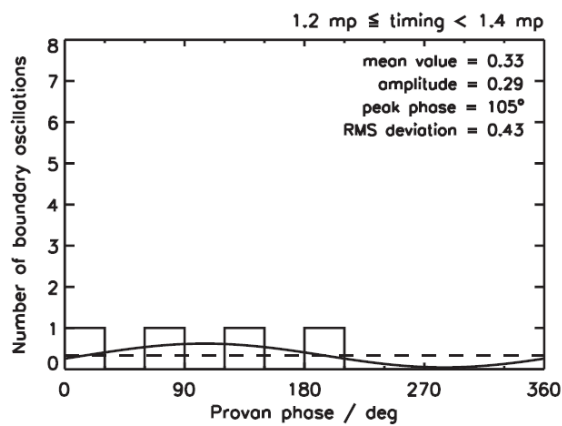
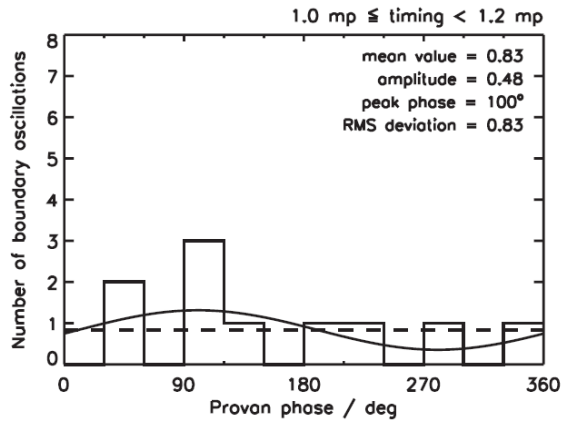


Figure 7.4 (continued from previous page)

make a close comparison with the magnetopause observations we have also re-analyzed the latter data using the same timing window criterion. For this reason we have also restricted our magnetopause data set to those spacecraft orbits which also crossed the bow shock at some point, thus excluding a number of orbits where the spacecraft crossed the magnetopause, but had insufficient radial range to reach the more distant bow shock, as mentioned previously in section 7.2.

This data set consists of 35 orbits during which 62 bow shock oscillations and 71 magnetopause oscillations were observed within the above timing window. We have then determined the Provan phase given by equation (6.1b) for each of these oscillation events, specifically for the centre time of the magnetosheath interval for the bow shock oscillations and the magnetosphere interval for the magnetopause oscillations, these being proxies for the time of maximum outward boundary excursion. The results are presented in Figure 7.5, where we show histograms of the number of oscillations occurring within 30° bins of Provan phase, the red line corresponding to the bow shock and the blue line to the magnetopause. It can be seen that both distributions are significantly peaked over similar ranges of Provan phase, demonstrating that both are related to the field and plasma oscillations inside the magnetosphere. It is also evident, however, that the distribution of bow shock phase values is somewhat broader than that of the magnetopause oscillations. If we consider the oscillation events that occur within the preferred 180° phase sector between 60° and 240° of both distributions (a sector that we note contains all of the phase values determined in Figures 7.1 and 7.2 for both bow shock and magnetopause), we find that for the bow shock 74% of the oscillations occur in this sector and 26% in the other 180° sector from 240° to 60° (via 360°), while for the magnetopause 89% occur in this

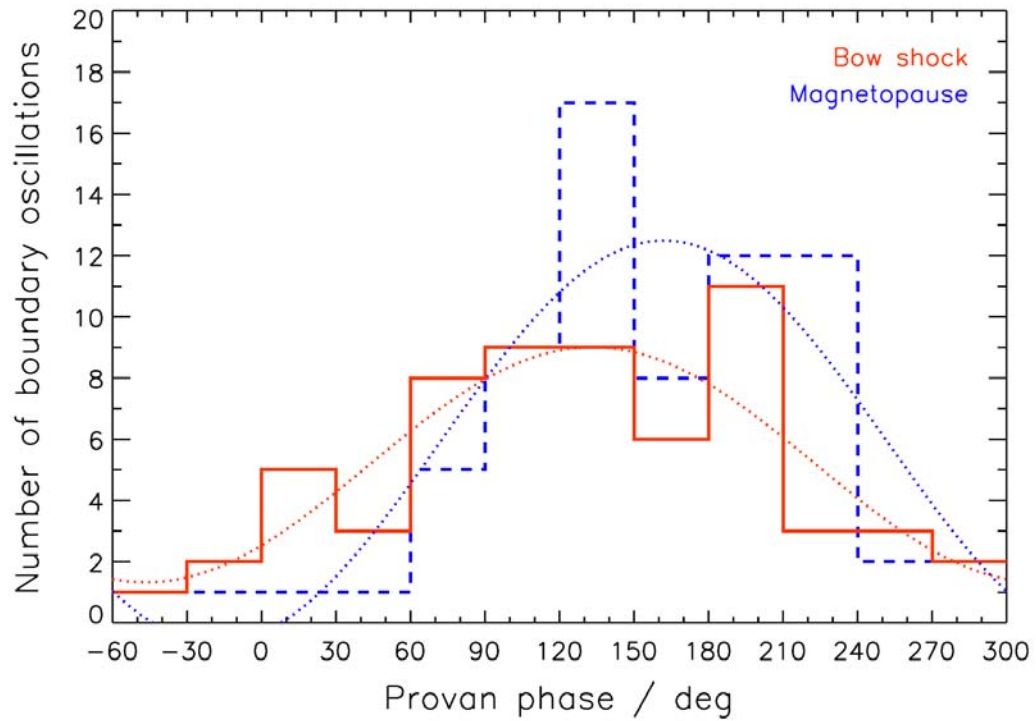


Figure 7.5 Histograms of the number of observed bow shock (red) and magnetopause (blue) oscillations versus Provan phase for an event timing window of 0.6 to 1.6 of the magnetospheric period, with least-squares sinusoid fits. The data set is restricted to those orbits that cross both boundaries.

preferred sector and 11% in the other sector. If the data set is further restricted in both cases to the timing window between 0.6 and 1.0 of the magnetospheric period, consisting of 41 bow shock oscillations and 40 magnetopause oscillations, we find that the phase organization within the preferred sector is marginally increased, such that 78% of the bow shock oscillations and 90% of the magnetopause oscillations occur in this sector (60° - 240°). Thus while these results show that the bow shock oscillations within the above timing windows are certainly organized by the Provan phase, hence proving the existence of magnetospheric period oscillations of the bow shock on a statistical basis, the degree of organization is rather less than that found for the magnetopause.

It is of interest to determine and compare the Provan phases Ψ_0 at which the histograms in Figure 7.5 peak. To do this we have least-squares fitted the histogram values to a sinusoid using the same method as for Figures 7.3 and 7.4, the fitted sinusoids being shown by the appropriately coloured curves in Figure 7.5. The uncertainty in the phase at the peak has been determined by computing the phase displacement away from the best-fit value that results in a significant 10 % increase in the RMS deviation of the fitted line from the histogram data. The resulting phases are $133^\circ \pm 17^\circ$ for the bow shock and $162^\circ \pm 15^\circ$ for the magnetopause, the latter being closely similar to the magnetopause value determined in Chapter 6. The difference between these values is $-29^\circ \pm 23^\circ$, which is essentially consistent with zero. For the sub-set of data within the restricted timing window between 0.6 and 1.0 of the magnetospheric period, the peak phase values are found to be $140^\circ \pm 19^\circ$ for the bow shock and $144^\circ \pm 21^\circ$ for the magnetopause, again consistent with in-phase behaviour within the estimated errors. The physical meaning of the result is that the quasi-uniform ‘core’ magnetic field is typically rotated $\sim 130^\circ - 160^\circ$ anti-clockwise (as

viewed from the north) from the instantaneous position of outward boundary maxima, thus pointing approximately away from the latter.

To take the comparison a step further, in Figure 7.6 we show the Provan phase of each observed bow shock (red) and magnetopause (blue) oscillation for the timing window between 0.6 and 1.6 of the magnetospheric period, plotted versus the local time at the centre of the oscillation. In this figure we now include data from five orbits that have magnetopause crossings but no bow shock crossings. The data have been divided into three 3 h local time bands centred on 6, 9, and 15 h LT where there are significant numbers of data values for both sets of oscillations, and the most probable phase values (with error estimates) have been calculated in the same manner as in Figure 7.5. These values are shown by the red and blue squares, from which it can be seen that the phase values for the LT bins centred on 6 and 15 h are equal within the error bars (typically about $\pm 25^\circ$), while for the bin centred on 9 h LT the difference lies marginally outside of the error bars. It can also be seen that the two phase values for the bin centred on 6 h LT on the dawn meridian both take somewhat larger values than those in the local time bands centred on 9 and 15 h LT either side of noon. As demonstrated in section 6.7 with respect to the magnetopause oscillations, this is due to the larger radial distance to the boundary with increasing azimuth from noon combined with the finite outward radial propagation speed of the oscillatory disturbances within the magnetosphere.

Overall, the above results demonstrate that the magnetospheric period oscillations of the bow shock are in phase with those of the magnetopause, within a phase uncertainty of about $\pm 25^\circ$. This result implies a sufficiently fast propagation of the oscillatory signal in the magnetosheath between the two boundaries. Since the separation of the boundaries in

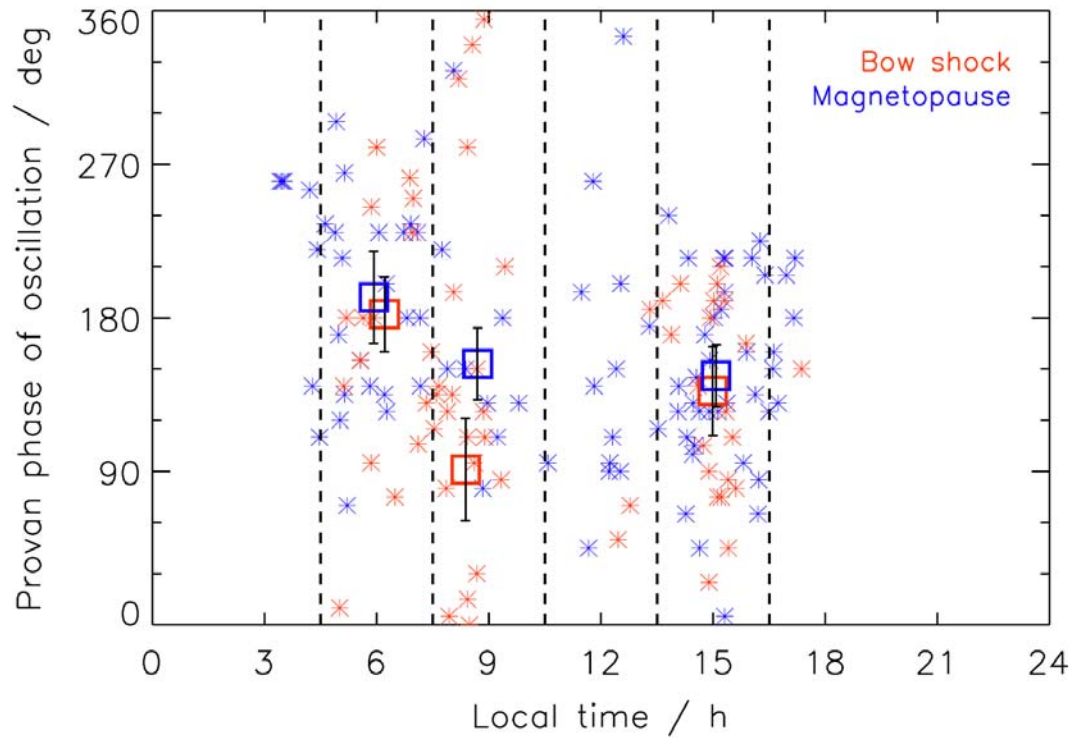


Figure 7.6 Plot of the Provan phase of the observed bow shock (red) and magnetopause (blue) oscillations versus local time for an event timing window of 0.6 to 1.6 of the magnetospheric period. In this figure we include data from five orbits that have magnetopause crossings but no bow shock crossings. The squares show peak phase values determined by least-squares sinusoid fits in the 3 h windows of local time (centred on 6, 9, and 15 h LT) marked by the vertical dashed lines.

the mid-morning and mid-afternoon LT hours corresponding to the majority of the data examined here (Figure 7.6) is $\sim 5\text{-}10 R_S$ (see Figure 7.7 to be introduced below), the implied outward propagation speed for approximately in-phase oscillations within the above phase uncertainty is at least $\sim 100\text{-}200 \text{ km s}^{-1}$. Physically, for slow motions of the magnetopause boundary as is the case here ($\sim 10\text{-}30 \text{ km s}^{-1}$ as estimated in section 6.8), we expect the signal to propagate through the magnetosheath at the magnetosonic speed. In the near sub-solar magnetosheath this speed will be some significant fraction of the upstream solar wind speed (the latter being typically $\sim 500 \text{ km s}^{-1}$), thus consistent with the lower limits for outward propagation of $\sim 100\text{-}200 \text{ km s}^{-1}$ estimated above. We note that the corresponding radial propagation speed of these signals in the magnetosphere is estimated to be $\sim 200\text{-}400 \text{ km s}^{-1}$ (section 6.7).

7.5 Occurrence and Amplitude of Bow Shock Oscillations

In this section we finally consider some implications of our findings for the occurrence and amplitude of the bow shock oscillations. In the corresponding discussion of magnetopause oscillations in Chapter 6, it was assumed that all of the oscillations observed within their timing window were associated with boundary oscillations at the magnetospheric period. This assumption was made on the basis that $\sim 90\%$ of their phase values fell within one ‘preferred’ 180° sector of Provan phase and only $\sim 10\%$ in the other, equivalent to the magnetopause result shown here (with modestly different timing window and orbit selection) in Figure 7.5. However, this argument has rather less force for the bow shock oscillations, since the percentage of observed oscillations whose phase falls within the preferred 180° sector, between 60° and 240° , is reduced to $\sim 75\%$, with $\sim 25\%$ in the

other sector. While the peaking in Provan phase within this sector is sufficient to show the presence of bow shock motion at the magnetospheric period on a statistical basis, it also suggests that not all of the observed oscillations within the timing window are so associated, though of course it is not possible to say which are and which are not on an individual basis. In order to take the discussion of occurrence and amplitude further, we thus introduce an additional element of event selection to consider only those oscillations that occur within the ‘preferred’ phase sector, on the basis that at least a majority of those cases are likely to be associated with the magnetospheric period oscillation. We apply this rule equally to both bow shock and magnetopause oscillations so that the results may be directly compared, though this produces only a marginal change in the more highly phase-peaked magnetopause data set.

We begin by noting that out of the total of 35 Cassini orbits that pass through the magnetosheath-solar wind boundary region, 22 are found to exhibit bow shock oscillations on either the outbound or inbound passes (falling both within the 0.6-1.6 magnetospheric period timing window and the preferred phase sector between 60° and 240°). Such oscillations are therefore found on $\sim 60\%$ of these orbits, thus representing a relatively commonly-observed phenomenon. Of the 22 orbits exhibiting such oscillations, 8 have one oscillation, 9 two oscillations, and 5 three or more (not necessarily consecutive). On these same 35 orbits, 25 exhibit magnetopause oscillations within the same timing window and preferred sector, i.e. $\sim 70\%$ of the orbits in this case. Of these, 12 have one oscillation, 4 two oscillations, and 9 three or more. In Chapter 6 we reported magnetopause oscillation occurrence results on the basis of individual passes through the magnetopause boundary region, but if analyzed on the same whole-orbit basis as adopted here, occurrence rises to

~85%. The ~70% value obtained here thus represents a modest reduction in magnetopause oscillation occurrence, resulting from the somewhat narrower timing window and preferred sector selection employed here, but still showing that it is a common phenomenon. Overall, our results thus show that bow shock oscillations near the magnetospheric period are commonly present, comparable in occurrence to the equivalent oscillations of the magnetopause.

The spatial distribution of the selected bow shock and magnetopause oscillations is shown in KSM coordinates in Figure 7.7 where, as in Figure 7.6, we show the magnetopause oscillations irrespective of whether the bow shock was crossed on a particular pass. KSM is the preferred system for bow shock and magnetopause studies, with X_{KSM} pointing towards the Sun (approximately opposite to the solar wind flow), the X_{KSM} - Z_{KSM} plane containing the planet's spin and magnetic axis, and Y_{KSM} completing the right-handed triad. The magnetopause and bow shock models of *Arridge et al.* [2006] and *Masters et al.* [2008] are expressed as figures of revolution about the X_{KSM} axis, and are plotted in Figure 7.7 in cylindrical ρ_{KSM} - X_{KSM} coordinates, where $\rho_{KSM} = \sqrt{Y_{KSM}^2 + Z_{KSM}^2}$, by the blue and green dashed lines, respectively. The inner pair of lines correspond to a solar wind dynamic pressure of 0.1 nPa, and the outer pair to 0.01 nPa, spanning the usual range. The trajectory of the spacecraft is shown by the grey dashed lines in the same cylindrical coordinates, plotted over the full tour employed here (SOI to Rev 55). Red segments of the trajectory correspond to boundary oscillations of the bow shock (upper panel) and the magnetopause (lower panel), and specifically show the whole of each $0^\circ - 360^\circ$ rotation of the Provan phase containing an observed oscillation, so that oscillations that are consecutive are shown by a continuous red line. It can be seen that

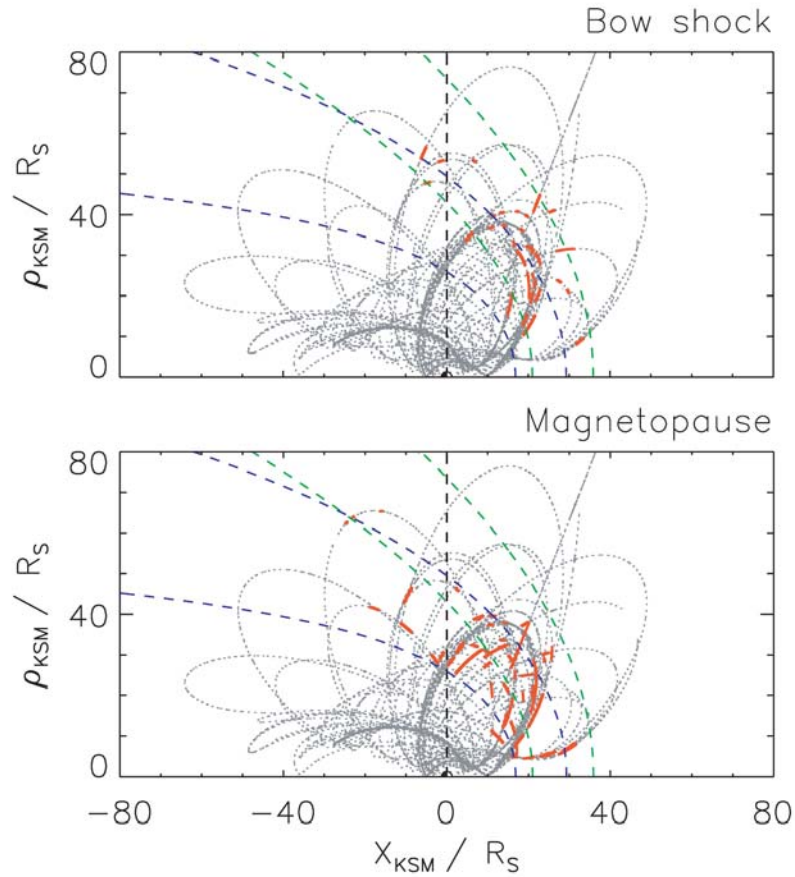


Figure 7.7 Plots showing the distribution of bow shock (upper panel) and magnetopause (lower panel) oscillations (red orbit segments) in cylindrical KSM coordinates where $\rho_{KSM} = \sqrt{Y_{KSM}^2 + Z_{KSM}^2}$, for an event timing window of 0.6 to 1.6 of the magnetospheric period and the ‘preferred’ 180° sector of Provan phase from 60° to 240°. The magnetopause model of *Arridge et al.* [2006] and bow shock model of *Masters et al.* [2008] are shown as blue and green dashed lines, respectively, the outer of each pair of lines corresponding to a solar wind dynamic pressure of 0.01 nPa and the inner to 0.1 nPa, spanning the usual range.

both bow shock and magnetopause oscillations are observed over essentially the whole range of locations that the spacecraft orbit crossed the expected position of these boundaries. This range corresponds to local times of 5-17 h for the bow shock and 3-17 h for the magnetopause (as also seen in Figure 7.6), and also to KSM latitudes between -18° and $+32^\circ$ for the bow shock and -36° and $+43^\circ$ for the magnetopause.

Finally with regard to the amplitude of the oscillations, we noted in section 6.8 that a lower limit to the peak-to-trough amplitude can be estimated from the spacecraft displacement normal to the model boundary surfaces between first and last contacts with the oscillating boundary (assuming that the boundary position is not affected by other processes during the interval in question). For our selected cases in which only a single boundary oscillation was observed (22 cases for the bow shock and 26 for the magnetopause), the mean displacements are found to be $0.9 R_S$ for the bow shock and $1.8 R_S$ for the magnetopause. With regard to the nature of the lower limit, the theoretical analysis presented in Chapter 5 (Figure 5.5 and Table 5.1) suggests that the displacement for single oscillations corresponds to roughly half the peak-to-trough boundary displacement, such that our results imply amplitudes of $\sim 0.8 R_S$ for the bow shock and $\sim 1.6 R_S$ for the magnetopause, the latter being consistent with the magnetopause results of Chapter 6. Thus both results imply typical amplitudes of order $\sim 1 R_S$, the significance of the difference between them remaining unclear. Correspondingly, for our selected cases in which two consecutive boundary oscillations were observed (6 cases for the bow shock and 8 for the magnetopause), the mean spacecraft displacements are found to be $2.5 R_S$ for the bow shock and $3.0 R_S$ for the magnetopause. The same theoretical analysis suggests that these values correspond to ~ 0.7 of the peak-to-trough boundary displacement, thus

consistently suggesting oscillation amplitudes of $\sim 2 R_S$ in both these cases. However, analysis of a few individual examples such as that shown in Figure 7.1 suggests that the amplitude can be significantly larger on occasion, possibly up to $4\text{-}5 R_S$ in the latter case, also in agreement with Chapter 6.

7.6 Summary

In this chapter we have employed magnetic field and plasma electron data from 35 Cassini orbits during 2004-2007 on which the spacecraft traversed the outer region of Saturn's environment from the magnetosphere to the solar wind, to present a first study of magnetospheric period oscillations of Saturn's bow shock, following the study of related magnetopause oscillations in Chapter 6. The principal results are as follows.

- (a) The phasing of bow shock oscillation events within a timing window between 0.6 and 1.6 of the magnetospheric period is found to be significantly organized by the phase of the magnetic field oscillations observed inside the magnetosphere [Provan *et al.*, 2009a], thus showing the presence of bow shock oscillations at the magnetospheric period. The degree of organization is somewhat weaker than the corresponding effect for the magnetopause, with 74% of these events falling within the preferred 180° Provan phase band between 60° and 240° , compared with 89% for the magnetopause. The corresponding figures for the more restricted timing window between 0.6 and 1.0 of the magnetospheric period are 78% and 90%.
- (b) The value of the Provan phase at the peak of the bow shock oscillation distribution is $133^\circ \pm 17^\circ$ for the timing window between 0.6 and 1.6 of the magnetospheric period,

compared with $162^\circ \pm 15^\circ$ for the magnetopause within the same timing window (the latter value being essentially the same as that reported in Chapter 6). These values are essentially equal to each other within the errors. The corresponding values for the timing window between 0.6 and 1.0 of the magnetospheric period are $140^\circ \pm 19^\circ$ for the bow shock and $144^\circ \pm 21^\circ$ for the magnetopause, again essentially equal. The bow shock and magnetopause thus oscillate in phase to within the established phase uncertainties of about $\pm 25^\circ$, thus implying signal propagation speeds across the magnetosheath of at least $\sim 100\text{-}200 \text{ km s}^{-1}$. The values of the phase at the peak of the distributions indicate that the quasi-uniform field within the ‘core’ region is rotated $\sim 130^\circ\text{--}160^\circ$ anti-clockwise (as viewed from the north) of the instantaneous location of outward boundary excursion maxima.

(c) Bow shock oscillations are commonly observed on Cassini orbits that cross the boundary region, with $\sim 60\%$ of such orbits showing one or more oscillations within the timing window between 0.6 and 1.6 of the magnetospheric period and within the preferred 180° phase sector from 60° to 240° . These events are observed at all locations at which the boundary was encountered by the spacecraft, from 5-17 h in local time and between -18° and $+32^\circ$ in KSM latitude.

(d) The data are consistent with the amplitudes of both bow shock and magnetopause oscillations being typically $\sim 1\text{--}2 R_S$, though evidence has also been presented of significantly larger values in the post-noon sector ($\sim 4\text{--}5 R_S$) on occasion.

Chapter 8

Summary and Future Work

In this thesis we have shown that the positions of Saturn's magnetopause and bow shock are modulated at a period near that of planetary rotation that we term the 'magnetospheric period'.

8.1 Background

Despite the fact that Saturn's internally-generated magnetic field is closely symmetric about the planet's spin axis [e.g. *Connerney et al.*, 1982; *Davis and Smith*, 1990; *Dougherty et al.*, 2005; *Giampieri et al.*, 2006], strong oscillatory phenomena near the planetary rotation period are nevertheless observed throughout the magnetosphere. These include 'strobe-like' variations in the power of Saturn kilometric radiation (SKR) emitted by auroral electrons [e.g. *Kaiser et al.*, 1980; *Zarka*, 1998], together with a rotating pattern of perturbations in the magnetic field and plasma particle fluxes that results in oscillations at a given position with a closely similar synodic period [e.g. *Espinosa et al.*, 2003a; *Carbary et al.*, 2007b, 2008a; *Andrews et al.*, 2008; *Southwood and Kivelson*, 2007; *Burch et al.*, 2009; *Provan et al.*, 2009a]. In particular, within the quasi-dipolar 'core' region of the magnetosphere, on magnetic shells with equatorial distances lying within $\sim 15 R_S$ of the planet, the equatorial oscillatory field takes the form of a quasi-uniform field of a few nT amplitude that rotates in the same sense as the planet. The SKR power is found to peak when this field points radially outward in the post-midnight sector. Evidence for outward radial propagation of the field and plasma effects has also been found in these data, such

that the oscillation ‘phase fronts’ spiral slowly outward from the planet [Cowley *et al.*, 2006; Gurnett *et al.*, 2007; Carbary *et al.*, 2007c; Andrews *et al.*, 2010]. It has also been found that the period of these oscillations is not strictly constant, but varies by $\sim 1\%$ on few year time scales [e.g. Galopeau and Lecacheux, 2000; Gurnett *et al.*, 2005; Kurth *et al.*, 2007, 2008]. The oscillations cannot therefore be tied directly to the rotation period of the planet, and are hence referred to here as ‘magnetospheric period’ oscillations. It should be noted that it has recently been discovered that there are two distinct SKR periods, one northern, the other southern [Kurth *et al.*, 2008; Gurnett *et al.*, 2009]. The work in this thesis relates to the southern hemisphere period which was dominant in the equatorial region during the southern summer conditions pertaining during 2004-2007. The first evidence for magnetospheric period oscillations of the magnetopause was presented by Espinosa and Dougherty [2001] and Espinosa *et al.* [2003a] who reported that during the outbound portion of the Pioneer-11 flyby the position of the magnetopause was modulated in phase with the radial component of the perturbation magnetic field. They suggested that the boundary oscillations were in response to variations in the total pressure (combined magnetic and plasma pressure) within the magnetosphere.

8.2 Summary

In this thesis we have presented four studies, three of which are data-based (Chapters 4, 6, and 7) and one theoretical (Chapter 5). The data-based studies use magnetic data from the Cassini orbiter’s fluxgate magnetometer (FGM), together with plasma electron data obtained by the spacecraft’s electron spectrometer instrument (ELS).

In Chapter 4, in a study based on the first ~ 20 Cassini orbits, we use data from two orbits to exemplify our discovery that Saturn's magnetopause oscillates at the magnetospheric period in response to changes in the total magnetospheric pressure. The amplitude of the boundary oscillations mapped to the planet-Sun line is estimated to be typically $\sim 1 R_S$ (expressed in the chapter as the peak-to-trough amplitude, $\sim 2 R_S$), corresponding to a $\sim 10\%$ change in the boundary radius. The change in internal pressure required to produce such motions is estimated to be $\sim 30 - 40\%$ of the background values and hence $\sim 30 - 40\%$ of the solar wind dynamic pressure.

In Chapter 5 we develop a simple theoretical model of motion through an oscillating planar boundary that is equally applicable to the magnetopause and the bow shock. One important result of our analysis is that, while the observed interval between successive like crossings of the boundary depends on spacecraft motion through the boundary region, it should always be shorter than the magnetospheric period. In reality, the boundary is subject to a number of processes that can lengthen or shorten the observed interval, therefore we employ fairly broad timing windows for event selection in Chapters 6 and 7.

In Chapter 6 we use data from ~ 40 Cassini orbits that crossed Saturn's magnetopause during 2004-2007 to make a first systematic study of the magnetospheric period oscillations of the magnetopause. Boundary oscillation events were selected for analysis using a timing window between 0.4 and 1.6 of the magnetospheric period. These events are found to be highly organized by the phase of the interior field oscillations, showing that they relate to boundary oscillations that have a closely common period. We find that $\sim 60\%$ of passes through the boundary region show one or more such oscillations. The oscillations are observed at all local times at which Cassini crossed the

magnetopause and over a range of latitudes, and are thus a global phenomenon. The phasing of the boundary oscillations is such that the rotating quasi-uniform equatorial field within the quasi-dipolar ‘core’ magnetosphere points approximately away from the maximum outward boundary displacement. However, the boundary oscillation phase is found to depend somewhat on radial distance to the magnetopause, consistent with outward radial propagation in the magnetosphere at phase speeds of $\sim 250 \text{ km s}^{-1}$. After taking account of the radial propagation, analysis shows that the phase of maximum outward boundary displacement is directly related to the phase of the density maximum in the Enceladus torus observed by *Gurnett et al.* [2007]. The oscillation amplitude is estimated typically to be $\sim 1.2 R_S$ (this being consistent with the findings of Chapter 4), but sometimes reaches $\sim 2 - 3 R_S$, and is occasionally as great as $\sim 4 - 5 R_S$. (Note that these amplitudes, and those obtained in Chapter 7, are not mapped to the planet-Sun line.)

As the magnetopause represents the effective obstacle around which the solar wind must flow, oscillations of the magnetopause should produce corresponding motions of the bow shock. In Chapter 7 we use data from 35 Cassini orbits on which the spacecraft crossed Saturn’s magnetopause and bow shock during 2004-2007 to provide first evidence for magnetospheric period bow shock oscillations. Two case studies are presented showing both bow shock and magnetopause oscillations on given spacecraft passes, together with a statistical study showing that bow shock oscillations observed within a timing window between 0.6 and 1.6 of the magnetospheric period are significantly organized by the phase of the interior field oscillations. (There is no evidence of such organization between 0.4 and 0.6 of the magnetospheric period.) Both case and statistical studies indicate that the bow shock and magnetopause oscillate approximately in phase, within a phase uncertainty

of about $\pm 25^\circ$. The overall data set suggests that bow shock oscillations are commonly observed over the whole local time range that the spacecraft crossed the boundary with typical amplitudes of $\sim 1-2 R_S$, comparable to results found previously for the corresponding oscillations of the magnetopause.

8.3 Future Work

We finally note that additional avenues of exploration of these phenomena are open for future studies, beyond those considered here.

It can be seen from Figure 6.14 in Chapter 6 that the propagating perturbations in the boundary positions should also be accompanied by associated tilting of the boundary normals, directed eastward of the average as the boundary moves outward, and westward as it moves inward, associated with the eastward phase motion of the disturbance. We note that this is opposite to the behaviour expected for Kelvin-Helmholtz disturbances propagating anti-sunward around the boundary in the dawn sector, but is in the same direction as the latter in the dusk sector. However, due to the very large length scales of the displacements along the boundaries (see Figure 6.14), these tilts are expected to be small, and may be difficult to detect in the presence of other shorter-scale phenomena.

The nature of the pressure perturbations in the outer magnetosphere and in the magnetosheath also merits further investigation, for example the relative importance of perturbations in the plasma and magnetic field pressures in producing the boundary motions. The analysis of internal pressure changes in Chapter 4 was not developed in further work because of the lack of ion pressure data, but these values are now becoming available.

In Chapter 7 we find that the bow shock and magnetopause oscillate in phase to within uncertainties of about $\pm 25^\circ$. However, the value of the Provan phase at the peak of the oscillation distribution is somewhat earlier for the bow shock than for the magnetopause. While this unexpected result may be an artefact of our analysis, we may also note here that it would be consistent with a signal that propagates through the magnetosheath from earlier to later local times.

We may speculate that the instances of (apparently) very large amplitude magnetopause and bow shock oscillations noted in Chapters 6 and 7 may occur at times when the outer magnetosphere plasma ‘bulge’ of *Burch et al.* [2009] is enhanced, presumably as the result of particularly high outgassing rates at Enceladus. This issue certainly merits further investigation, although it should be acknowledged that we cannot exclude the possibility that such cases within our data set may be affected by solar wind-induced motions of the boundary that partially match the spacecraft motion and therefore lead to overestimates of the oscillation amplitude.

A recent study by *Andrews et al.* [Magnetospheric period oscillations at Saturn: Comparison of equatorial and high-latitude magnetic field periods with north and south SKR periods, manuscript submitted to *J. Geophys. Res.* in May 2010] has shown that two systems of magnetic field oscillations are present at Saturn with periods that are closely similar to those of the modulated SRK emission originating in the northern and southern hemispheres (~ 10.6 h and ~ 10.8 h respectively). These observations indicate the presence of physically distinct northern and southern hemisphere current systems, each with an associated effective dipole, that rotate at these two different periods. (Note that these findings somewhat modify the account given in section 2.2.) The two systems remain

separate at high latitudes but are superposed in the equatorial region where the southern period is dominant as assumed throughout this thesis. The dominance of the southern hemisphere system in low-latitude data obtained before equinox (August 2009) may be attributed to the southern summer conditions then prevailing. Analysis of data obtained after equinox is necessary to determine whether the northern hemisphere system will become dominant under conditions of northern hemisphere summer.

Most importantly, the overall physical origins of these oscillatory phenomena, resulting in such highly coordinated rotating plasma and field perturbations throughout Saturn's magnetosphere, remain to be determined.

Appendix

Derivation of the expression for the timescale on which the displaced magnetopause moves back to equilibrium, as used in section 4.4

We recall from section 1.3 that the magnetopause standoff distance R_{MP} is determined by pressure balance at the boundary. If magnetospheric plasma pressure is neglected, the equilibrium condition at the subsolar magnetopause can be represented as

$$\rho V_{SW}^2 \approx \frac{2B_{eq}^2}{\mu_0} \left(\frac{R_p}{R_{MP}} \right)^6, \quad (\text{A1})$$

where ρ is the solar wind mass density, V_{SW} is the solar wind bulk flow speed, B_{eq} is the effective equatorial field of the planet, and R_p is the radius of the planet.

If we suppose that the magnetopause is for some reason displaced inward (say) to some new radius R'_{MP} , the field pressure inside the boundary will now be larger than ρV_{SW}^2 and so the boundary will move outwards at speed V_B . The boundary speed is determined by the requirement of equilibrium in the boundary frame of reference. The effective bulk flow speed of the solar wind is $(V_{SW} + V_B)$ and the equilibrium condition can be written as

$$\rho (V_{SW} + V_B)^2 \approx \frac{2B_{eq}^2}{\mu_0} \left(\frac{R_p}{R'_{MP}} \right)^6. \quad (\text{A2a})$$

The boundary speed is given by

$$V_B = \frac{dR'_{MP}}{dt} \approx \left(\frac{2B_{eq}^2}{\mu_0 \rho} \left(\frac{R_p}{R'_{MP}} \right)^6 \right)^{\frac{1}{2}} - V_{SW} \quad (\text{A2b})$$

$$\approx V_{SW} \left(\left(\frac{R_{MP}}{R'_{MP}} \right)^3 - 1 \right) . \quad (\text{A2c})$$

Making the substitutions $r = \frac{R'_{MP}}{R_{MP}}$ and $\tau = \frac{t}{R_{MP}} V_{SW}$ then yields

$$\frac{dr}{d\tau} \approx \frac{1-r^3}{r^3} . \quad (\text{A3a})$$

Because we are considering small displacements, we can write

$$r = 1 + \delta r(t) . \quad (\text{A3b})$$

Substituting for r in equation (A3a) and linearizing gives

$$\frac{d}{d\tau}(\delta r) \approx -3\delta r(t) , \quad (\text{A3c})$$

which on integration yields

$$\delta r \approx \delta r_0 e^{-3\tau} . \quad (\text{A3d})$$

Magnetopause displacements thus suffer exponential decay on a timescale

$$T_{MP} \approx \frac{R_{MP}}{3V_{SW}} . \quad (\text{A4})$$

References

- Achilleos, N., C.S. Arridge, C. Bertucci, C.M. Jackman, M.K. Dougherty, K.K. Khurana, and C.T. Russell (2008), Large-scale dynamics of Saturn's magnetopause: Observations by Cassini, *J. Geophys. Res.*, *113*, A11209, doi:10.1029/2008JA013265.
- Achilleos, N., P. Guio, and C.S. Arridge (2009), A model of force balance in Saturn's magnetodisc, *Mon. Not. R. Astron. Soc.*, *401*, 2349-2371, doi:10.1111/j.1365-2966.2009.15865.x.
- Aellig, M.R., A.J. Lazarus, and J.T. Steinberg (2001), The solar wind helium abundance: Variation with wind speed and the solar cycle, *Geophys. Res. Lett.*, *28*, 14, 2767-2770.
- Andrews, D.J., E.J. Bunce, S.W.H. Cowley, M.K. Dougherty, G. Provan, and D.J. Southwood (2008), Planetary period oscillations in Saturn's magnetosphere: Phase relation of equatorial magnetic field oscillations and SKR modulation, *J. Geophys. Res.*, *113*, A09205, doi:10.1029/2007JA012937.
- Andrews, D.J., S.W.H. Cowley, M.K. Dougherty, and G. Provan (2010), Magnetic field oscillations near the planetary period in Saturn's equatorial magnetosphere: Variation of amplitude and phase with radial distance and local time, *J. Geophys. Res.*, *115*, A04212, doi:10.1029/2009JA014729.
- Arridge, C.S., N. Achilleos, M.K. Dougherty, K.K. Khurana, and C.T. Russell (2006), Modeling the size and shape of Saturn's magnetopause with variable dynamic pressure, *J. Geophys. Res.*, *111*, A11227, doi:10.1029/2005JA011574.

- Bridge, H.S., et al. (1982), Plasma observations near Saturn: Initial results from Voyager 2, *Science*, 215, 563.
- Bunce, E.J., and S.W.H. Cowley (2001), Local time asymmetry of the equatorial current sheet in Jupiter's magnetosphere, *Planet. Space Sci.*, 49, 261-274.
- Bunce, E.J., S.W.H. Cowley, I.I. Alexeev, C.S. Arridge, M.K. Dougherty, J.D. Nichols, and C.T. Russell (2007), Cassini observations of the variation of Saturn's ring current parameters with system size, *J. Geophys. Res.*, 112, A10202, doi:10.1029/2007JA012275.
- Bunce, E.J., C.S. Arridge, S.W.H. Cowley, and M.K. Dougherty (2008a), Magnetic field structure of Saturn's dayside magnetosphere and its mapping to the ionosphere: Results from ring current modeling, *J. Geophys. Res.*, 113, A02207, doi:10.1029/2007JA012538.
- Bunce, E.J., et al. (2008b), Origins of Saturn's aurora: Simultaneous observations by Cassini and the Hubble Space Telescope, *J. Geophys. Res.*, 113, A09209, doi:10.1029/2008JA013257.
- Burch, J.L., J. Goldstein, P. Mokashi, W.S. Lewis, C. Paty, D.T. Young, A.J. Coates, M.K. Dougherty, and N. André (2008), On the cause of Saturn's plasma periodicity, *Geophys. Res. Lett.*, 35, L14105, doi:10.1029/2008GL034951.
- Burch, J.L., A.D. DeJong, J. Goldstein, and D.T. Young (2009), Periodicity in Saturn's magnetosphere: Plasma cam, *Geophys. Res. Lett.*, 36, L14203, doi:10.1029/2009GL039043.

- Burton, M.E., B. Buratti, D.L. Matson, and J.-P. Lebreton (2001), The Cassini/Huygens Venus and Earth flybys: An overview of operations and results, *J. Geophys. Res.*, *106*, A12, 30099-30107.
- Burton, M.E., M.K. Dougherty, and C.T. Russell (2009), Model of Saturn's internal planetary magnetic field based on Cassini observations, *Planet. Space Sci.*, *57*, 1706-1713.
- Carbary, J.F., and S.M. Krimigis (1982), Charged particle periodicity in the Saturnian magnetosphere, *Geophys. Res. Lett.*, *9*, 1073-1076.
- Carbary, J.F., D.G. Mitchell, S.M. Krimigis, and N. Krupp (2007a), Electron periodicities in Saturn's outer magnetosphere, *J. Geophys. Res.*, *112*, A03206, doi:10.1029/2006JA012077.
- Carbary, J.F., D.G. Mitchell, S.M. Krimigis, D.C. Hamilton, and N. Krupp (2007b), Charged particle periodicities in Saturn's outer magnetosphere, *J. Geophys. Res.*, *112*, A06246, doi:10.1029/2007JA012351.
- Carbary, J.F., D.G. Mitchell, S.M. Krimigis, and N. Krupp (2007c), Evidence for spiral pattern in Saturn's magnetosphere using the new SKR longitudes, *Geophys. Res. Lett.*, *34*, L13105, doi:10.1029/2007GL030167.
- Carbary, J.F., D.G. Mitchell, S.M. Krimigis, D.C. Hamilton, and N. Krupp (2007d), Spin-period effects in magnetospheres with no axial tilt, *Geophys. Res. Lett.*, *34*, L18107, doi:10.1029/2007GL030483.
- Carbary, J.F., D.G. Mitchell, P. Brandt, C. Paranicas, and S.M. Krimigis (2008a), ENA periodicities at Saturn, *Geophys. Res. Lett.*, *35*, L07102, doi:10.1029/2008GL033230.

- Carbary, J.F., D.G. Mitchell, P. Brandt, E.C. Roelof, and S.M. Krimigis (2008b), Periodic tilting of Saturn's plasma sheet, *Geophys. Res. Lett.*, *35*, L24101, doi:10.1029/2008GL036339.
- Connerney, J.E.P., N.F. Ness, and M.H. Acuña (1982), Zonal harmonic model of Saturn's magnetic field from Voyager 1 and 2 observations, *Nature*, *298*, 44-46.
- Connerney, J.E.P. (1993), Magnetic fields of the outer planets, *J. Geophys. Res.*, *98*, 18,659-18,679.
- Connerney, J.E.P., M.H. Acuña, N.F. Ness, T. Satoh (1998), New models of Jupiter's magnetic field constrained by the Io flux tube footprint, *J. Geophys. Res.*, *103*, 11,929-11,939.
- Cowley, S.W.H. (1991), The plasma environment of the Earth, *Contemp. Phys.*, *32*, 235-250.
- Cowley, S.W.H., D.M. Wright, E.J. Bunce, A.C. Carter, M.K. Dougherty, G. Giampieri, J.D. Nichols, and T.R. Robinson (2006), Cassini observations of planetary-period magnetic field oscillations in Saturn's magnetosphere: Doppler shifts and phase motion, *Geophys. Res. Lett.*, *33*, L07104, doi:10.1029/2005GL025522.
- Cowling, T.G. (1934), The magnetic field of sunspots, *Mon. Not. R. Astron. Soc.*, *94*, 39-48.
- Cowling, T.G. (1955), Dynamo theories of cosmic magnetic fields, *Vistas in Astronomy*, *1*, 313-322.
- Davis, L., Jr., and E.J. Smith (1990), A model of Saturn's magnetic field based on all available data, *J. Geophys. Res.*, *95*, 15,257-15,261.

- De Keyser, J., et al. (2005), Magnetopause and boundary layer, *Space Sci. Rev.*, *118*, 231-320, doi:10.1007/s11214-005-3834-1.
- Desch, M.D., and M.L. Kaiser (1981), Voyager measurement of the rotation period of Saturn's magnetic field, *Geophys. Res. Lett.*, *8*, 253-256.
- Dougherty, M.K., et al. (2004), The Cassini magnetic field investigation, *Space Sci. Rev.*, *114*, 331-383, doi:10.1007/s11214-004-1432-2.
- Dougherty, M.K., et al. (2005), Cassini magnetometer observations during Saturn orbit insertion, *Science*, *307*, 1266-1270, doi:10.1126/science.1106098.
- Espinosa, S.A., and M.K. Dougherty (2000), Periodic perturbations in Saturn's magnetic field, *Geophys. Res. Lett.*, *27*, 2785-2788.
- Espinosa, S.A., and M.K. Dougherty (2001), Unexpected periodic perturbations in Saturn's magnetic field data from Pioneer 11 and Voyager 2, *Adv. Space Res.*, *28*, 919-924.
- Espinosa, S.A., D.J. Southwood, and M.K. Dougherty (2003a), Reanalysis of Saturn's magnetospheric field data view of spin-periodic perturbations, *J. Geophys. Res.*, *108*(A2), 1085, doi:10.1029/2001JA005083.
- Espinosa, S.A., D.J. Southwood, and M.K. Dougherty (2003b), How can Saturn impose its rotation period in a non-corotating magnetosphere?, *J. Geophys. Res.*, *108*(A2), 1086, doi:10.1029/2001JA005084.
- Feldman, W.C., J.R. Asbridge, S.J. Bame, and J.T. Gosling (1978), Long-term variations of selected solar wind properties: Imp 6, 7, and 8 results, *J. Geophys. Res.*, *83*, A5, 2177-2189.

- Galopeau, P.H.M., P. Zarka, and D. LeQuéau (1995), Source location of Saturn's kilometric radiation: The Kelvin-Helmholtz instability hypothesis, *J. Geophys. Res.*, *100*, 26,397-26,410.
- Galopeau, P.H.M., and A. Lecacheux (2000), Variations of Saturn's radio rotation period measured at kilometer wavelengths, *J. Geophys. Res.*, *105*, 13,089-13,101.
- Giampieri, G., M.K. Dougherty, E.J. Smith, and C.T. Russell (2006), A regular period for Saturn's magnetic field that may track its internal rotation, *Nature*, *441*, 62-64, doi:10.1038/nature04750.
- Gosling, J.T., and V.J. Pizzo (1999), Formation and evolution of corotating interaction regions and their three dimensional structure, *Space Sci. Rev.*, *89*, 21-52.
- Gurnett, D.A., et al. (2005), Radio and plasma wave observations at Saturn from Cassini's approach and first orbit, *Science*, *307*, 1255-1259, doi:10.1126/science.1105356.
- Gurnett, D.A., A.M. Persoon, W.S. Kurth, J.B. Groene, T.F. Averkamp, M.K. Dougherty, and D.J. Southwood (2007), The variable rotation period of the inner region of Saturn's plasma disk, *Science*, *316*, 442-445, doi:10.1126/science.1138562.
- Gurnett, D.A., A. Lecacheux, W.S. Kurth, A.M. Persoon, J.B. Groene, L. Lamy, P. Zarka, and J.F. Carbary (2009), Discovery of a north-south asymmetry in Saturn's radio rotation period, *Geophys. Res. Lett.*, *36*, L16102, doi:10.1029/2009GL039621.
- Huddleston, D.E., C.T. Russell, M.G. Kivelson, K.K. Khurana, and L. Bennett (1998), Location and shape of the Jovian magnetopause and bow shock, *J. Geophys. Res.*, *103*, 20075-20082.

- Hundhausen, A.J. (1995), The solar wind, in *Introduction to Space Physics*, edited by M.G. Kivelson and C.T. Russell, 91-128, Cambridge University Press, Cambridge, UK.
- Jackman, C.M., R.J. Forsyth, and M.K. Dougherty (2008), The overall configuration of the interplanetary magnetic field upstream of Saturn as revealed by Cassini observations, *J. Geophys. Res.*, *113*, A08114, doi:10.1029/2008JA013083.
- Joy, S.P., M.G. Kivelson, R.J. Walker, K.K. Khurana, C.T. Russell, and T. Ogino (2002), Probabilistic models of the Jovian magnetopause and bow shock locations, *J. Geophys. Res.*, *107*, doi:10.1029/2001JA009146.
- Jones, G.H., et al. (2006), Enceladus' varying imprint on the magnetosphere of Saturn, *Science*, *311*, 1412-1415, doi:10.1126/science.1121011.
- Kaiser, M.L., M.D. Desch, J.W. Warwick, and J.B. Pearce (1980), Voyager detection of non-thermal radio emission from Saturn, *Science*, *209*, 1238-1240.
- Kanani, S.J., et al. (2010), A new form of Saturn's magnetopause using a dynamic pressure balance model, based on in-situ, multi-instrument Cassini measurements, *J. Geophys. Res.*, in press, doi:10.1029/2009JA014262.
- Kellett, S., E.J. Bunce, A.J. Coates, and S.W.H. Cowley (2009), Thickness of Saturn's ring current determined from north-south Cassini passes through the current layer, *J. Geophys. Res.*, *114*, A04209, doi:10.1029/2008JA013942.
- Kellett, S., C.S. Arridge, E.J. Bunce, A.J. Coates, S.W.H. Cowley, M.K. Dougherty, A.M. Persoon, N. Sergis, and R.J. Wilson (2010), Nature of the ring current in Saturn's dayside magnetosphere, *J. Geophys. Res.*, in press, doi:10.1029/2009JA015146.

- Khurana, K.K., D.G. Mitchell, C.S. Arridge, M.K. Dougherty, C.T. Russell, C. Paranicas, N. Krupp, and A.J. Coates (2009), Sources of rotating signals in Saturn's magnetosphere, *J. Geophys. Res.*, *114*, A02211, doi:10.1029/2008JA013312.
- Kivelson, M.G., and D.J. Southwood (2003), First evidence of IMF control of Jovian magnetospheric boundary locations: Cassini and Galileo magnetic field measurements compared, *Planet. Space Sci.*, *51*, 891-898.
- Krimigis, S.M., et al. (2005), Dynamics of Saturn's magnetosphere from MIMI during Cassini's orbital insertion, *Science*, *307*, 1270-1273, doi:10.1126/science.1105978.
- Krupp, N., et al. (2005), The Saturnian plasma sheet as revealed by energetic particle measurements, *Geophys. Res. Lett.*, *32*, L20S03, doi:10.1029/2005GL022829.
- Kurth, W.S., A. Lecacheux, T.F. Averkamp, J.B. Groene, and D.A. Gurnett (2007), A Saturn longitude system based on a variable kilometric radiation period, *Geophys. Res. Lett.*, *34*, L02201, doi:10.1029/2006GL028336.
- Kurth, W.S., T.F. Averkamp, D.A. Gurnett, J.B. Groene, and A. Lecacheux (2008), An update to a Saturn longitude system based on kilometric radio emissions, *J. Geophys. Res.*, *113*, A05222, doi:10.1029/2007JA012861.
- Lecacheux, A., and F. Genova (1983), Source location of Saturn kilometric radio emission, *J. Geophys. Res.*, *88*, 8993-8998.
- Lepping, R.P., L.F. Burlaga, and L.W. Klein (1981), Surface waves on Saturn's magnetopause, *Nature*, *292*, 750-753.

- Masters, A., N. Achilleos, M.K. Dougherty, J.A. Slavin, G.B. Hospodarsky, C.S. Arridge, and A.J. Coates (2008), An empirical model of Saturn's bow shock: Cassini observations of shock location and shape, *J. Geophys. Res.*, *113*, A10210, doi:10.1029/2008JA013276.
- Masters, A., N. Achilleos, C. Bertucci, M.K. Dougherty, S.J. Kanani, C.S. Arridge, H.J. McAndrews, and A.J. Coates (2009), Surface waves on Saturn's dawn flank magnetopause driven by the Kelvin-Helmholtz instability, *Planet. Space Sci.*, *57*, 1769-1778.
- McAndrews, H.J., C.J. Owen, M.F. Thomsen, B. Lavraud, A.J. Coates, M.K. Dougherty, and D.T. Young (2008), Evidence for reconnection at Saturn's magnetopause, *J. Geophys. Res.*, *113*, A04210, doi:10.1029/2007JA012581.
- McAndrews, H.J., et al. (2009), Plasma in Saturn's nightside magnetosphere and the implications for global circulation, *Planet. Space Sci.*, *57*, 1714-1722.
- Nichols, J.D., J.T. Clarke, S.W.H. Cowley, J. Duval, A.J. Farmer, J.-C. Gérard, D. Grodent, and S. Wannawichian (2008), The oscillation of Saturn's southern auroral oval, *J. Geophys. Res.*, *113*, A11205, doi:10.1029/2008JA013444.
- Ogilvie, K.W., and J. Hirshberg (1974), The solar cycle variation of the solar wind helium abundance, *J. Geophys. Res.*, *79*, 31, 4595-4602.
- Phan, T.D., et al. (2005), Magnetopause processes, *Space Sci. Rev.*, *118*, 367-424, doi:10.1007/s11214-005-3836-z.
- Pontius, D.H., and T.W. Hill (2006), Enceladus: A significant plasma source for Saturn's magnetosphere, *J. Geophys. Res.*, *111*, A09214, doi:10.1029/2006JA011674.

- Porco, C.C., et al. (2006), Cassini observes the active south pole of Enceladus, *Science*, *311*, 1393-1400, doi:10.1126/science.1123013.
- Priest, E.R. (1995), The Sun and its magnetohydrodynamics, in Introduction to Space Physics, edited by M.G. Kivelson and C.T. Russell, 58-90, Cambridge University Press, Cambridge, UK.
- Provan, G., D.J. Andrews, C.S. Arridge, A.J. Coates, S.W.H. Cowley, S.E. Milan, M.K. Dougherty, and D.M. Wright (2009a), Polarization and phase of planetary-period magnetic field oscillations on high-latitude field lines in Saturn's magnetosphere, *J. Geophys. Res.*, *114*, A02225, doi:10.1029/2008JA013782.
- Provan, G., S.W.H. Cowley, and J.D. Nichols (2009b), Phase relation of oscillations near the planetary period of Saturn's auroral oval and the equatorial magnetospheric magnetic field, *J. Geophys. Res.*, *114*, A04205, doi:10.1029/2008JA013988.
- Russell, C.T., and R.J. Walker (1995), The magnetospheres of the outer planets, in Introduction to Space Physics, edited by M.G. Kivelson and C.T. Russell, 503-520, Cambridge University Press, Cambridge, UK.
- Rymer, A.M., A.J. Coates, K. Svenes, G.A. Abel, D.R. Linder, B. Narheim, M. Thomsen, and D.T. Young (2001), Cassini Plasma Spectrometer Electron Spectrometer measurements during the Earth swing-by on August 18, 1999, *J. Geophys. Res.*, *106*, A12, 30177-30198.
- Shue, J.-H., J.K. Chao, H.C. Fu, C.T. Russell, P. Song, K.K. Khuruna, and H.J. Singer (1997), A new functional form to study the solar wind control of the magnetopause size and shape, *J. Geophys. Res.*, *102*, 9497-9511.

- Slavin, J.A., E.J. Smith, P.R. Gazis, and J.D. Mihalov (1983), A Pioneer-Voyager study of the solar wind interaction with Saturn, *Geophys. Res. Lett.*, *10*, 9-12.
- Slavin, J.A., E.J. Smith, J.A. Spreiter, and S.S. Stahara (1985), Solar wind flow about the outer planets: Gas dynamic modeling of the Jupiter and Saturn bow shocks, *J. Geophys. Res.*, *90*, 6275.
- Southwood, D.J., and M.G. Kivelson (2007), Saturn magnetospheric dynamics: Elucidation of a camshaft model, *J. Geophys. Res.*, *112*, A12222, doi:10.1029/2007JA012254.
- Spreiter, J.R., and A.Y. Alksne (1970), Solar-wind flow past objects in the solar system, *Annu. Rev. Fluid Mech.*, *2*, 313-354.
- Stahara, S.S., R.R. Rachiele, J.R. Spreiter, and J.A. Slavin (1989), A three dimensional gasdynamic model for solar wind flow past nonaxisymmetric magnetospheres: Application to Jupiter and Saturn, *J. Geophys. Res.*, *94*, 13,353-13,365.
- Stanley, S. (2010), A dynamo model for axisymmetrizing Saturn's magnetic field, *Geophys. Res. Lett.*, *37*, L05201, doi:10.1029/2009GL041752.
- Stevenson, D.J. (1982), Reducing the non-axisymmetry of a planetary dynamo and an application to Saturn, *Geophys. Astrophys. Fluid Dyn.*, *21*, 113-127.
- Stevenson, D.J. (1983), Planetary magnetic fields, *Rep. Prog. Phys.*, *46*, 555-620.
- Talboys, D.L., C.S. Arridge, E.J. Bunce, A.J. Coates, S.W.H. Cowley, and M.K. Dougherty (2009), Characterization of auroral current systems in Saturn's magnetosphere: High-latitude Cassini observations, *J. Geophys. Res.*, *114*, A06220, doi:10.1029/2008JA013846.
- Tokar, R.L., et al. (2006), The interaction of the atmosphere of Enceladus with Saturn's plasma, *Science*, *311*, 1409-1412, doi:10.1126/science.1121061.

- Warwick, J.W., et al. (1981), Planetary radio astronomy observations from Voyager 1 near Saturn, *Science*, *212*, 239-243.
- Wei, H.Y., C.T. Russell, A. Wellbrock, M.K. Dougherty, and A.J. Coates (2009), Plasma environment at Titan's orbit with Titan present and absent, *Geophys. Res. Lett.*, *36*, L23202, doi:10.1029/2009GL041048.
- Wilson, R.J., R.L. Tokar, M.G. Henderson, T.W. Hill, M.F. Thomsen, D.H. Pontius Jr. (2008), Cassini plasma spectrometer thermal ion measurements in Saturn's inner magnetosphere, *J. Geophys. Res.*, *113*, A12218, doi:10.1029/2008JA013486.
- Young, D.T., et al. (2004), Cassini plasma spectrometer investigation, *Space Sci. Rev.*, *114*, 1-112, doi:10.1007/s11214-004-1406-4.
- Zarka, P. (1998), Auroral radio emissions at the outer planets: Observations and theories, *J. Geophys. Res.*, *103*, 20,159-20,194.